Prediction of Human Postural Response in Shipboard Environments using Multibody Dynamics and Sensory-based Control

by

Nicholas Bourgeois

Carleton University

A thesis submitted to

the Faculty of Graduate and Postdoctoral Affairs

in partial fulfillment of

the requirements for the degree of

Doctor of Philosophy

in

Aerospace Engineering

Department of

Mechanical and Aerospace Engineering

Carleton University

Ottawa, Ontario

Abstract

Accurate prediction of the human response to ship motion can lead to improved safety and efficiency of ship operation and design. The objective of this thesis is to derive and validate a human postural stability model having similar dynamic response to an actual human when exposed to six-degree-of-freedom ship motion. The human body is modelled as a four-link inverted pendulum, which allows for representative motion of the ankles, knees, waist, and neck. Human postural stability experiments were performed during an eight day heavy-weather sea trial in the North Atlantic Ocean. This was the first known attempt to use a variety of advanced data acquisition techniques in a shipboard environment to record human sensory stimuli. This included using two full-body motion capture systems to record body segment positions and orientations, instrumented shoe insoles to measure somatosensory data, an inertial sensor to measure head vestibular data, and a head-mounted camera to capture visual proprioceptive data. The separate data sets were combined in order to describe the motion of each subject's centre of mass and centre of force within their base of support. Human postural reactions during the sea trial were correlated with the ship motion in order to derive control gains for the inverted pendulum model which included both open-loop and closed-loop components. Simulation results were compiled from 49 test cases and it was observed that the derived controller matched human response frequently in both postural roll and pitch. Further analysis indicated that there was a consistent relationship between the accuracy of the model's motions and the direction of greater ship angular motions.

The specific contributions of this thesis include the spatial postural stability model, the detailed biometric data gathered during the sea trial, the control system developed by correlating ship motions with human response, and the compilation of comprehensive data sets of postural stability parameters of humans experiencing six-degree-of-freedom motion.

Acknowledgements

I would like to thank Rob Langlois, my supervisor and friend, for his support and guidance over the last five point five years of this doctorate degree. If you had not tempted me back to grad school with exciting research opportunities at a research facility that is even now still being built, none of this wonderful journey would have taken place.

I would like to thank Aren Hunter, Roger Arsenault, Alex Ritchie, and the rest of the scientific staff at DRDC-Atlantic for all of their generous support in planning and performing the sea trial experiments. I would also like to extend my gratitude to the crew of CFAV Quest because without their help the human postural stability experiments would not have been as successful as they were.

I would like to thank Heather Morris for her help in setting up and recruiting volunteers for the sea trial experiments. I would also like to thank Jamie Leveille for providing a template upon which to base my dynamics notations. Finally I would like to thank Jon Plumpton for his moral support over the many long hours of this project.

List of Symbols

This section defines symbols by chapter in order to accommodate symbol reuse between chapters. All lower case plain text symbols represent scalar values. Lower case bold symbols represent vectors. Upper case bold symbols represent matrices.

Symbols Introduced in Chapter 3

Symbol	Description
$\mathbf{R}^{LG}$	Local to global transformation matrix
$\mathbf{R}^{JK}$	Transformation matrix from frame J to frame K
$\mathbf{R}_{xyz}$	Rotation matrix using XYZ Euler angle convention
$\mathbf{R}_{zyx}$	Rotation matrix using ZYX Euler angle convention
$\mathbf{T}^{AHRS}$	Transformation matrix between AHRS400 and model coordinate systems
$\mathbf{T}^{BVH}$	Transformation matrix between iPi Studio BVH coordinates and model coordinate systems
$\mathbf{a}$	Translational acceleration vector
a_i	Translational acceleration in direction of axis i
θ_i	Bryant angle about axis i
$a_{i,j}$	Value of row i and column j entry in matrix $\mathbf{A}$
m_f^k	Mass fraction of body k
$\mathbf{r}_{CoM}$	Position of total system centre of mass
$\mathbf{r}_m^k$	Position of body k centre of mass
d^k	Proximal distance as a fraction of total segment length
mg	Weight of a person, mass times acceleration due to gravity
g	Acceleration due to gravity (9.807 m/s^2)

I_{ii}	Moment of inertia about axis i
d	Mass-normalized mass moment of inertia about X and Y axes
b	Mass-normalized mass moment of inertia about Z axis
F_L	Y-axis interface force between left foot and ship deck
F_R	Y-axis interface force between right foot and ship deck
N_L	Z-axis interface force between left foot and ship deck
N_R	Z-axis interface force between right foot and ship deck
M_L	X-axis interface moment between left foot and ship deck
M_R	X-axis interface moment between right foot and ship deck
x_L	Distance along Y axis between left foot and centre of mass
x_R	Distance along Y axis between right foot and centre of mass
h	Distance along Z axis between ship deck and centre of mass
A_y	Translational acceleration measured by IMU along Y axis
A_z	Translational acceleration measured by IMU along Z axis
Ω_y	Angular velocity measured by IMU about Y axis
Ω_z	Angular velocity measured by IMU about Z axis
Λ_x	Angular acceleration measured by IMU about X axis
$\mathbf{f}_L$	Reaction force vector between left foot and ship deck
$\mathbf{f}_R$	Reaction force vector between right foot and ship deck
$\mathbf{m}_L$	Reaction moment vector between left foot and ship deck
$\mathbf{m}_R$	Reaction moment vector between right foot and ship deck
$\mathbf{a}_{CoM}$	Acceleration vector of centre of mass
$\mathbf{r}_R$	Relative position between the centre of mass and the left foot
$\mathbf{r}_L$	Relative position between the centre of mass and the right foot
$\boldsymbol{\omega}$	Angular velocity of the person's centre of mass
$\dot{\boldsymbol{\omega}}$	Angular acceleration of the person's centre of mass

$\mathbf{I}$	Inertia of person
$\mathbf{I}'$	Diagonal matrix 3x3 with entries d, d, and f

Symbols Introduced in Chapter 4

Symbol	Description
$\mathbf{I}$	Identity matrix 3×3
$\mathbf{O}$	Zero matrix 3×3
${}^0\mathbf{p}^k$	Position of the centre of mass of body k in inertial coordinates
${}^0\mathbf{v}^k$	Velocity of the centre of mass of body k in inertial coordinates
${}^0\dot{\mathbf{v}}^k$	Acceleration of the centre of mass of body k in inertial coordinates
${}^0\mathbf{w}^k$	Angular velocity of body k in inertial coordinates
${}^0\dot{\mathbf{w}}^k$	Angular acceleration of body k in inertial coordinates
$\mathbf{R}_i$	Rotation matrix about axis i
$\mathbf{R}^{JK}$	Rotation matrix from frame J to frame K
${}^a\mathbf{r}^b$	Vector distance corresponding to body b, defined in frame a
${}^a r_i^b$	Component i of vector $\mathbf{r}$ corresponding to body b, defined in frame a
${}^a\mathbf{S}_q^b$	Skew matrix of vector q corresponding to body b, defined in frame a
$\dot{\mathbf{x}}$	Vector of generalized coordinate derivatives
${}^k\dot{\mathbf{x}}^k$	Generalized coordinate derivatives for body k,
	defined in k body frame coordinates
$\boldsymbol{\theta}$	Vector of Bryant angles
$\mathbf{R}^{k0}$	Transformation matrix from frame k to the inertial frame
$\dot{\mathbf{R}}^{k0}$	Derivative of transformation matrix from frame k to the inertial frame
${}^k\mathbf{w}^{k0}$	Absolute angular velocity of body k, defined in k local coordinates

${}^{k}\mathbf{Y}^{k0}$	Skew matrix of ${}^{k}\mathbf{w}^{k0}$
$\mathbf{V}^{k}$	Partial velocity matrix of body k
$\mathbf{Q}$	Transformation between ${}^{k}\mathbf{w}^{k0}$ and $\dot{\mathbf{x}}$
$\mathbf{V}_{Q}^{k}$	Partial velocity matrix of body k pre-multiplied by $\mathbf{Q}$
$\mathbf{W}^{k}$	Partial angular velocity matrix of body k
$\dot{\mathbf{W}}^{k}$	Derivative of partial angular velocity matrix of body k
$\mathbf{I}^{\mathbf{k}}$	Inertia matrix of body k defined in local body k coordinates
$\mathbf{I}^{k0}$	Inertia matrix of body k rotated into inertial coordinates
$\mathbf{I}^{0k}$	Transpose of $\mathbf{I}^{k0}$
$\mathbf{\Omega}^{k0}$	Skew-symmetric matrix of $\dot{\mathbf{x}}(\mathbf{W}^{k})(\mathbf{I}^{k0})$
$\mathbf{\Omega}^{0k}$	Transpose of $\mathbf{\Omega}^{k0}$
$\mathbf{f}^{k}$	External forces acting on body k
$\mathbf{m}^{k}$	External/control moments acting on body k
$\mathbf{A}$	Matrix of governing equations containing mass- and inertia-related terms
$\mathbf{B}$	Matrix of governing equations containing linear velocity-related terms
$\mathbf{C}$	Matrix of governing equations containing nonlinear velocity-related terms
$\mathbf{f}$	Vector of governing equations containing external forces and moments
$\mathbf{y}$	Equivalent to $\dot{\mathbf{x}}$
$\dot{\mathbf{y}}$	Equivalent to $\ddot{\mathbf{x}}$
$\mathbf{T}^{k}$	Transformation between generalized coordinate derivatives and Bryant angle derivatives for body k
I_{G}	Inertia of single-link inverted pendulum
I	Inertia of individual links of four-link inverted pendulum
M	Mass of single-link inverted pendulum
m	Mass of individual links of four-link inverted pendulum
l	Half of the length of individual links of the four-link inverted pendulum

$\boldsymbol{\theta}_{tot}$	Absolute angles of inverted pendulum with vertical axis in inertial coordinates
$\dot{\boldsymbol{\theta}}_{tot}$	Absolute angular velocity of the inverted pendulum in the inertial frame
$\mathbf{C}$	Damping matrix
$\mathbf{K}$	Stiffness matrix

Symbols Introduced in Chapter 5

Symbol	Description
$\mathbf{m}^k$	Control moments generated at the joint located at the proximal end of body k
$\mathbf{h}(h_i)$	Open-loop control scaling factors
$\mathbf{e}(e_i)$	Vector of proportional errors; input to control algorithm
$\mathbf{d}(d_i)$	Vector of derivative errors; input to control algorithm
k_1, k_2	Roll and pitch control gains derived from experimental correlations
$\mathbf{m}_{OL}$	Open-loop control moments
$\mathbf{m}_{CL}$	Closed-loop control moments
$\mathbf{x}_p, \dot{\mathbf{x}}_p$	Instantaneous model states used in stability analysis

Contents

List of Figures

List of Tables

Chapter 1

Introduction

1.1 Thesis Objective

One of the applications of modelling human postural stability is to quantify the effects of moving environments on human performance. For instance, shipboard motion environments can hinder a person's ability to perform tasks which, in turn, can result in increased operating costs of commercial vessels and in less effective warships [1]. Opportunities may exist to introduce postural stability analysis earlier in ship design cycles thereby leading to more effective ship design and increased operational efficiency. Research in this subject area is current and ongoing, as researchers have not agreed on what model complexity is needed to accurately predict incidents of loss of postural stability. Additionally, modelling human behaviour is not trivial. There are many factors which affect one's performance: age, experience, fatigue, physical health, mental health, motion habituation, and motion sickness, just to name a few [2, 3]. Regardless, the benefits of accurate models outweigh the difficulties that are encountered in the process of their development. Further, this research is relevant and timely, as Canada is embarking on its largest ship building programme in recent history [4].

The purpose of this thesis is to contribute to the study of human balance dynamics with the development of a multi-link, spatial, human postural stability model. The model's response to ship motion will be derived from experimental measurements of humans in shipboard environments acquired as a component of this project. The performance of this model will then be fine-tuned by comparing the motions of the model to the motions recorded during the shipboard experiments. This thesis will also analyze the relative motion of the centre of mass (CoM) and centre of force (CoF) for humans maintaining balance in shipboard environments. The CoM is defined as the vertical projection on the ground of the weighted average of a body's mass components. The CoF is the location in the ground plane where the vertical force acts to balance a person's weight. In quiet standing these points will be co-located; however in a constantly moving environment they will not.

1.2 Thesis Overview

This thesis has been divided into six chapters. This first chapter provides an overview of the contributions of the research work and a thorough review of past literature that can be used to justify the choices of design parameters of the experiments performed, and models derived, over the course of this research project. Following that are five chapters that describe the methodology and results of the research and development work.

The first part of this research project was to plan and execute heavy-weather sea trial experiments using a variety of data acquisition techniques which had never before been used in a constantly-moving rugged environment such as that experienced by a ship in the North Atlantic Ocean. Chapter 2 presents the instrumentation technologies that were selected for the sea trial, the ethics processes for peer approval of the experiments, the experimental procedures, any unanticipated difficulties that were encountered during the actual experiments, and an evaluation of the quality of the acquired data.

Chapter 3 presents the data processing steps that were required to transform and combine the sea trial data from the individual instrument recordings to a form from which useful experimental results could be extracted. Most of the data needed to be filtered for noise and transformed into a common coordinate system. Obstacles that were overcome include determining the absolute positions of individual human body joints, deriving the mass of each subject from human and ship dynamics, and calibration of foot pressure measurements. When all of the measurements had been combined, a time history of each subject's centre of mass (CoM) and centre of force (CoF) within their base of support (BoS) was obtained thereby providing useful metrics in the study of human postural stability. Finally, the above metrics were analyzed at identified occurrences of motion induced interruptions (MII) to compare published incidents to the experimental results.

Chapter 4 details the development and validation of a four-link inverted pendulum human postural stability model that was derived using advanced multibody dynamics techniques which automate the derivation of the equations when provided with the parameters of the model. The developed model is validated against existing published human postural stability models that have been designed for studying human response to ship motion.

Chapter 5 presents the development of a sensory-based control system for the inverted pendulum model based on the experimental data collected during the sea trial. A correlation is made between the total translational acceleration of the ship and the motion of the subject such that linear controller gains are able to be derived. A state feedback controller is then developed which incorporates open-loop and closed-loop components to match the performance of the inverted pendulum model to each of the subjects in the experimental trial.

Chapter 6 revisits all sections of the project and discusses implications of the results as well as interesting observations worth further investigation, and concludes the thesis.

1.3 Background

The following sections contain a literature review that summarizes research in each relevant subject area, and provides justifications for the selected scope of the human postural stability model introduced in the previous section.

1.3.1 Dynamic Model

Multibody dynamics methods are capable of automatically generating and solving the equations of motion of mechanical systems if the mass properties, geometrical properties, connection types, and externally applied forces of the system are known beforehand [5]. The techniques of multibody dynamics are well suited to problems in biomechanics and nonlinear system design [6]. Postural stability models with four or more links have been derived in many two-dimensional models; however, none exist in three dimensions. Some models have been developed that combine separate sagittal and frontal plane models [7, 8]. A spatial inverted pendulum has been developed for use in shipboard research [9] and a double-link spatial inverted pendulum has been developed for use in studying balance control in robots [10].

Typically the number of links in an inverted pendulum postural stability model is defined by the specific types of motion that one wishes to study. The references below are intended to justify the use of four links even though it results in additional complexity over typical postural stability models.

As far back as 1981, it was identified by Stockwell et al. that a single-link inverted pendulum does not adequately describe human postural dynamics, since investigations show that significant movement occurs at all joints, not only at the ankle [11]. An experiment was carried out where the joint angles of subjects were monitored after experiencing lateral translational displacements and there was significant movement measured at ankle, knee, hip, and neck joints. This indicated that a model with at least four degrees of freedom in two dimensions was necessary to represent human sway.

In 1982, Diener et al. performed sway experiments at varying frequencies [12]. They observed that displacements of the head were usually less than those of the hips, so they theorized that a separate compensatory mechanism was being used to stabilize the spatial position of the head. The objective of this mechanism would be to minimize retinal image motion.

In 1989, Barin compared experimental data of human motion to inverted pendulum models with one to four links. The results consistently showed significant differences between one- and two-link models, although the comparison metric was limited to differences in centre of pressure [13]. Barin discussed that there was a trade-off between using a four-link model, that is more appropriate for studying sensory mechanisms, and a two-link model which is more appropriate if simply studying postural control methods that are confined to ankle and hip control strategies.

In 1993, Kuo and Zajac created a three-link inverted pendulum model. They studied the range of accelerations that a human could produce using different muscle exertion combinations [14]. Their results indicate that certain combinations of joint accelerations would require more neural effort than others. They also noted that keeping the knees straight greatly limits the set of achievable accelerations, and thus possible postural stability strategies.

In 1999, Bos performed an analysis on the feasibility of motion induced interruption prediction. He pointed out that one of the major failings of the single-link inverted pendulum is that it does not allow for independent head motion. This is important because humans generally try to keep their heads fixed in space as much as possible in order to form a stable optical image of the world [15].

Most work in the late 1990s and early 2000s focused on development of control strategies for the inverted pendulum. However, in 2009, Xinjilefu et al. produced a two-link spatial inverted pendulum [10]. Their motivation behind developing a spatial model was that centrifugal and Coriolis forces have no equivalent in a planar model, due to their formulation as cross products, and are fundamental to stabilization strategies. While progressing to a spatial model has merit, the motivation given seems inconsistent with fundamental dynamics principles. This expansion into a spatial model is important as there are also experimental results which underscore that a three-dimensional model is necessary in order to fully understand how balance is maintained in everyday life [16].

1.3.2 Sensory Input

The human body receives sensory input from three primary sources. The vestibular system, located in the inner ear, which measures angular velocity and linear acceleration; the somatosensory system, which measures the distribution of pressure on one's skin; and the visual feedback system. In order to construct a sensory model which can reflect the complex behaviour of humans, it is necessary to include all three of these systems.

Modelling these sensory systems to behave similarly to a human is a nontrivial task. Together the three sources of sensory information provide redundant data that the central nervous system fuses together to determine current body orientations. In addition to this, there are examples of cases where postural stability can no longer be maintained if one of these sensory inputs are removed, and also cases where, due to permanent disability, the central nervous system has adapted to maintaining balance without one of the inputs. Looking at the general case only, an observation can be made that either there is error in the full-state feedback of joint angles, that postural stability is better controlled or optimized with these additional inputs, or the additional inputs are simply a redundant sensory mechanism.

The most common method for incorporating additional sensory mechanisms into postural stability models is to use a strategy that fuses the data together with weights or otherwise, in order to obtain an optimal estimation of current body orientation. Joint torque outputs are then calculated in order to move to or maintain a specific orientation.

In 1983, Hemami and Stokes studied the possible feedback loops used by the central nervous system [17]. They discussed that somatosensory signals from the bottom of the feet are likely necessary for postural stability.

Corna et al. performed postural stability experiments in 1999 [18]. While their experiments were focused on how humans manage their momentum in oscillating conditions, they observed that vision played a major role in their results. When vision was allowed, subjects behaved similarly to flexible pendulums with their heads stabilized in space. When vision was not allowed, the heads of the subjects oscillated more than the motion platform used to perturb the subjects, especially at low frequencies.

An early model of multisensory integration was developed by Borah et al. in 1988 [19]. It contained dynamic models of the sensory mechanisms discussed above, and modelled the central nervous system as a steady state Kalman filter that optimally blended information to form an estimate of spatial orientation. Time delays in receiving information were also considered. These principles have continued to be studied since that time.

In 1995, Kuo set out to determine whether optimal control and state estimation could explain the selection of control strategies used by humans in response to small disturbances to stable upright balance [20]. He developed an optimal control system that reasonably matched experimental data by combining measurements of centre of mass with body deviations calculated from a state estimation model. In his conclusions, he observed that the nature of a model such as this limits the possible reactions of the central nervous system to specific postural responses. This provides useful insight into studying human motor control systems.

In 1998, van der Kooij et al. combined a similar optimal control system with a three-link inverted pendulum dynamic model [21]. They specifically added a predictive element to the controller to compensate for time delays. Their model results for total body sway closely resembled experimental results. This model was further developed in 2001 to include an adaptive estimator model which dynamically reweighed sensory error signals as a function of environmental conditions [22]. Their improved model showed results that were in agreement with specific phenomena observed in experiments, such as: that vestibular function was essential to prevent falling and that loss of somatosensory feedback also had a significant effect on postural response to sudden support-base displacements.

In 2003, Bos et al. discussed how the central nervous system, when provided with an assortment of sensory data and an efferent copy of body motor commands, likely gives a prediction of body motion that is more accurate than that estimated by the sensory system alone [23, 24]. They commented that a subject's experience should be incorporated into an internal model. There is also substantial evidence that vision plays a major role in postural stability due to the fact that a sudden change in one's entire visual scene can result in significant perturbations [25].

Based on these examples presented above, it is clear that including all of the human sensory mechanisms and deciding how they are to be modelled can have a significant impact on the fidelity of a postural stability model.

1.3.3 Control System

The objective of the design of the control system for the inverted pendulum model is to mimic the system components and strategies that are possibly used by the central nervous system, and to have the resulting dynamic model behave similarly to a human performing balance control. This is a challenge because typically postural stability model control systems are intended to simply maintain stability, and are tuned to optimize a specific response characteristic. Human balance on the other hand, may or may not be optimized for the same types of responses. Another challenge is that while a control system may be tuned with specific experimental data, it may not behave consistently when exposed to a new motion situation.

Development of a model of human balance control can be divided into two parts. The first is to determine what exactly human senses measure that contributes to postural stability. This was discussed in the previous section. The second part is to determine how that information travels to locations where it can be processed, how it is processed by the central nervous system or other intermediate processing facilities, and how muscles respond to various inputs which results in body motions. The research reviewed in this section is intended to emphasize specific components that it is believed a human balance control system should contain.

Most research work that involves modelling human balance as an inverted pendulum can be traced back to a doctoral thesis written by Nashner in 1970 [26]. He identified two important points in designing a model to mimic human balance control. One is that there should be a difference between quiet standing, which does not include perturbing forces, and situations that do require control in the presence of small perturbing forces. The second is that various sensory organs provide specific feedback states, and that they may be processed by the body in different ways and at different rates. Both of these strategies suggest the use of a control method that has nonlinear aspects.

Stiffness Control and Ankle/Hip Strategies

Winter et al. studied and modelled how the central nervous system controls and maintains an upright standing posture without external perturbations, a condition commonly known as quiet standing [27]. It was reasoned that for small perturbations only passive stiffness, such as that provided by a spring, was present and that visual and vestibular feedback played very little part in maintaining balance. This control strategy was incorporated as part of a spatial inverted pendulum stability model developed by Langlois [9]. It implemented feedback control as linear combinations of the states, but also divided the feedback into separate stiffness, damping, and active control terms. This large passive muscle stiffness that is observed when joint displacements are small can also be considered an example of co-contraction [28].

Many research projects study and identify the differences between the “ankle strategy” and the “hip strategy”, which can be traced back to research conducted by Horak and Nashner in 1986 [29]. Their research identified two distinct control strategies where control output response is dominated by output torques at either the ankles or hips. They observed that various postural behaviours could be achieved by combining these two strategies in various magnitudes and temporal relations. Later research by Kuo et al. reinforced that actual human responses are more often a combination of both ankle and hip strategies, as independent control of either joint is difficult to achieve [14].

Feedback Time Delays and State Estimation

In 1995, Kuo presented a controller combining a parameterized linear quadratic regulator (LQR) with a linear quadratic estimator (LQE) [20]. These two components provided state feedback and estimation. Kuo indicated that while there was no evidence that the central nervous system operates like an LQR controller, there were plausible arguments that it should behave like one. Another notable statement made by Kuo was that an important consideration in a biological system is that the controller must be stable even with substantial transmission delays, which state estimation is well suited for.

In 1997, Tian and He developed a model with time delays and used internal estimation models to compensate for the delay and to prepare for a predictable perturbation [30]. Similar models were developed by Kooij et al. in 1999 and 2001 which used optimal estimation theory, including a predictive component in the form of an extended Kalman filter to compensate for time delays [21]. It was later further advanced to include an adaptive estimator model of spatial orientation which applied weights to the difference between expected and actual sensor signals as a function of environmental conditions [22]. In 2003, Roy and Iqbal attempted to model short, medium, and long muscle invariant latencies that the central nervous system uses to maintain balance [31]. In 2009 Tahboub used feedforward and feedback components in the postural control of a simple robot intended for the study of postural stability [32].

Nonlinear Control Strategies

A common strategy for controlling an inverted pendulum is to linearize the dynamic equations around a specific system state and to apply linear control methods. The equations of motion of an inverted pendulum are nonlinear so this control scheme is reduced in effectiveness beyond orientations where small angle assumptions are valid. Nonlinear control strategies can provide better performance in such situations.

One method is to essentially add multiple linear control strategies that change depending on system orientation [33, 34, 35]. This method was common prior to the computational capacity that became readily available within the last decade. Since then, more complex nonlinear control methods have been implemented successfully.

In 1999, Wang and He implemented a fuzzy controller to improve controller performance outside of the linear control region [36]. Also in 1999, Wu developed a controller that used piecewise continuous control strategies with its discontinuous portions replaced with smooth functions in order to remove potential chatter in the controller [37].

In 2004, Frazier and Chouikha presented a new nonlinear postural controller [38]. It was an optimal switching state controller that also contained a learning algorithm intended to imitate the central nervous system, thereby providing improved performance over a controller using a linear quadratic Gaussian (LQG) and an extended Kalman filter.

In 2006, Virk suggested the possibility of reweighing redundant control inputs in the central nervous system in real time as a method for adaptive control [39].

Open-Loop Control

In some postural stability models, open-loop control strategies have been employed. While there are many models that do not use it, it was recognized by Nashner in the 1970s that balance was maintained through a coordinated effort of leg muscles [40, 33]. In 1983, Hemami and Stokes observed a variety of postural movement strategies which support the existence of feedforward and feedback pathways [17]. In 1995, Kuo developed a controller which contained both open-loop/feedforward and closed-loop/feedback components [20]. The controller was designed to select which method to use based on the current system state. A feedforward control was also used by Frazier and Chouikha in order to minimize the transient error in response to a disturbance [38] in conjunction with a feedback component and other control components.

1.3.4 Motion Induced Interruptions

The ship design community quantifies loss of stability events of a person on board a ship at sea using the rate of motion induced interruption (MII). It is typically measured as the number of loss of balance events per minute that occur during an arbitrary deck operation [41]. A loss of stability is typically defined as the time when a subject in a moving environment has to stop their current task and grab on to something or focus on stability in order to maintain their balance [42].

Records of experimental MIIs are used in combination with biomechanical models of the human body to construct models that predict the frequency of MIIs for a standing person during particular ship movements or sea states. Using these results, one can generate criteria as to when it is safe or dangerous to perform particular shipboard tasks [2].

The term MII was first introduced by Baitis et al. with their research efforts that were focused on the effect of human factors on ship operations [43]. The first mathematical formulation was developed in the early 1990s and is known as the Graham model [1]. This model consists of a block sitting on a moving surface that has mass properties similar to a human.

The MII model predicts that a person will lose balance during a simple motor task when the accelerations experienced by that person exceed a specific threshold. MIIs occur under three distinct phenomena:

- sliding due to the forces induced by the ship overcoming the frictional forces between movable objects and the deck;
- tipping due to a momentary loss of postural stability; and
- the very occasional and potentially the most serious condition where lift-off occurs due to inertia forces exceeding the restraining force of gravity.

The third condition is not modelled in MII literature due to the extreme conditions under which it would occur. However, anecdotal evidence of its occurrence in practice is not uncommon.

Experiments have shown that quantifying these conditions alone tends to overestimate the occurrence of sliding and tipping events, so subsequent researchers have added tuning coefficients to match these equations better to experimental data.

For example, Crossland et al. adjusted the tipping model with coefficients that take into account the added complications from changing posture, oscillations in body centre of mass, and active postural control [42]. These coefficients were derived by counting MIIs under prescribed motion conditions and noting accelerations at the time the MIIs occurred. One disadvantage of this method is that it can make it difficult to generalize the model for multiple conditions or activities.

A second method for improving Graham's model is to improve the fidelity of the box that represents a human standing on a ship deck. This is done by adding articulation to the model. For example, adding a revolute joint at the base could be used to model ankle movement. This method also requires a control system for the model to maintain a specific orientation. Such a model was developed by Langlois et al. in the form of a 2D inverted pendulum shown in Figure 1.1 [44]. The tuned model reproduced the MII rate and agreed in time for 41 percent of MII events. This result was not ideal, but it was noted that this model was a first step toward the development of more sophisticated articulated postural stability models.

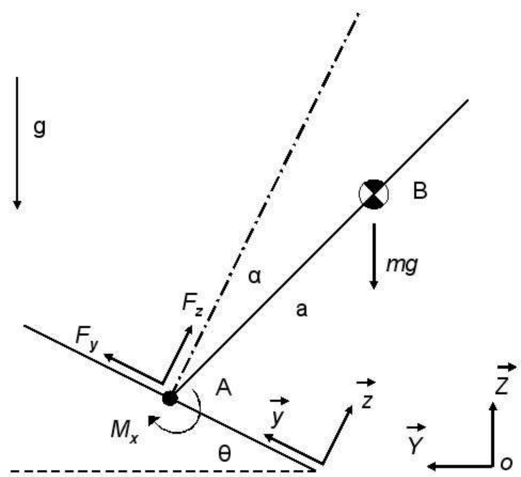

Figure 1.1: Inverted pendulum model for detection of MIIs [44].

A much more complex model was later developed by Langlois, which included a detailed derivation of a spatial inverted pendulum [9]. This created a human model that was allowed to pivot at the ankles and maintained its position with a control system that represented the maximum effort that a human could put into maintaining balance during a specific task. If the required restoring torque was greater than a predetermined amount, then it indicated that an MII had occurred. For this model, sliding and tipping were defined, as well as yawing. The model was demonstrated using experimental data recorded during the

Quest Q-303 heavy weather sea trial [45] that was held in winter 2007 and the model was able to be verified for a single articulated segment with two revolute degrees of freedom.

1.3.5 Sea Trials

In order to validate human postural models and in this case to design a control system which behaves similarly to that of a human in shipboard environments, it was necessary to perform balance experiments with human participants in moving environments which record human body orientations and the inputs that human senses might use to determine those body positions and orientations.

Similar experiments to the ones presented in this thesis were carried out aboard Quest trial Q-303 in 2007. Those experiments were different in that their execution was the primary objective of the sea trial (rather than a secondary objective as in the case for this thesis) and they incorporated a variety of tasks and measurement strategies contributed to by a multi-national group of researchers from Australia, Britain, Canada, and the Netherlands. The Canadian contributions were provided by Memorial University of Newfoundland, the University of New Brunswick, and DRDC Atlantic [45]. That sea trial is the first known attempt at quantifying MIIs in an at-sea shipboard environment for which the transient ship motion and times of occurrence of MIIs were recorded. During the Q-303 sea trial, 12 subjects were asked to perform a series of manual materials handling (MMH) tasks. The subjects were videotaped such that MIIs, as defined by an adjustment in their stance, could be identified through post-experiment analysis of the video records [46]. Overall, the current experiment is similar to the Q-303 sea trial, but with more precise and extensive use of data measurement systems.

1.4 Contributions of the Thesis

While conducting the work described in this thesis, the following significant research and development contributions have been made.

1. Development of the first spatial human postural stability model that incorporates representative motion for ankles, knees, hips, and neck; human-like mass properties; and a control system that is designed to mimic human balance control, maintaining stability when exposed to six-degree-of-freedom (DOF) ship input motions.

2. Development and execution of the first-known shipboard human postural stability experiments which incorporate full-body motion capture, extensive foot force/torque measurements, and body-fixed and ship-fixed inertial measurements. This is also the first time the occurrences of motion induced interruptions have been identified and analyzed to the extent enabled by a motion capture system in a shipboard environment.

3. The first known attempt at deriving a control system based on the ship kinematics and orientation of the subject within their local frame rather than within the inertial frame, which when simulated and compared to the experimental measurements, successfully mimics human centre of mass motion in the direction of greatest ship motion.

4. Compilation and detailed analysis of comprehensive data sets studying the motion of a person's centre of mass and centre of force within their base of support in a real six-DOF shipboard motion environment; unlike most published experiments which have been performed on motion platforms.

Chapter 2

Quest Sea Trial Q-348

2.1 Introduction

One of the shortcomings of existing research on human postural stability is the lack of experimental shipboard data that focuses on human performance in various sea conditions while performing a variety of shipboard activities.

In order to address the need for relevant experimental data, a number of postural stability experiments were carried out on board Canadian Forces Auxiliary Vessel (CFAV) Quest during the Q-348 sea trial from November 20th through November 28th, 2012. Thirteen participants took part in postural stability and cognitive efficiency experiments carried out by researchers from Carleton University and Defence Research and Development Canada Atlantic (DRDC-Atlantic). Participants took part in 90-minute experimental sessions in which they were asked to maintain balance while performing a cognitive task, and while standing at various orientations with respect to the ship centreline. The data measurement procedures in this experiment were unique in that they attempted to measure all of the sensory inputs that a person might use to maintain balance. This experiment was also unique in its use of a cognitive task to investigate the overall impact of motion induced interruptions on task performance from a memory for goals theory point of view, which was the contribution of DRDC-Atlantic to the experiment [47, 48].

2.2 Quest Q-348 Sea Trial

CFAV Quest is a civilian-crewed ship operated by DRDC-Atlantic for research purposes. The ship is a dredger type, built in 1969, and has an overall length of 76 metres and a beam of 10 metres. The ship has been modified for acoustic research by shock-mounting all of its engine components which minimizes vibration outside of the engine compartments. This makes it ideal for sensor measurements that involve motion. A photograph of CFAV Quest prior to the Q-348 sea trial is shown in Figure 2.1.

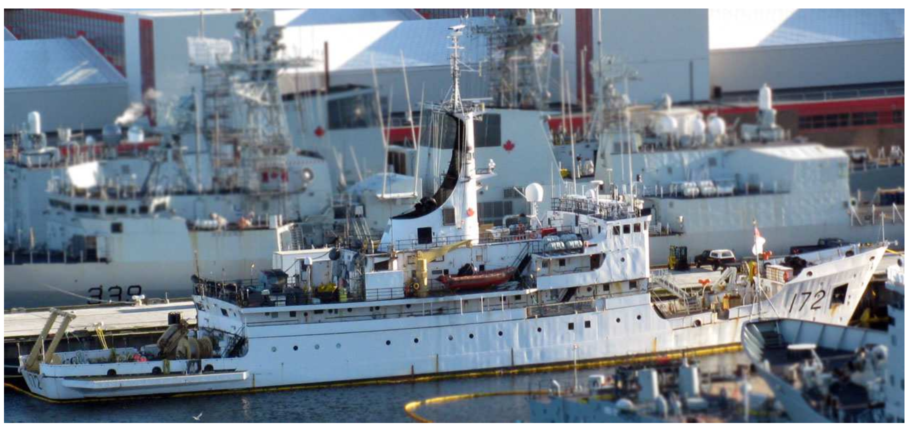

Figure 2.1: Photo of CFAV Quest.

There are two main laboratory areas on board Quest. During the Q-348 sea trial the larger aft lab area was used for a concurrent unrelated research experiment and the smaller mid-ships laboratory was allocated to human motion experiments. Figure 2.2 shows the location where the experiments took place, relative to the rest of the ship, indicated by the solid black square.

The ship left Halifax harbour at approximately 1020 on Tuesday, November 20, 2012;

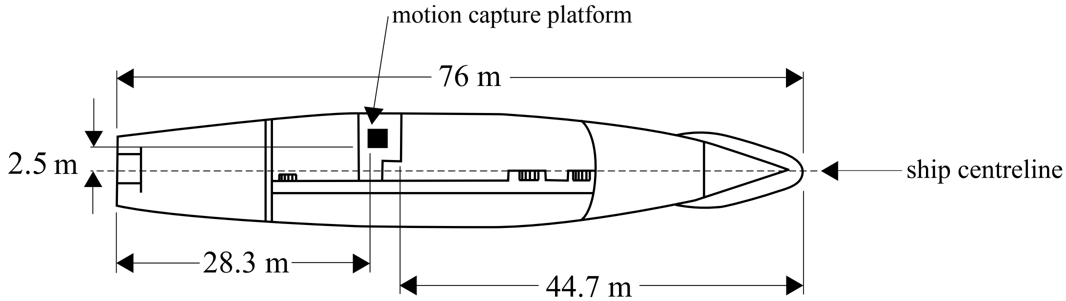

Figure 2.2: Position of motion capture platform within mid-ships laboratory on board CFAV Quest.

and returned to the dockyard at approximately 0900 on Wednesday, November 28, 2012. The ship spent the majority of its time in the Emerald Basin, an area of water approximately 70 nautical miles south of Halifax, Nova Scotia, Canada.

The primary experiment required the deployment of four wave buoys followed by navigation of the ship along specific patterns for the remainder of the experiment. The GPS coordinates recorded over one day of the sea trial are shown in Figure 2.3. The variety of ship headings was intended to ensure that the ship encountered all of the different ship heading/wave direction combinations.

The wave buoys were deployed as soon as Quest arrived at the Emerald Basin late on November 20, 2012 and were retrieved once the weather had settled on November 27, 2012. A recording of significant wave height made by one of the buoys is shown in Figure 2.4. Significant wave height is defined as the mean of the largest third of the wave heights. The scale used in the figure has been defined by the World Meteorological Organization Sea State Code [49].

As can be seen in the figure, there were two optimal periods for gathering data where the heights of the ocean waves were of greatest magnitude. Due to the logistics of setup and execution of the experiments, the work carried out during the first period focused mainly on calibration of the recording equipment and finalization of the experimental procedures.

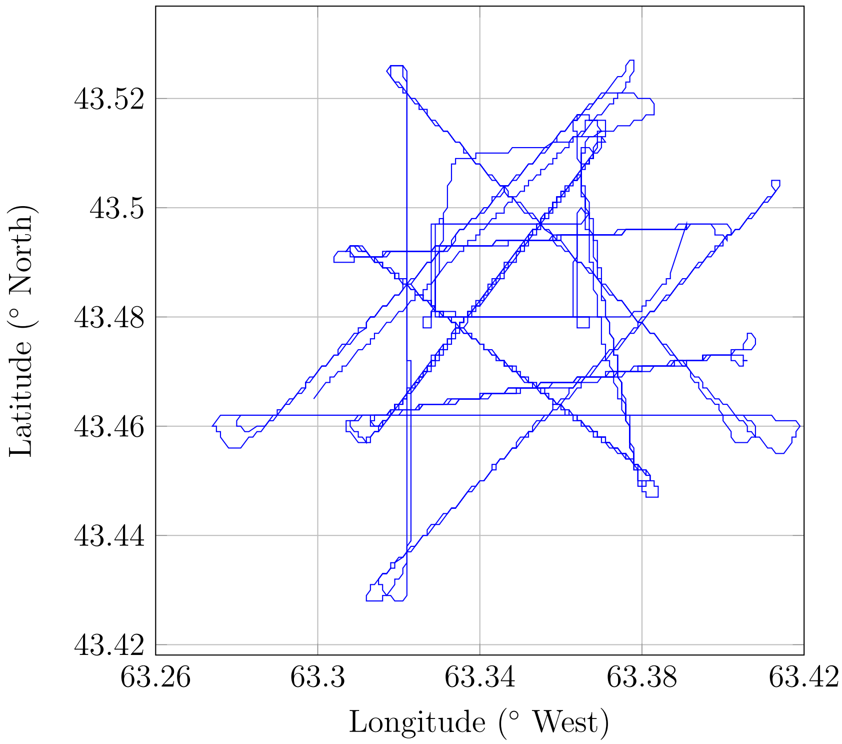

Figure 2.3: Ship GPS measurements for Nov 24, 2012.

The second period is when the majority of the experimental trials were carried out.

2.3 Research Ethics

Before this research could be carried out it was necessary to obtain approval from both the Carleton University and DRDC Research Ethics Boards. Both ethics application submissions required that detailed protocols be written in advance which focused on:

- background and relevance of the research to both Carleton University and the Canadian Forces;
- selection of personnel and procedures of informed consent to the experiments and/or withdrawal as applicable;
- data acquisition procedures and techniques;

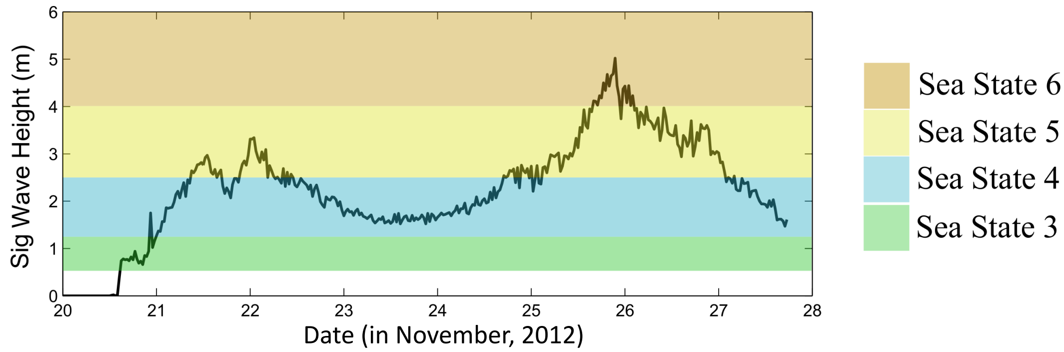

Figure 2.4: Significant wave height over the eight day Q-348 sea trial.

- risks to the participants and methods for managing those risks; and
- details on confidentiality and anonymity of participants both during and after the sea trial.

Before the start of the sea trial, the research project was granted ethical clearance by the Carleton University Research Ethics Board (13-0632) and was also reviewed and approved by the DRDC Human Research Ethics Committee (2012-045). The ethics clearance documents are included in Appendix A.

2.4 Experimental Procedures

The human postural stability experiments were not the primary research goal of the sea trial. As a result of this, and due to space limitations, it was not possible to bring dedicated subjects on the sea trial for the experiments. Participants were instead recruited from the ship crew and scientific staff after the ship had departed. Of the 35 crew and scientists on board, 13 volunteers were able to spare time from their duties to take part in the experiments. Of the 13 volunteers, 10 were male and 3 were female. There were no restrictions on who was permitted to participate. The motions experienced by the participants were no different from what they already would have experienced by being on the ship, so there was no increased physical risk to participants by taking part in the study. Each participant was provided with information about the experiment in advance and was required to sign an informed consent form before the experiment. They were also informed that they could withdraw from the experiment at any time.

During the planning stages of the sea trial experiments there was concern that the number of available participants would be limited. In actuality, the limiting factors on the number of experiments that were able to be carried out were the weather conditions providing large enough ship motions that the balance task was not trivialized and the number of experimental trials that was practical to perform in a day.

Each participant was allocated 90 minutes in order to allow for a sufficient amount of time for data collection without interfering with their normal schedules. Of that 90 minutes, 20-30 minutes were spent setting up and calibrating the instrumentation, 40 minutes were spent collecting the data, and the remaining time was spent processing the data between trials. Participants took part in 6, 6-minute trials which were divided evenly between three possible standing orientations of the participant with respect to the ship centreline, of 0°, 45°, and 90°. When it was possible, efforts were made to ensure that the ship heading and speed remained constant through a set of the three orientations. Unfortunately, this was not always feasible due to the time constraints of the participants and the limited duration of time spent travelling on each heading.

While maintaining balance, participants were asked to perform a data logging task using a pen and paper attached to a clipboard and then again with an electronic tablet. Each experimental trial was divided into 3 minutes using the clipboard and 3 minutes using the tablet. In both versions, participants were given a list of 3-digit numbers and were required to transcribe only the odd numbers into a new list. It was not possible to finish the task within the allotted time so participants were transcribing for the full 3 minutes.

Since one of the goals of the experiment was to measure each of the possible human sensory inputs used to maintain balance, a variety of data acquisition technologies were used during the experiment. Two different motion capture systems were used to record body positions and joint angles:

- NaturalPoint Opti-track full-body motion capture system and Arena software, which used retro-reflective markers and 8 cameras positioned around the lab to record body positions; and
- Microsoft Kinect sensors and iPi Recorder/Studio software packages, which used the Kinect's depth camera to determine the positions and orientations of joints in 3D-space.

In order to obtain somatosensory measurements, otherwise known as skin pressure data, that would be sensed at the bottoms of a person's feet, two systems were used to measure foot-ground interaction forces:

- Tekscan F-Scan system which consisted of two instrumented insoles that were wired to a computer; and
- ATI Industrial six-axis load cell located beneath a plate that subjects stood on.

Two instruments were attached to the helmet that participants wore during the experiment. The first was an Xsens inertial sensor that measured orientation angles, angular velocities, and linear accelerations similar to the human vestibular system. The second was a GoPro camera that recorded the visual field that was available to participants, based on head orientation, during the experiments.

There were two additional sensors used during the experiment. A Crossbow AHRS400 inertial sensor was installed on the experimental platform in close proximity to where the participants were required to stand during the experiments. This sensor recorded the ship motions that the participants experienced. Also, an additional video camera was used to record the experiments for future verification of collected data and to gain additional insight into the motions of particular participants if required during subsequent data analyses. A labelled photograph indicating all of the data acquisition sensors, except for the extra video camera, is shown in Figure 2.5. Additional ship data were made available from the primary sea trial experiment carried out by DRDC-Atlantic. These included additional inertial sensor data, wave height data, and ship position data.

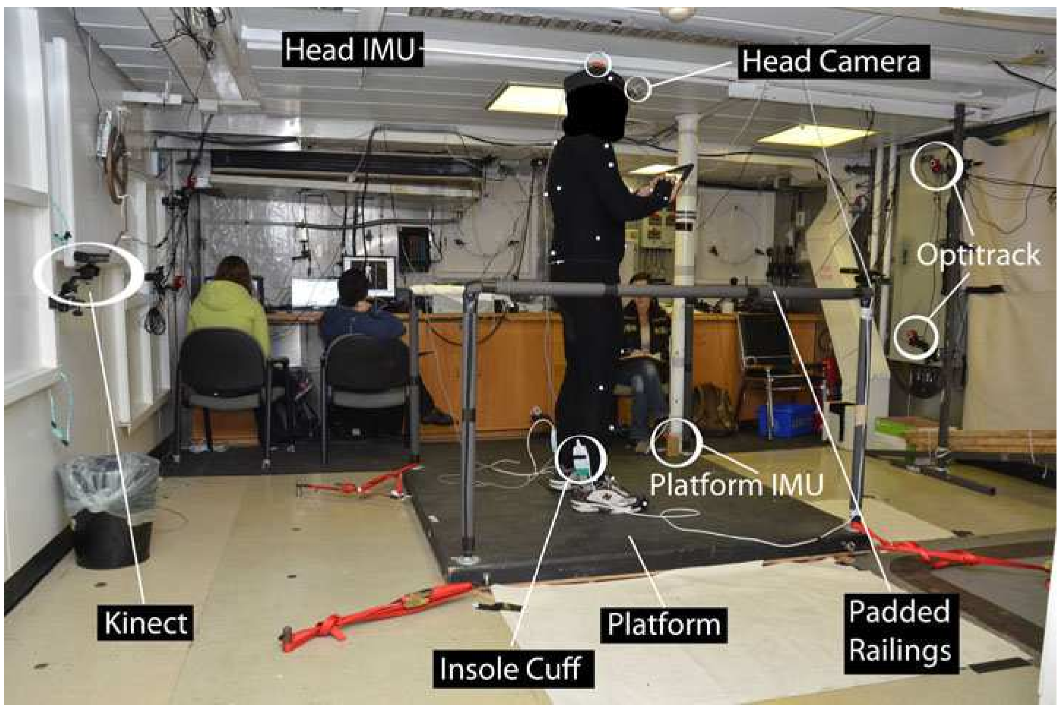

Figure 2.5: Fully-instrumented participant performing clipboard transcription task with all data acquisition equipment labeled.

2.5 Opti-track

The NaturalPoint Opti-track system was the primary motion tracking system used. NaturalPoint is a recognized industry leader in motion capture technology, marketing an assortment of motion capture systems whose capabilities range over a variety of capture volumes and measurement accuracies. Although one must be meticulous during its camera calibration and skeleton calibration procedures, the resulting motion capture data are accurate, sampled at a high frequency (100 Hz), and quickly compiled from the individual camera recordings. The system used in this case consisted of 8 high-speed cameras arranged around the lab, and 34 retro-reflective markers affixed using velcro to a skin-tight black suit worn by the motion capture target.

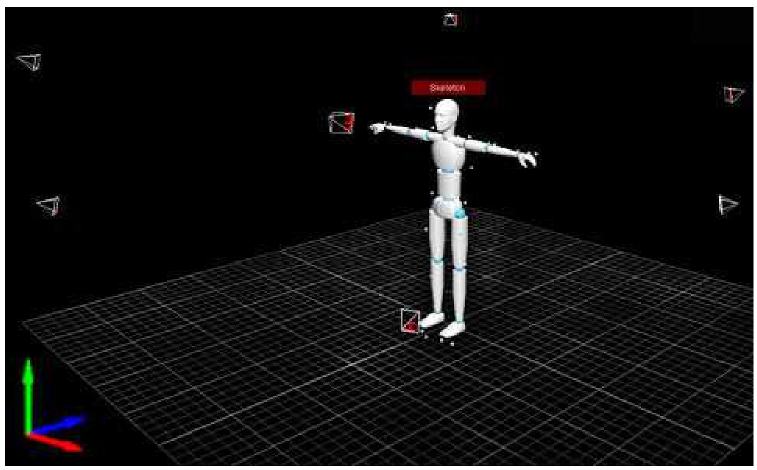

Figure 2.6: Arena T-pose with camera arrangement around participant.

Before motion capture data can be recorded with the Opti-track system, it is necessary to calibrate the cameras so that the associated Arena software can determine the 3D coordinates and pointing direction of each camera. This is done by tracking the position of a single marker as it moves through the field of view of all of the cameras. After that is completed, a square ruler with 3 markers on it is placed on the floor which indicates to the software the location of the ground plane, and defines how to orient the 3D coordinate system. Next, the participant puts on the black skin-tight outfit over their clothing to which the small reflective markers of negligible mass are attached. The markers are positioned in such a way that specific body parts can be easily identified. The skeleton calibration process next requires that the participants assume a T-pose and that all of the markers can be identified by the cameras. An image of the required T-pose is shown in Figure 2.6. Once the markers are mapped to body parts in the software, the software is able to track their positions in 3D space and motion capture can begin. Each recording session starts with a T-pose so that the Arena software can identify which markers correspond to which body parts. An image of the skeletal model in Arena with marker positions indicated is shown in Figure 2.7.

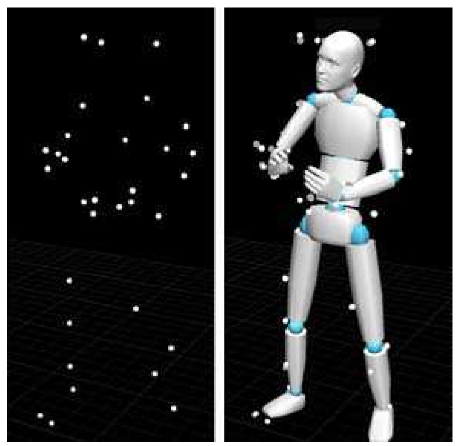

Figure 2.7: Motion tracking in NaturalPoint Arena software with and without skeleton.

Overall the system was able to obtain the motion capture data that were required: positions and orientations of feet, legs, waist, chest, and head. Unfortunately it was frequently deficient in associating the correct markers with their corresponding body part due to marker occlusion. Some of these difficulties are discussed in more detail in subsequent sections.

2.6 Kinect and iPi Studio

The Kinect sensor is a motion tracking device produced by Microsoft. The two versions available are shown in Figure 2.8: the device used with their XBox 360 gaming console (right) and a Windows-only version (left) that includes a license for development of commercial applications using Microsoft's software development libraries. Technologically, there is very little difference between the two, and one of each was used for motion capture during the sea trial. Microsoft's software tools are free for personal, academic, and open source use; however, they do not have the capability to combine motion tracking data from two or more sensors.

Figure 2.8: Kinect motion tracking hardware.

Each Kinect sensor records a video stream and a depth image stream. A sample of two depth stream images is shown in Figure 2.9. The different colours represent varying distances from the camera. Yellow indicates areas that are hidden by shadows or are too distant for the sensor to measure. The sensor determines depth by emitting and detecting an infrared light pattern, and compares the differences in the detected pattern to the image in its memory.

Various software strategies are available for using these data to determine joint positions and orientations. The commercially-available iPi Studio software that was selected for this experiment was the only software available in 2012 that could combine the data recorded from two sensors into one 3D skeletal model. The software can be used and works very

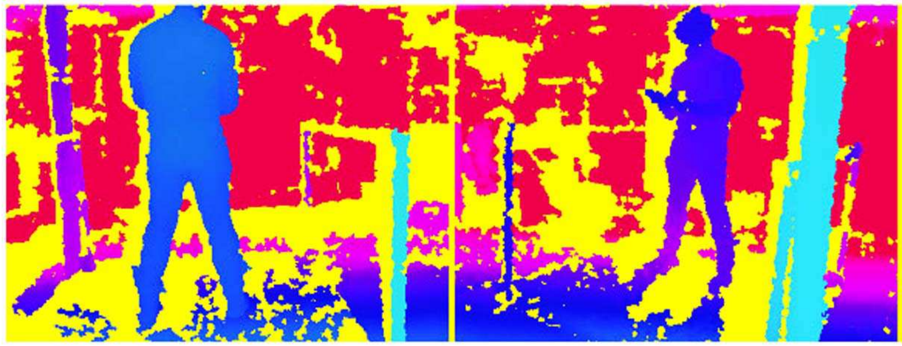

Figure 2.9: Kinect depth data recorded simultaneously from two separate cameras.

well with just one Kinect sensor, but in order to deal with issues of joint occlusion it is necessary to use two cameras, one located on each side of the subject being recorded. The resulting configuration can record motion capture data that are reasonably close to what the Opti-track can obtain, but without the need for markers or a lengthy calibration process. The software is made up of two components: iPi Recorder and iPi Studio. A screenshot from the iPi Recorder software is shown in Figure 2.9. It is capable of recording and playback of Kinect depth streams. The RGB (red-green-blue) video stream can also be recorded, but files become an order of magnitude larger in size. The iPi Studio software is then used to map the depth streams to the motion of a 3D model of a person. A screenshot with depth data from two cameras superimposed is shown in Figure 2.10.

Before each recording session, it is necessary to calibrate the two Kinect cameras so that their relative positions and orientations in 3D coordinates can be determined. This is done by recording the motion of a flat 2D surface (such as a piece of cardboard or solid plastic) by both cameras simultaneously. The iPi software calculates where the corners and the centre of the plane are located in each camera view and assumes that both cameras are looking at the same object. Depth and 3D images from this process are shown in Figure 2.11.

At the start of each Kinect recording session it is necessary for the subject to perform

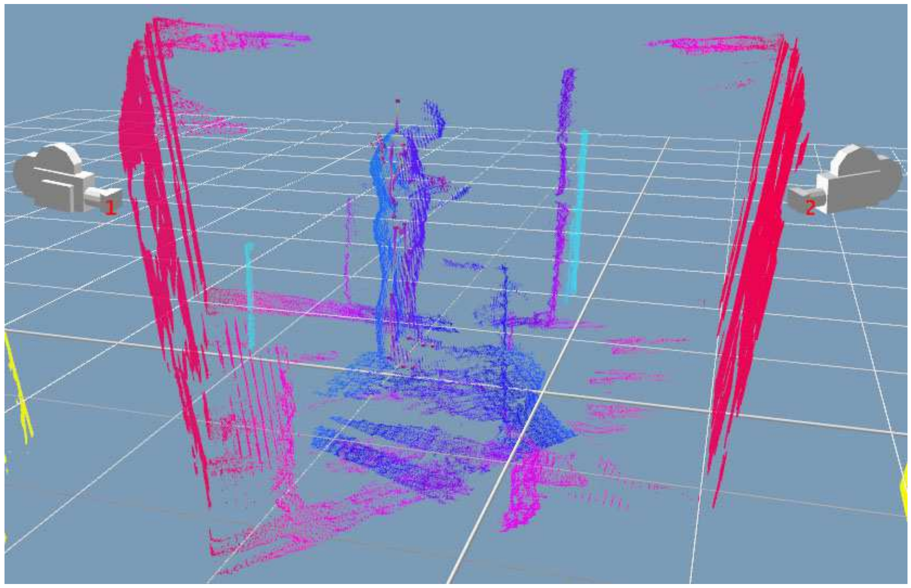

Figure 2.10: Kinect depth data from two sensors arranged in 3D space in iPi Studio.

a T-pose for a moment. At that moment in time in iPi Studio a 3D model of a person must be manually placed such that it overlaps the outline of the person in the depth recording. The software then determines the best match of the person's skeleton to the depth data. The software can then track forward or back in time to determine the best fit of a human skeleton to the depth data at each time step, based on the previous data frame. If the software cannot determine the correct body positions on its own, each joint can be manually positioned by the user.

2.7 Camera Positioning

The successful acquisition of accurate motion capture data was affected by two major factors of the recording environment. One is that both the cameras and the object being recorded were in a constant state of motion due to the motion of the ship. Both systems were designed to be used in cases where the cameras are stationary and only the recorded subject is moving. In order to prevent camera movement relative to the ship during the

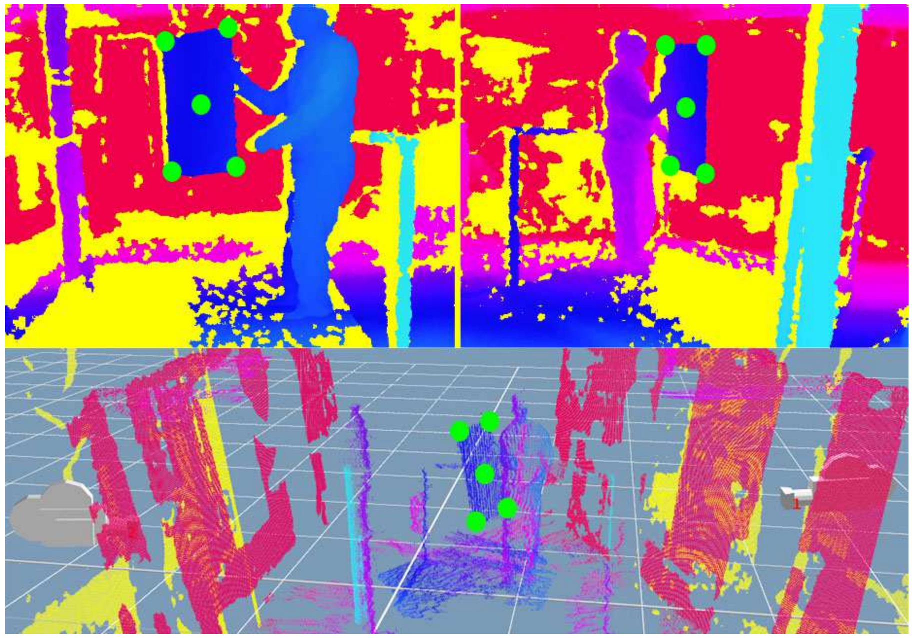

Figure 2.11: Dual Kinect camera calibration in iPi Studio.

experiments, high-quality camera arms and mounts were used to hold the cameras, and the camera arms were tightened regularly to correct any loosening that resulted from ship motion and constant low levels of vibration. There is no evidence that suggests that camera misalignment developed during the experiment. The second factor is that the recording area was smaller than the recommended recording area for both systems. NaturalPoint recommends that the Opti-track system be used in a square area having, at minimum, 4.6 metre edges, or optimally, 6.1 metre edges. For the Kinect system, it was found that the optimal configuration was to have each camera approximately 2.4 – 2.7 metres away from the subject, oriented so that the cameras are facing each other. Neither of these arrangements was possible in the Quest lab area which was approximately 4.5 metres by 4.0 metres, so both camera systems were used in a smaller-than-ideal space configuration.

Limited vertical space in the room was also an issue, especially for the Opti-track cameras which are required to track retro-reflective markers on top of the recording subject's head. In a lab environment this is handled by locating at least half of the cameras at a height that is well above the height of the subject. This was not possible on board the ship due to a maximum ceiling height of approximately 2.10 metres and participant heights that ranged from 1.54 to 1.93 metres.

The camera positions were also limited by where the cameras could be securely mounted due to physical constraints in the laboratory. The distances between the cameras are shown in Figure 2.12. The cameras at the bottom of the diagram were mounted to a bulkhead so they were able to be placed optimally on that side of the room. There were no similar mounting options on the opposite side of the room so the cameras were instead attached to steel T-frames which were constructed in advance, fastened to tapered-thread (pipe thread) bolt holes in the floor, and fastened to angle brackets on the ceiling with C-clamps. Camera positioning was also affected by a post on one side of the room. In the Kinect depth images in Figures 2.9 and 2.11 for example, the post can be clearly seen on the right (it appears in cyan). Additionally, in Figure 2.9, it can be seen in the left image that if a participant was sufficiently tall they did not fit in the frame since the camera was specifically positioned to prioritize measurement of leg positions.

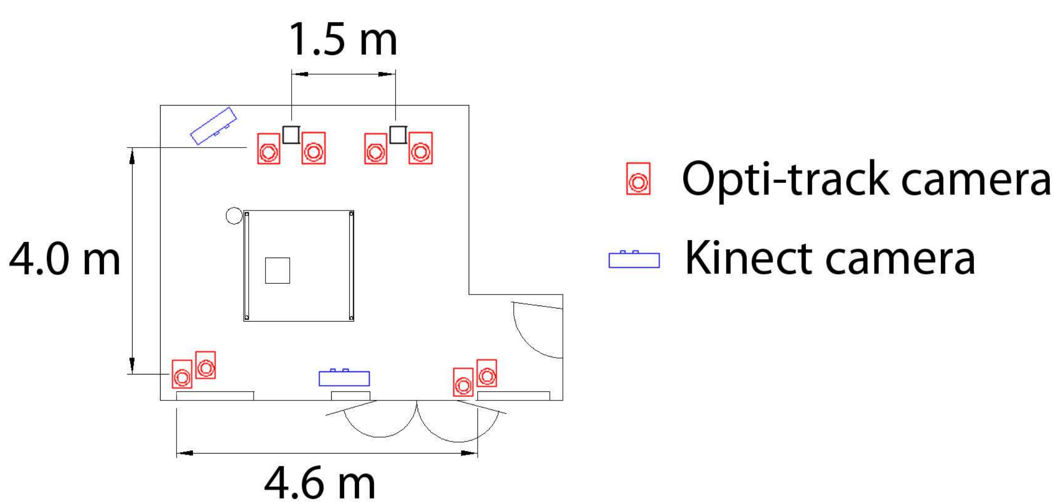

Figure 2.12: Quest lab floor plan with platform and cameras.

2.8 Marker and Body Occlusion

In order for the Opti-track system to operate correctly it is necessary to ensure that there are no other objects in the recording area that reflect light with at least equivalent intensity to the suit markers. For this reason, it was necessary to cover many of the objects and surfaces in the lab area with non-reflective tape or fabric.

The Opti-track system can track a large number of retro-reflective markers simultaneously in 3D space, which is made more complicated when those markers are attached to a human body because at any point in time a number of markers may not be visible to a sufficient number of cameras in order to be tracked properly, and it is important for markers to not be confused with each other. Opti-track compensates for each of these problems by associating marker positional patterns with specific body parts. If the position of one of the markers on a body part cannot be determined, then as long as the others remain visible the software can continue to properly record the motion. This is a very challenging task when camera positioning is limited, and when markers are frequently blocked by structures such as railings, by data logging equipment, or by other body parts. This was frequently an issue with the Opti-track recordings. One of the primary issues with the recordings was with properly tracking a subject's waist. The waist is tracked with four markers, evenly spaced around the body. The centre front marker was frequently blocked due to the clipboard or tablet associated with the cognitive task the participants were required to perform. This on its own was not an issue, but if for some reason a second waist marker was lost, the Arena software would frequently remap the waist to a different set of markers causing the entire human body model to bend into unrealistic orientations. Difficulties were also encountered with the head tracking. Due to the limited vertical space in the room, it was very rare for the head to be properly tracked at all. Most of these issues with the marker tracking can be corrected in the Arena software in post-processing, but it is a very time consuming process.

Body occlusion was also an issue with the Kinect sensor, although not to the same extent. In the recordings there are occasional cases where a leg cannot be tracked properly, or the camera may incorrectly map a body part due to an object the subject is holding, or the subject may be interacting with another person. Overall these issues did not significantly affect the data recordings, but it did take time to correct for them in iPi Studio.

2.9 Kinect Tracking Evaluation

The Applied Dynamics Laboratory has been using the Opti-track system for several years, but this is the first time a Kinect-based system has been used. Similar to the Opti-track, it is primarily aimed at the computer animation industry when used with iPi Studio. There are some significant advantages and disadvantages of using this system compared to the Opti-track system which are discussed below.

Processing time for the Kinect data is significantly longer. The Arena software can generate 3D motion data within 30 seconds for a 6-minute recording. The iPi Studio software requires approximately 90 minutes to generate 3D skeletal data from a 6-minute recording. Additional time is required to apply smoothing filters to the data. Data export from iPi Studio only supports formats that include the skeletal structure as part of the file format such as with BVH (Biovision Hierarchy), while Arena also supports the open C3D (Coordinate 3D) format that only stores the locations of points. It is also worth noting that the Opti-track system does not require a skeleton for motion capture. It is capable of tracking any combination of at least two markers that do not have relative motion between them by defining them as a 'rigid body', although three markers would be required to fully-define the orientation of said body.

The Kinect sensors are significantly less accurate than the Arena cameras. The initial

Kinect motion captures contain a considerable amount of noise because the depth error increases with distance, up to 2-3 cm at a distance of 3 m. This, however, can be offset by multiple filtering options available in the software. Also, due to the difference in camera hardware, the Kinect system is limited to 30 frames per second while the Opti-track system is capable of recording at up to 100 frames per second.

The Kinect motion capture process requires more computing power to process the data, and at minimum two orders of magnitude more digital storage for its files. The depth data processing is only performed on a computer's video card, while the motion smoothing processing is performed using a computer's processor. The Arena software only uses a computer's processor for its computations. While both systems require a significant amount of universal serial bus (USB) bandwidth in order to properly communicate with all of their cameras, the Kinect system requires each sensor to be attached to a separate USB controller. This was dealt with in the experiments by using recently released laptops with separate USB2 and USB3 ports.

The Kinect sensors need to be oriented vertically and must be able to locate the ground in order to operate properly. In the specific case of iPi Recorder, the background of the recording area cannot change over the course of a recording, because if it did, the processing software would have difficulty differentiating the recording subject from their surroundings. That said, the sensors did prove to be remarkably resilient when dealing with additional humans entering and exiting the recording area. These issues with changing environments do not arise with the Opti-track system, as long as the markers are not obscured.

With all of these disadvantages it might seem like the Opti-track system is superior to the Kinect system for motion capture experiments. In many cases this is so, although if some of the advantages of the Opti-track, such as accuracy, are not required, the Kinect system's advantages can make it a more practical system to use. These advantages include:

1. Camera and skeletal calibration processes are significantly simpler, and subjects

being recorded do not need to wear any special clothing. The initial hardware configuration setup is also simpler.

2. The Kinect system deals better with joint occlusion, which leads to less post-processing effort being required. The system is also remarkably resilient to having additional people enter the camera's field of view during a recording.

3. The Kinect system costs an order of magnitude less than the Opti-track system. Additionally, if only a single Kinect sensor is used, and the Microsoft software tools are used, motion capture recordings can be created for the cost of a single sensor, which retails for approximately $100.

4. Also available from the company that created iPi Studio at additional expense is an add-on software that provides biomechanical tools for outputting joint kinematics and centre of mass calculations. This add-on was evaluated, but not used for any of the calculations in this project because it was not released until December 2013.

2.10 Shoe Insole Pressure Measurements

The Tekscan F-Scan system consists of two instrumented insoles which are placed into a subject's shoes. Pressure measurements are made by pressure-sensitive ink that has an electrical resistance proportional to the compressive force applied to it. The insole is directly connected to a data connection hub which is attached with Velcro to the Opti-track motion capture suit. This connection is shown in Figure 2.13. The computer connected to the hub samples the insole data at a specified frequency (100 Hz). An image of the F-Scan software output is shown in Figure 2.13.

One complication with using this system on board the ship was that the sensors could not be properly calibrated before use because the ship was experiencing constant motion.

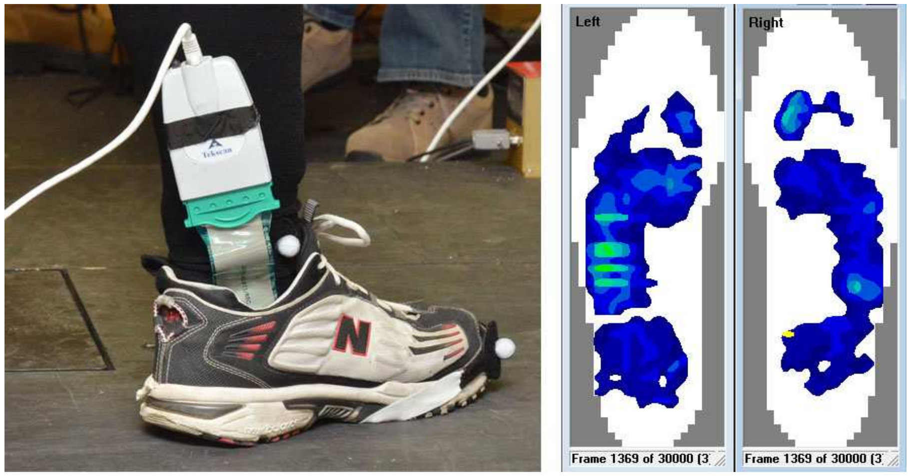

Figure 2.13: Pressure-sensing insole with connection at ankles (left) and image from F-Scan software (right).

The calibration processes require a subject to stand on one foot and not change the pressure on the insole, which was not possible in the shipboard environment.

2.11 Load Cell Measurements

Participants were required to stand on a wooden platform into which was installed an ATI Industrial six-axis load cell. This sensor was used to measure the reaction forces and moments beneath the left foot. When a participant changed the direction they were facing they were instructed to keep their left foot on the load cell plate. The load cell provided very accurate force and torque measurements which were recorded at 100 Hz. An image of the load cell installation is shown in Figure 2.14. The load cell is located beneath the black plate in the centre. While it would have been ideal to have a second load cell placed under the subject's right foot, only one sensor was available for use at the time. Additionally, the experimental platform would have required a much more complicated design in order to accommodate variable stance orientation.

Figure 2.14: Photograph of load cell plate installed in motion capture platform.

2.12 GoPro Camera Recordings

The GoPro camera is a small durable camera specially designed for making high-quality video recordings in extreme environments. Primarily it is targeted at the extreme sports and racing industries, but has been used in a wide variety of applications. It records high definition video at a variety of frame sizes and frame rates. In this experiment, it was mounted to the helmet of participants in order to record an approximation of what their eyes were seeing during the experiment. A sample image from one of the trials is shown in Figure 2.15. The primary use of the head camera data was to aid in determining how long it took for the subjects to recover from MIIs.

Figure 2.15: Sample image recorded by GoPro camera.

2.13 Data Acquisition Computers

Two laptops and a desktop computer were used to perform all of the sea trial data acquisition tasks. The desktop computer was connected to the Optitrack cameras through USB and to the load cell through a National Instruments data acquisition peripheral component interface (PCI) card. One laptop was connected to the AHRS and Xsens IMUs, and to the insoles. The other laptop was dedicated to recording the depth data from the two Kinect sensors. A photograph of the three computers is shown in Figure 2.16. The laptop on the left is running the Tekscan software and the custom IMU software that was developed for the sea trial. The middle laptop is running the iPi Recorder software, and the computer on the right is running the Arena software.

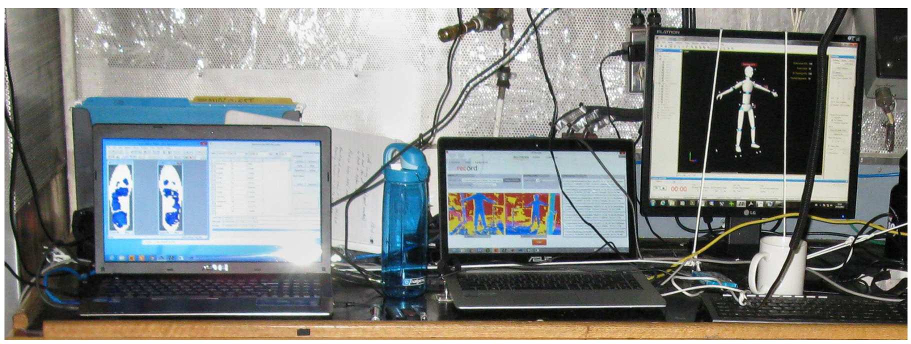

Figure 2.16: Computers used for data acquisition during the sea trial.

For redundancy, the only hardware items that were limited to a single specific computer were the Optitrack cameras and the insoles. The insoles would only work with 32-bit Windows, which was installed on one of the laptops, and the Optitrack cameras would only work with the desktop computer. The load cell could be connected to a laptop through a backup USB interface, and the kinect cameras could be connected to either laptop. The IMUs communicated over a USB connection and could be connected to any of the computers.

2.13.1 Time Synchronization

Data synchronization between sensor systems was a major consideration during the experiments, especially given that multiple sensors used their own proprietary software to make recordings, which could not all be started simultaneously. Three methods were used to synchronize the data.

1. The computers were synchronized over a network to GPS time for the latter two-thirds of the experiment.

2. At the start of each 6-minute recording session the participants were asked to stomp their left foot which was positioned on the load cell plate. This resulted in a clear data marker in both motion capture data sets, both foot pressure measurements, and in the helmet inertial sensor.

3. The helmet inertial sensor and platform inertial sensor were exactly synchronized by using the same software to record both data sets. This was necessary because the foot stomp event did not appear in the platform sensor data.

2.14 Overall Data Evaluation

As discussed earlier, many of the data acquisition technologies used in the sea trial experiments were not designed to be used in shipboard environments, and there was no existing literature on other researchers using them in that way. Overall, the sea trial experiments were very successful, but it was found that due to data acquisition complications that a considerable amount of data post-processing was required to transform the data into a useful state. The following sections will provide a brief evaluation of the condition of each set of data.

2.14.1 Motion Induced Interruptions

One of the objectives of the sea trial was to study the conditions under which motion induced interruptions occurred. Overall, it was found that unless a participant was standing at 90° with respect to ship centreline, the chances of them experiencing an MII were very low. Additionally, it was found that many of the researchers/crew who were accustomed to working in shipboard environments, experienced very few or no occurrences at all. This limited the data analysis that was able to be performed on causes of MIIs.

2.14.2 Motion Capture Data

Once the Kinect depth recordings had been processed into skeletal motion capture data, the quality of the recordings were compared to the Optitrack recordings. It was found that all of the Optitrack recordings would require a significant amount of post processing time for the reasons discussed in Section 2.8. Therefore it was decided to use only the Kinect motion capture data for this project.

2.14.3 Foot Pressure Data

Both the insoles and the load cell performed reasonably well under the continuously-evolving sea conditions. Overall, the load cell data was of much higher quality than the insoles, but was limited to just the left foot. As discussed in Section 2.10, it was not possible to properly calibrate the insoles during the sea trial. In order to accommodate this, the load cell data was used to calibrate the left insole data, and a dynamics model of the ship-human system was used to calibrate the right insole data. The exact calibration procedure is described in detail in Chapter 3.

2.14.4 Inertial Measurements

The AHRS measurements of ship motion on the experimental platform were generally very good. There were however several recordings early in the sea trial when the sensor was not recording properly. Fortunately, there was supplementary data available from the additional IMU located in the same room that was recording data for DRDC-Atlantic. This data was able to be substituted for the AHRS recordings, although since Carleton's and DRDC-Atlantic's systems were not time-synchronized until later in the sea trial, it was necessary to cross-correlate IMU motions measured by each sensor in order to time-synchronize them. Details on this procedure are documented in the next chapter.

The head-mounted IMU worked as intended for its role in time-synchronizing the AHRS IMU to the rest of the recordings. Unfortunately the head-IMU-specific measurements were not useful as vestibular-equivalent measurements since it was determined after the sea trial that it was not possible to easily determine the orientation of the IMU with respect to the subject's head due to relative motion between the subject's helmet and head.

2.14.5 Video Recordings

One of reasons that the head-mounted GoPro camera was included as part of the experiment instrumentation was that there is considerable research that shows that vision plays a role in human balance. Due to the constraint of the participants being required to perform the cognitive task, it is believed that this contribution was significantly diminished because the participants would have been mainly focused on the clipboard or tablet, rather than the surrounding environment. Also, due to the geometric limitations of the head mount and the inability of being able to see the output of the camera while mounted, it was not possible to ensure that the camera was receiving the same input as the subject's eyes. Additionally, since the lab space was entirely indoors, it is not clear how the subjects would be using this information to maintain balance since they would not be able to see a stationary reference.

2.14.6 Future Work

While it was beyond the scope of this research project, it might be possible in the future to fuse together the various data recordings related to the head motion in order to obtain an accurate measurement of the head orientation during the sea trial experiments. This analysis could include:

1. Kinect head tracking data;
2. helmet markers that were visible in the Opti-track data;
3. head inertial measurements with unknown frame of reference; and
4. relative head positions determined from GoPro recordings.

Chapter 3

Sea Trial Data Processing and Analysis

3.1 Introduction

The objective of this chapter is to present how the sea trial data from the IMUs, the foot pressure sensors, and the motion capture were combined in order to provide a comprehensive picture of how each subject responded to ship motion.

A common analysis in this subject area is to study the motion of the centre of mass (CoM) and the centre of force (CoF) within the base of support (BoS). Traditionally the BoS is considered to be the area encompassed by a person's stance, and that as long as the CoM is contained within the BoS then postural stability is guaranteed. More recent research has shown that it is a combination of position and velocity of the CoM and the reaction moment required to maintain upright stance that contributes to postural stability [50] whereby if the combination of the two provides a situation where a person's muscular forces cannot keep the CoM within the BoS, a step will be required in order to maintain upright stability.

This chapter will present the calculations that were required to process the sea trial data into a form that allowed the analysis of the motion of the CoM and CoF within the BoS. First it will discuss the ship IMU data, which was measured in its own coordinate system and contained significant noise. There was also an error with the primary IMU early in the sea trial that resulted in erroneous data being recorded. In order to accommodate this, some ship motion data had to be synchronized and substituted from an auxiliary sensor. Next, the format of the motion capture data, and the method used to extract foot positions and CoM kinematics will be presented. This is followed by the processing of the load cell data.

Next, a simplified human body dynamic model will be derived both in 2D and in 3D in order to use the available data to estimate the mass of each subject. Once that is done, the 3D model is also used to estimate the vertical force under the right foot, by using the data measured by the load cell, which was located under the left foot. Both data sets are then used to determine calibration coefficients for the insole data for each participant.

The next part of this chapter takes a closer look at the data from the insoles, after it has been calibrated. The data recorded from each participant is combined in such a way that it allows an outline of their footprint to be calculated. These outlines are combined with the foot position data from the motion capture to place them the proper distance apart, and then connecting lines are added between them to arrive at a plot of the BoS of each subject. The location of the CoM and CoF are also added to the plot so that their relative motion within the BoS can be studied. Finally, the chapter concludes by analyzing the CoM kinematics for a few participants who experienced several MIIs.

3.2 IMU Data

When analyzing the dynamics of human subjects in a shipboard environment, it is necessary to include the kinematics of the ship motion, and the human-ship interaction forces. Three IMUs were used to record motion data during the experiment. The main source was the AHRS sensor that was placed in the corner of the platform upon which the experiments took place. The second was a NAV sensor which was located in the same laboratory space near one of the walls. The third sensor was the Xsens IMU that was attached to the helmet that participants were required to wear during the experiments. Its data were primarily used to synchronize the ship-mounted IMUs to the data recorded by the body-attached sensors.

3.2.1 AHRS Data

The Attitute Heading Reference System (AHRS) is an inertial sensor that was placed near the feet of participants in order to measure the translational accelerations and angular velocities that each participant experienced. Processing of this data involved filtering noisy data, differentiating angular velocities to obtain accelerations, and conversion of the data from the AHRS coordinate conventions to ship motion conventions expected by the simulations that use it. If they were required, ship translational velocities and displacements could be calculated by integrating the translational accelerations with respect to time. The sequence and units of the AHRS data and the format expected by the simulations that use the AHRS data are shown in Figure 3.1. The greyed-out portions are not currently calculated since they are not used in the simulation or analysis but the ship motion files still contain placeholder values.

The first step in processing the data was to subtract the components of gravity from the translational accelerations if required. When used with dynamics simulations that

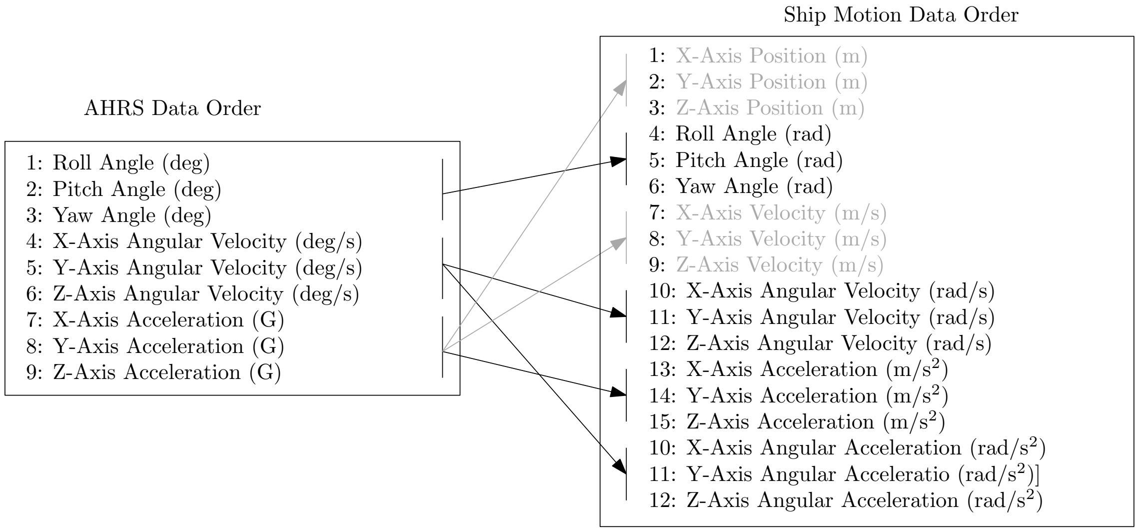

Figure 3.1: Data order and units for AHRS data and ship motion data.

include gravity terms, the components of IMU acceleration due to gravity need to be subtracted, since gravity terms are included in the formulation and change depending on the subject's body orientation. Alternatively, later in this chapter, an analysis is presented that computes the equations of motion of the subject in such a way that the ship accelerations with gravity included are one of the model's inputs.

The transformation from local to global coordinates for the AHRS data for a specific sensor orientation is:

$$\mathbf{R}^{LG} = \begin{bmatrix} \mathrm{c}(\theta_y)\mathrm{c}(\theta_z) & \mathrm{c}(\theta_y)\mathrm{s}(\theta_z) & -\mathrm{s}(\theta_y) \\ \mathrm{s}(\theta_x)\mathrm{s}(\theta_y)\mathrm{c}(\theta_z)-\mathrm{c}(\theta_x)\mathrm{s}(\theta_z) & \mathrm{s}(\theta_x)\mathrm{s}(\theta_y)\mathrm{s}(\theta_z)+\mathrm{c}(\theta_x)\mathrm{c}(\theta_z) & \mathrm{s}(\theta_x)\mathrm{c}(\theta_y) \\ \mathrm{c}(\theta_x)\mathrm{s}(\theta_y)\mathrm{c}(\theta_z)+\mathrm{s}(\theta_x)\mathrm{s}(\theta_z) & \mathrm{c}(\theta_x)\mathrm{s}(\theta_y)\mathrm{s}(\theta_z)-\mathrm{s}(\theta_x)\mathrm{c}(\theta_z) & \mathrm{c}(\theta_x)\mathrm{c}(\theta_y) \end{bmatrix} \tag{3.1}$$

The gravity vector in inertial coordinates was transformed to local IMU coordinates using the transpose of Equation 3.1 and subtracted from the acceleration data at each time stamp. Samples of the original data and data with gravity subtracted are shown in Figure 3.2.

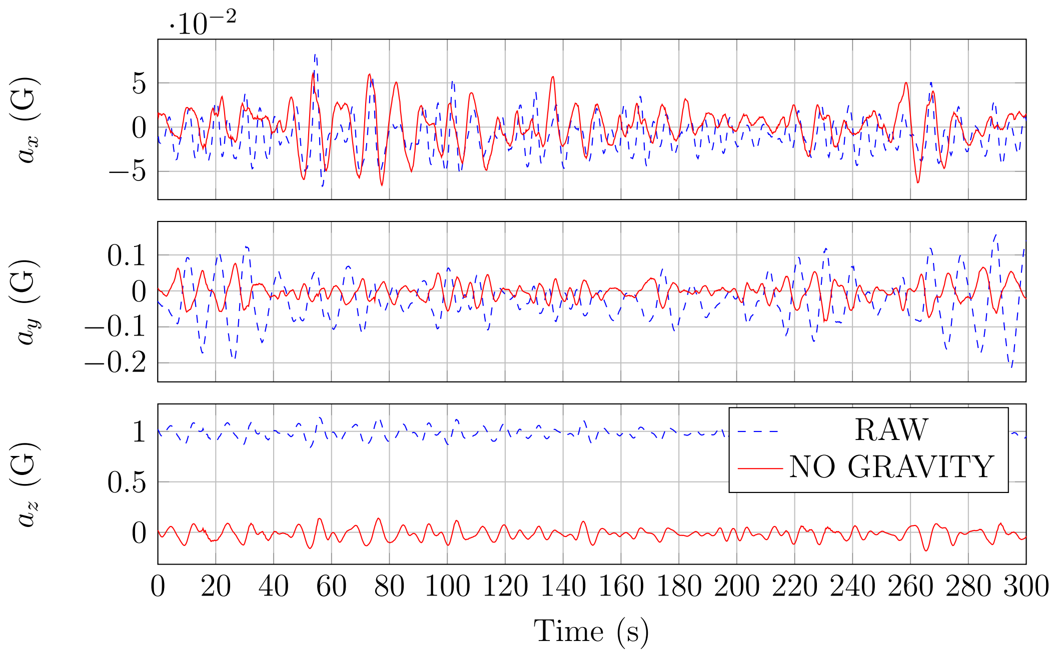

Figure 3.2: AHRS acceleration data with and without the components of gravitational acceleration.

Filtering

Next, the data was low-pass filtered and converted from G to m/s^2. Figure 3.3 shows an example of the effectiveness of filtering at smoothing the acceleration data.

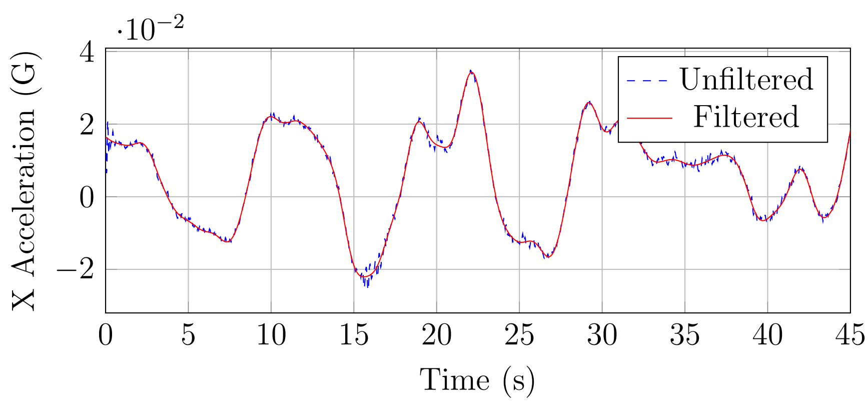

Figure 3.3: Filtered and unfiltered X-axis acceleration data.

A ninth-order zero-phase Butterworth filter was used to filter the data. This filter was chosen over a lower-order filter because it was found that lower-order filters had a tendency to significantly diminish the minimums and maximums of the data. This filter was used for every case of low-pass filtering in this thesis. The cutoff frequency was chosen using a method described in [51], which is designed to provide the optimum balance between noise and signal. All of the cutoff frequencies that were derived for processing the sea trial data, were determined using this method, which will now be briefly presented.

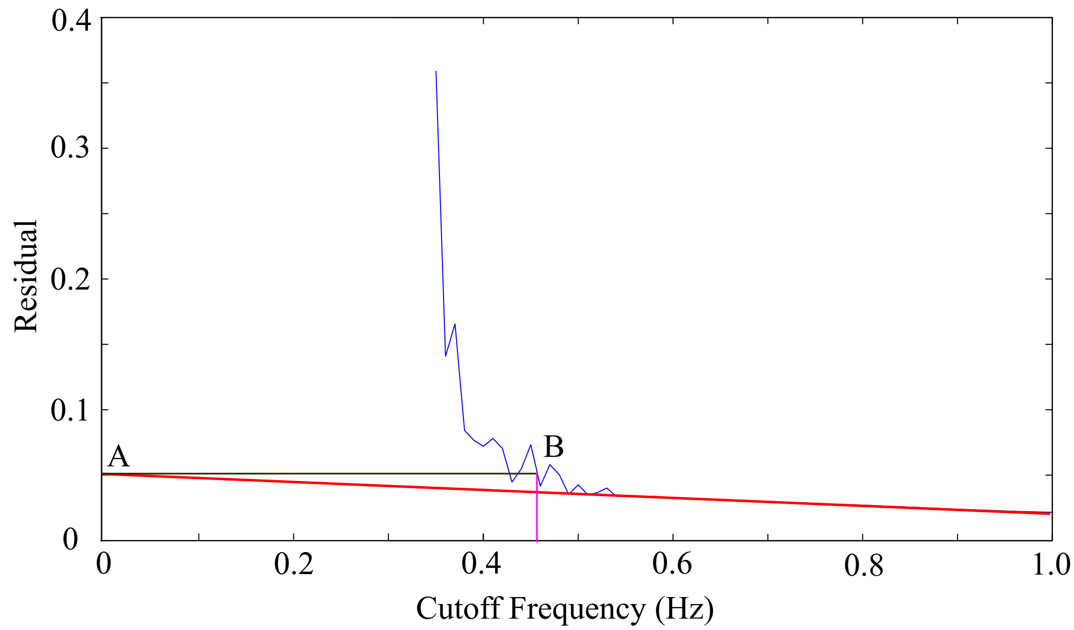

Figure 3.4: Data filtering residual with Butterworth filter at various cutoff frequencies, and lines used to determine optimal cutoff frequency.

The graph in Figure 3.4 shows the residual between the filtered and raw roll motion data at various cutoff frequencies. The residual is the root mean square (RMS) of the differences between the two data sets. In order to determine the cutoff frequency which offered the best compromise between reduction of noise and maintenance of the data signal, the following steps were taken.

1. Draw a line parallel to the linear portion which intersects the Y-axis (the red line in Figure 3.4).

2. Draw a horizontal line from the Y-axis intersection in the previous step so that it intersects the data curve (the black line from A to B in Figure 3.4.

3. Draw a vertical line from point B to the horizontal axis (the magenta line in Figure 3.4). This X-axis intersection is the cutoff value which provides the optimal balance between data accuracy and noise reduction.

In the case of Figure 3.4, the optimal cutoff frequency is approximately 0.5 Hz. For simulation purposes it is generally better to round down to a lower cutoff frequency because that results in smoother data. Each cutoff frequency selected using this method was manually verified by plotting the filtered and unfiltered data together. Fine-adjustments to their values were made if necessary. Optimal cutoff frequencies for measured and calculated inertial sensor measurements are shown in Table 3.1.

Measurement	Cutoff Frequency (Hz)
Roll Angle	0.5
Pitch Angle	0.7
Yaw Angle	0.6
X Ang Velocity	0.5
Y Ang Velocity	0.4
Z Ang Velocity	0.4
X Acceleration	0.7
Y Acceleration	0.7
Z Acceleration	0.7

Table 3.1: Cutoff frequencies for filtering ship motion sensor data.

The next step in processing the AHRS data was to filter the orientation and angular velocity data. Figures 3.5 and 3.6 show samples of the effectiveness of these filters.

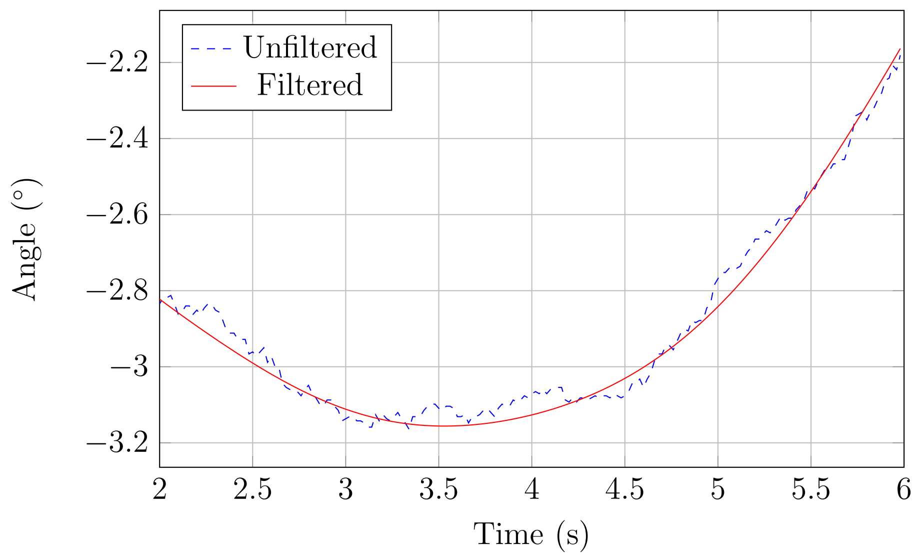

Figure 3.5: Filtered and unfiltered roll angle data.

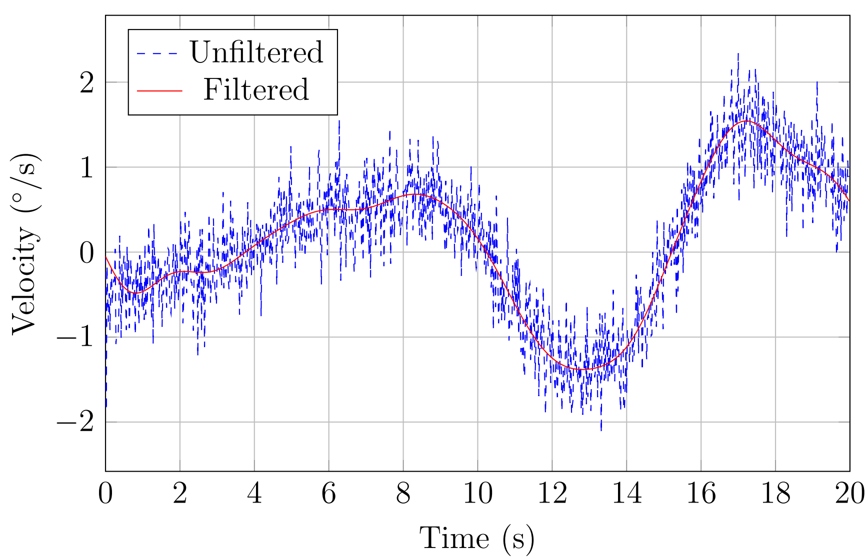

Figure 3.6: Filtered and unfiltered roll angular velocity data.

The next step was to calculate angular accelerations by numerically differentiating the angular velocities with respect to time. This was accomplished using central-differentiation of order $O(h^4)$ [52] defined by:

$$\left(\frac{\mathrm{d}}{\mathrm{dt}}f\right)_n = \frac{-f_{n+2} + 8f_{n+1} - f_{n-1} + f_{n-2}}{12(t_n - t_{n-1})} \tag{3.2}$$

Coordinate Conventions

The AHRS inertial sensor has its own coordinate system which is different from the one used by the models developed in this thesis. The AHRS convention is to have X positive forward, Z positive down, and Y positive to the right. The convention for the models is to have X positive forward, Z positive up, and Y positive to the left. The two coordinate systems are shown in Figure 3.7.

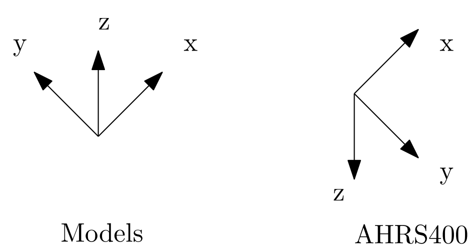

Figure 3.7: Alignment of thesis model coordinate system and AHRS400 coordinate system.

The AHRS also uses a different angle convention in that it uses ZYX Euler angles rather than XYZ Euler angles which is the selected convention for this thesis. The simplest method of dealing with this data is to transform the data into the model coordinates. The transformation between coordinate systems is:

$$\mathbf{T}^{AHRS} = \begin{bmatrix} 1 & 0 & 0 \\ 0 & -1 & 0 \\ 0 & 0 & -1 \end{bmatrix} \tag{3.3}$$

Each of the linear accelerations, angular velocities, and angular accelerations was multiplied by $\mathbf{T}^{AHRS}$. The relationship between the angular transformation matrices of the two coordinate systems is:

$$\mathbf{R}_{xyz} = (\mathbf{T}^{AHRS})^T \mathbf{R}_{zyx} \mathbf{T}^{AHRS} \tag{3.4}$$

The XYZ Euler angles could then be calculated from $\mathbf{R}_{xyz}$ using the following relationships [53]:

$$\begin{aligned} \theta_y &= \operatorname{asin}(a_{1,3}) \\ \theta_x &= \operatorname{asin}\left(\tfrac{-a_{2,3}}{\cos(\theta_y)}\right) \\ \theta_z &= \operatorname{asin}\left(\tfrac{-a_{1,2}}{\cos(\theta_y)}\right) \end{aligned} \tag{3.5}$$

where $a_{i,j}$ is the entry in $\mathbf{R}_{xyz}$ corresponding to row i and column j.

3.2.2 NAV Data

The NAV sensor is the IMU that was used by DRDC-Atlantic during the sea trial for logging ship motion. It was located in the laboratory space where the human postural stability experiments took place but was not placed next to the participants like the AHRS sensor. For the first few days of the sea trial, when data was collected for the first two participants, the AHRS sensor was not recording properly due to a software error. A sample of this faulty data is shown in Figure 3.8. Therefore, in order to acquire ship motions for those trials it was necessary to use the NAV data. Unfortunately, at that point in the trial, Carleton and DRDC's equipment were not time synchronized so some calculations were required in order to determine the time offsets between data sets. These calculations involved performing a cross-correlation between the two data sets to determine their time offset, and using the AHRS data start and end times to locate the corresponding data sets in the NAV recordings. Additional details are provided below.

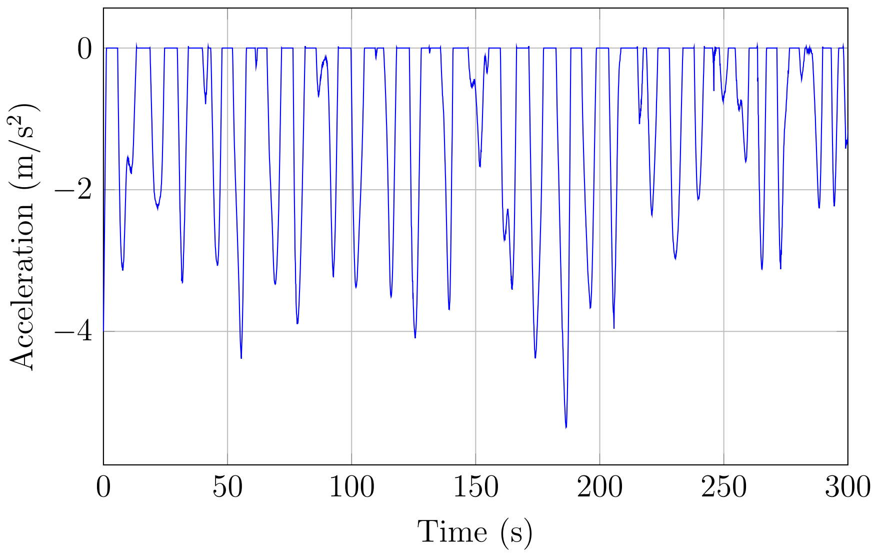

Figure 3.8: Faulty AHRS acceleration data.

The AHRS recordings are a set of approximately 6-minute data recordings made at irregular intervals; while the NAV data recordings are a set of continuous 20-minute recordings. While many of the time intervals of the AHRS recordings were fully contained within the boundaries of the NAV recordings, there were a few that were not. Therefore the first step was to load all of the NAV recordings associated with a specific participant's trials to form one continuous data recording.

The next step was to perform a cross-correlation between one of the angular parameters in each data set. In most cases pitch angle was used because it provided consistent, clear results. Sample results of this are shown in Figure 3.9. A cross-correlation compares how close two data sets are to each other at every possible time offset between the two data sets where there is overlap. If the differences between the data sets are small, the magnitude of the correlation will be large. Alternatively, if the data sets are very different, the magnitude

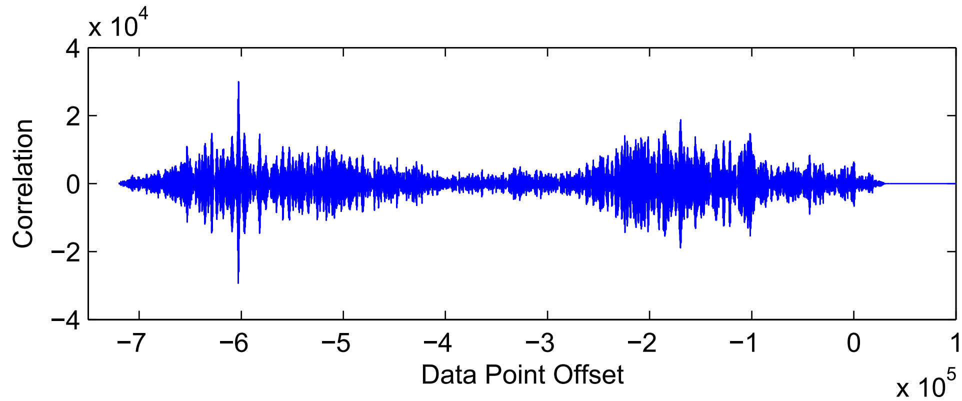

Figure 3.9: Cross-correlation between NAV and AHRS data.

of the correlation will be very small. Following this logic, after the correlation has been calculated at every possible time-offset between the two data sets, the maximum correlation magnitude should correspond to the actual time offset between the two data sets.

In Figure 3.9 it is clear that near a data offset of -6$\times 10^5$ there is a maximum correlation. Due to the oscillatory and repetitive nature of the IMU data, there were a few cases where there were several correlations of equally large magnitude where the largest did not correspond to the correct time offset. These cases were identified manually on visual inspection of the results. In order to fix this problem, roll angle was used instead of pitch angle for those particular correlations. The reason why roll angle was not used for every case, is that there were more cases where roll angle gave the incorrect time offset than for pitch angle. Fortunately, there were no cases where both pitch and roll angle cross-correlations indicated incorrect time offsets.

Because of these issues with the cross-correlations, there was a possibility that the AHRS was not recording angles properly because of significant differences between the two data sets, even when using the correct time offset. In order to investigate this issue, AHRS and NAV data sets were compared from later in the sea trial when the issues with the AHRS had been resolved. No significant differences between the data sets were observed in those cases.

Figure 3.10 shows the result of all of the cross-correlations for a two-hour recording session. The fact that all of the recordings align chronologically is indicative of the algorithm performing correctly.

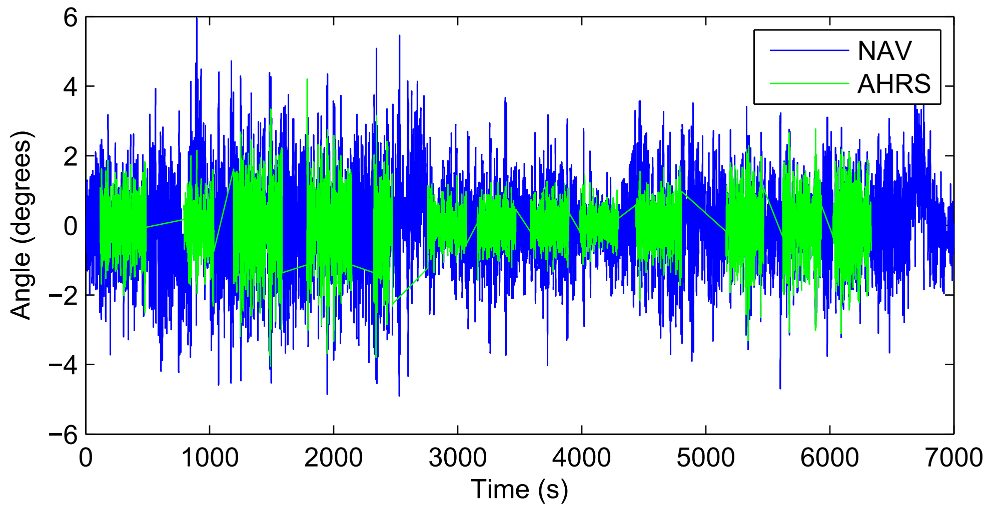

Figure 3.10: Synchronized NAV data overlapped on AHRS data.

3.2.3 Head IMU Data

As discussed in Section 2.14.4, it was not possible to directly use the Xsens head IMU data in the model since the relative orientation between the sensor and the subject's head was not measured. The Xsens data was still useful, however, for determining the time offset between the AHRS recordings and other data sources because the data from both sensors was recorded with the same software that was custom-written for the sea trial. A sample of vertical acceleration data taken from the Xsens sensor is shown in Figure 3.11. In the figure, there is a clear maximum in the Z-acceleration data at 7 seconds that indicates when the subject stomped their foot on the load cell.

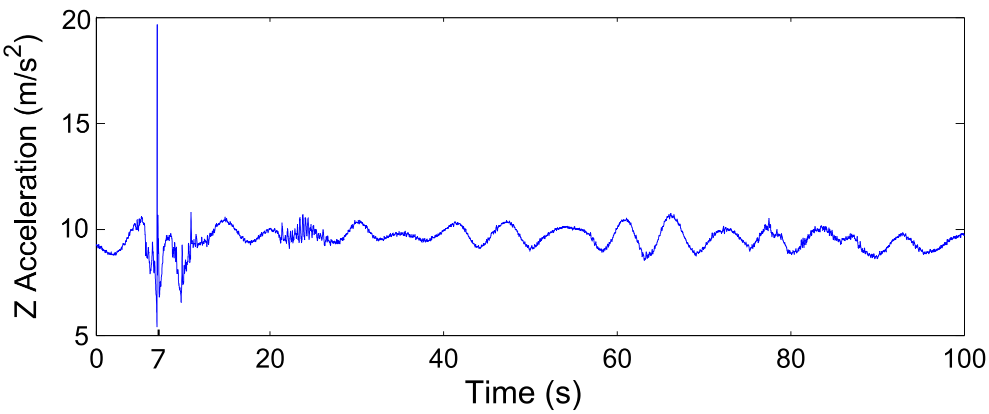

Figure 3.11: Vertical acceleration data from the start of a trial measured by Xsens IMU.

3.3 Kinect Motion Capture Data

Motion tracking data was recorded using two Microsoft Kinect sensors and an iPi Studio software package. The software's proprietary algorithms map depth data recordings from the two sensors onto a model of a human skeleton. A sample of the skeleton model used is shown in Figure 3.12.

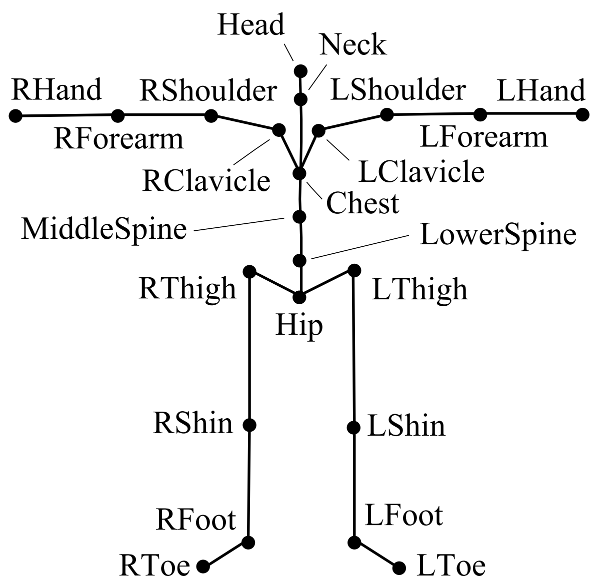

Figure 3.12: Human skeletal structure output by iPi Studio software.

3.3.1 BVH File Format

Since the iPi Studio software is primarily marketed at the animation industry, it can output its data to a variety of file formats. The output format that was selected for this project is an ASCII-readable format that uses the .BVH extension. It was invented by a motion capture services company called Biovision which no longer exists, but the format in some form is supported by most software packages that are used to animate skeletal characters. The file format includes support for defining a chain-like skeleton structure and how the positions and orientations of the skeleton structure change with time.

The BVH file format is a tab-separated ASCII file format that is divided into two separate portions. The first part starts with 'HIERARCHY'. This section contains a list of all of the joints in the skeletal model. It is organized such that there is one 'ROOT' joint (typically the hips) and all other joints are defined relative to that joint or to each other. Each 'JOINT' has a unique name and each chain of joints ends with an 'End Site'. Each joint defines its offset relative to its parent joint with components defined in the coordinate system of the parent joint.

Each joint also defines a list of 'CHANNELS'. These are its properties that can be changed over time. The six possible channels are: Xposition, Yposition, Zposition, Xrotation, Yrotation, and Zrotation. Typically the root joint records all six and all subsequent joints record only rotations since bones typically do not change in length over time. The order of the rotation channels specifies the order in which the rotations should be performed. End sites do not contain any channels since they represent points on a rigid body that also included the preceding joint.

After the joint hierarchy is the MOTION section. The first line of this section defines the number of frames in the recording (eg. "Frames: 9001"). The second line of the section defines the amount of time that elapses in each frame in seconds (eg. "Frame Time: 0.0333333").

Each subsequent line of the file contains the data for a single frame. One line contains a list of tab-separated values corresponding to the order that channels are presented in the hierarchy section. Units are not defined anywhere in the file format, but it appears to be common for units to be in centimetres and degrees.

3.3.2 BVH Joint Conventions

In iPi Studio's BVH files the XYZ Euler angle rotation convention is used. The rotations are defined the body-fixed coordinates of each body segment. In matrix form this transformation can be written as:

$$\mathbf{R} = \begin{bmatrix} 1 & 0 & 0 \\ 0 & \cos(\theta_x) & -\sin(\theta_x) \\ 0 & \sin(\theta_x) & \cos(\theta_x) \end{bmatrix} \begin{bmatrix} \cos(\theta_y) & 0 & \sin(\theta_y) \\ 0 & 1 & 0 \\ -\sin(\theta_y) & 0 & \cos(\theta_y) \end{bmatrix} \begin{bmatrix} \cos(\theta_z) & -\sin(\theta_z) & 0 \\ \sin(\theta_z) & \cos(\theta_z) & 0 \\ 0 & 0 & 1 \end{bmatrix} \tag{3.6}$$

Since the rotations only define the relative orientation between two adjacent coordinate systems, multiple transformations must be combined in order to determine the absolute position of any joint that is more than one segment away from the root joint. A sample joint position calculation combining multiple sequentially-chained joints labelled as A, B, C, and D could be written as:

$$^0\mathbf{r}_D = \mathbf{R}^{a0}(^a\mathbf{r}_{B/A}) + \mathbf{R}^{a0}\mathbf{R}^{ba}(^b\mathbf{r}_{C/B}) + \mathbf{R}^{a0}\mathbf{R}^{ba}\mathbf{R}^{cb}(^c\mathbf{r}_{D/C}) \tag{3.7}$$

where the uppercase subscripts indicate relative joint positions and the lowercase superscripts indicate which coordinate system they are defined in. Calculation of points using this equation is useful if one wishes to know all of the intermediate coordinates. A more computationally-efficient procedure, if only the end point is required, is to calculate $\mathbf{r}_D$ as:

$$^0\mathbf{r}_D = \mathbf{R}^{a0}[(^a\mathbf{r}_{B/A}) + \mathbf{R}^{ba}[(^b\mathbf{r}_{C/B}) + \mathbf{R}^{cb}(^c\mathbf{r}_{D/C})]] \tag{3.8}$$

Using this form, the right and left ankle positions in the ship frame can be calculated directly from the BVH data file as:

$$\mathbf{r}_{RFoot/ship} = \mathbf{r}_{Hip} + \mathbf{R}_{Hip}(\mathbf{r}_{RThigh} + \mathbf{R}_{RThigh}(\mathbf{r}_{RShin} + \mathbf{R}_{RShin}(\mathbf{r}_{RFoot}))) \tag{3.9}$$

$$\mathbf{r}_{LFoot/ship} = \mathbf{r}_{Hip} + \mathbf{R}_{Hip}(\mathbf{r}_{LThigh} + \mathbf{R}_{LThigh}(\mathbf{r}_{LShin} + \mathbf{R}_{LShin}(\mathbf{r}_{LFoot}))) \tag{3.10}$$

The BVH coordinate system used by iPi Studio does not align with the coordinate system used by the models in this thesis. The two coordinate systems are aligned as shown in Figure 3.13.

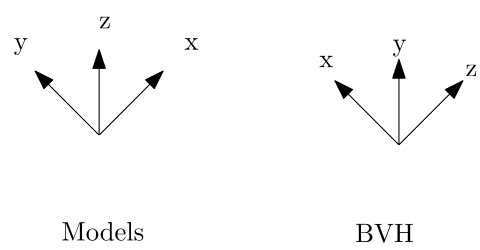

Figure 3.13: Alignment of thesis model coordinate system and iPi Studio BVH coordinate system.

It is necessary to follow the same procedure described in Section 3.2.1 to transform the BVH data into the model coordinate system. The only difference is that the transformation matrix is as follows:

$$\mathbf{T}^{BVH} = \begin{bmatrix} 0 & 0 & 1 \\ 1 & 0 & 0 \\ 0 & 1 & 0 \end{bmatrix} \tag{3.11}$$

3.3.3 Centre of Mass Estimation

One of the useful metrics that can be derived from the motion capture data is the location of the body centre of mass (CoM) at each time step. This is done by calculating the CoM of each part of the body, and then combining them with a weighted average, where the weights are the percentage of the total body mass that each part contains.

Most models of the human body assume that the CoM of each segment of the body is located along its axial centreline. For example, if one were to draw a line from the shoulder to the elbow, the upper arm's CoM would be located a fixed distance along that line. That distance is referred to as the proximal distance when measured from an inboard joint, in this case the shoulder, and referred to as the distal distance when measured from an outboard joint, in this case the elbow. Written in mathematical form, if $\mathbf{r}_1$ is the position of the inboard joint, and $\mathbf{r}_2$ is the position of the outboard joint, then the centre of mass location for that body segment can be formulated as:

$$\mathbf{r}_m^k = \mathbf{r}_1^k + (\mathbf{r}_2^k - \mathbf{r}_1^k)d^k \tag{3.12}$$

where d^k is the proximal distance as a fraction of the total segment length. The total body centre of mass can then be calculated as:

$$\mathbf{r}_{CoM} = \sum \mathbf{r}_m^k \; m_f^k \tag{3.13}$$

where m_f^k is the mass fraction of body segment k and $\mathbf{r}_m^k$ is the position of the segment's CoM in the body frame. Mass fraction is the mass of body segment k divided by the total body mass.

The proximal body segment distances and mass fractions used were taken from literature [51] and are shown in Table 3.2. The data in the table was compiled from the results of several different investigators. The start and end joint names follow the conventions used in the iPi Studio BVH data recordings.

In addition to calculating overall CoM, Equation 3.13 can also be used to calculate subset centres of mass. This is useful if one wishes to study the motion of groups of joints, rather than overall body motions. Since the project objective is to study human motion as a four-link inverted pendulum, body segments were grouped together into four sections as indicated in the last column of Table 3.2. A diagram which illustrates this grouping is shown in Figure 3.14.

For each subject, the left and right global ankle positions, and total body CoM were calculated and low-pass filtered with a cutoff frequency of 0.4 Hz. The CoM positions were

Table 3.2: Body segment proximal distances, mass fractions, and inverted pendulum link assignments.

Segment	Start Joint	End Joint	Prox. Dist.	Mass. Frac.	IP Link
Left forearm	LForearm	LFinger22	0.682	0.0220	3
Right forearm	RForearm	RFinger22	0.682	0.0220	3
Left upper arm	LShoulder	LForearm	0.436	0.0280	3
Right upper arm	RShoulder	RForearm	0.436	0.0280	3
Left foot	LFoot	LToe	0.500	0.0145	1
Right foot	RFoot	RToe	0.500	0.0145	1
Left lower leg	LShin	LFoot	0.433	0.0465	1
Right lower leg	RShin	RFoot	0.433	0.0465	1
Left upper leg	LThigh	LShin	0.433	0.1	2
Right upper leg	RThigh	RShin	0.433	0.1	2
Head	Head	Head	0	0.0810	4
Trunk	LowerSpine	Neck	0.500	0.497	3

then differentiated in order to obtain CoM velocities and accelerations. After each differentiation the data was again low-pass filtered because numerical differentiation of noisy data accentuates the noise. Differentiation was performed using the same central difference formula presented in Equation 3.2 and low-pass filtered using the cutoff frequencies that are shown in Table 3.3.

Measurement	Cutoff Frequency
XYZ Positions	0.4
X Velocity	0.5
Y Velocity	0.9
Z Velocity	0.5
X Acceleration	0.6
Y Acceleration	2.0
Z Acceleration	0.5

Table 3.3: Body segment proximal distances and mass fractions.

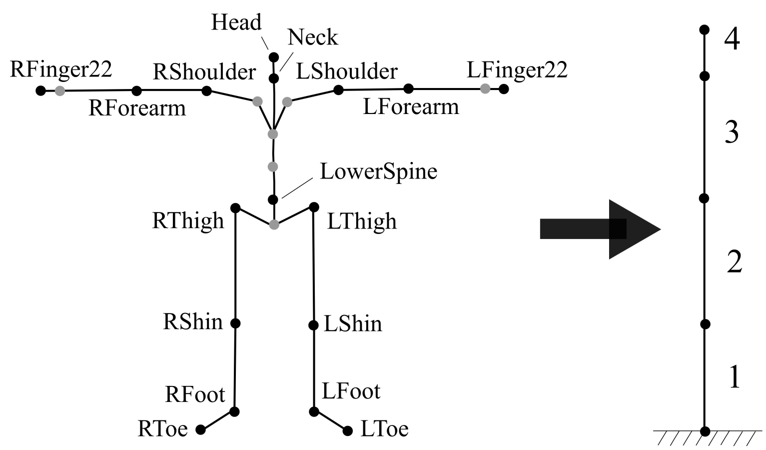

Figure 3.14: Grouping of BVH segments to inverted pendulum links.

3.4 Calibration of Insole Data

As was discussed in Section 2.14.4, the insole data could not be calibrated during the sea trial experiments due to the requirement of needing to apply a constant pressure to the insole over a set period of time. This section will describe how this problem was dealt with, and is divided into three parts. The first part will briefly discuss some post-processing steps that were applied to the load cell data. The next part will present how the load cell data, the motion capture data, and the IMU data were combined in order to estimate the mass of each participant. The final part of this section will present how the load cell data was used to calibrate the data measured by the insoles.

3.4.1 Load Cell Data

The load cell data required minimal processing before it could be used. One calculation that was required was to rotate the data from the instrument's frame to the model frame. The relative orientation of these two coordinate frames is shown in Figure 3.15.

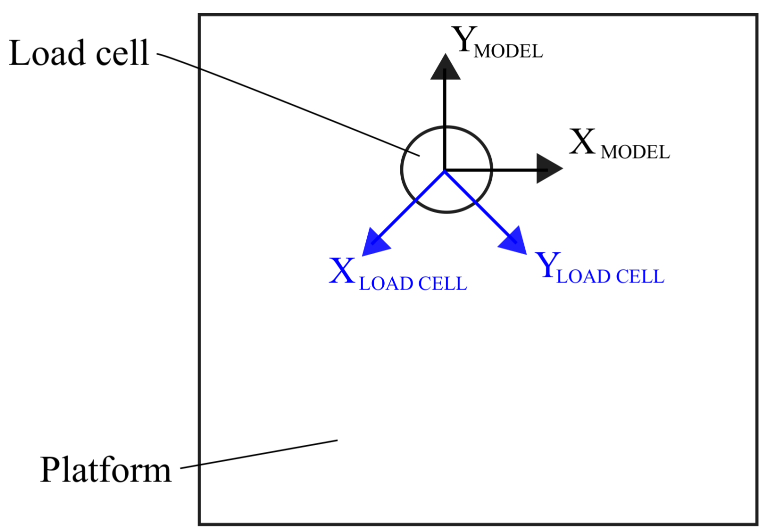

Figure 3.15: Orientation of load cell and model coordinate frames.

In order to align the two frames, the load cell data had be rotated 135° about its Z axis.

For example, if the force or moment vector of the load cell data is written as $\mathbf{f}_{LC}$ and the rotation as $\mathbf{R}_z$, then the load cell data in the model frame could be calculated as:

$$\mathbf{f}_{MODEL} = \mathbf{R}_z \mathbf{f}_{LC} \tag{3.14}$$

where:

$$\mathbf{R} = \begin{bmatrix} \cos(135°) & -\sin(135°) & 0 \\ \sin(135°) & \cos(135°) & 0 \\ 0 & 0 & 1 \end{bmatrix} \tag{3.15}$$

The load cell software samples the load cell's instruments at 1000 Hz and then averages the results to output a result at 100 Hz. In order to determine whether further data filtering was necessary, the data was low-pass filtered with the cutoff frequencies listed in Table 3.4. Figures 3.16 and 3.17 show sample filtering of force and moment data. Similar results were obtained in all coordinate directions. After performing the calculations presented in the next section, with and without the load cell data filtered, no significant differences were observed in the results.

Measurement	Cutoff Frequency (Hz)	Data File Order
X-Axis Force	2.0	2
Y-Axis Force	2.4	3
Z-Axis Force	2.2	4
X-Axis Moment	2.6	5
Y-Axis Moment	2.7	6
Z-Axis Moment	3.0	7

Table 3.4: Cutoff frequencies for filtering load cell data.

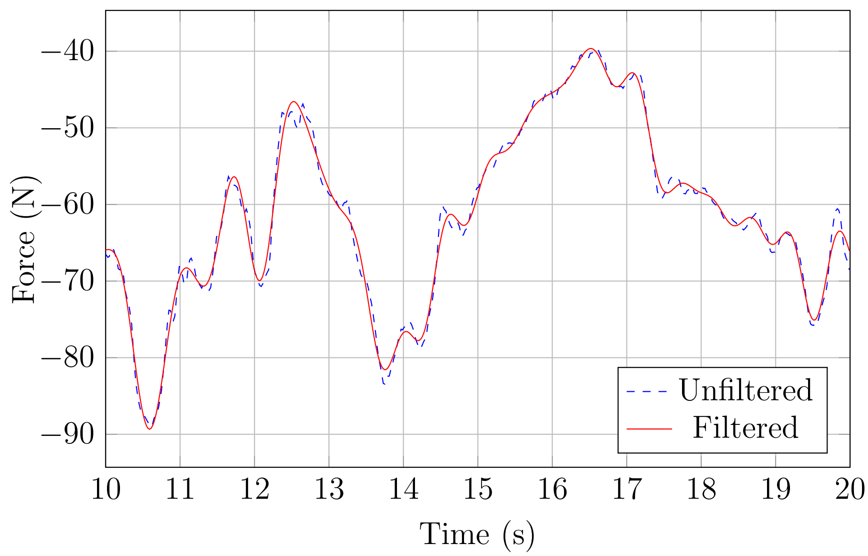

Figure 3.16: Filtered and unfiltered X-axis load cell force data.

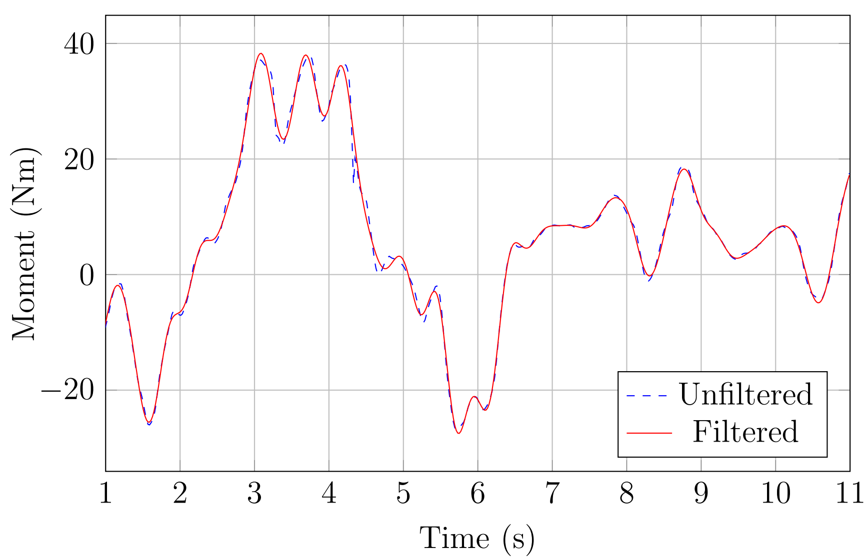

Figure 3.17: Filtered and unfiltered X-axis load cell moment data.

3.4.2 Subject Mass Estimation

The originally-intended method for calibration of the insole data was to have a subject stand with both feet on the load cell at the start of each experiment since the load cell did not require special considerations for calibration. This method was not ideal, but would have provided force data that could be correlated to the insole data. Unfortunately, it was determined after the sea trial that this method would not be feasible because the data recordings that were made were not of sufficient length and the ship motions were not recorded by the AHRS at the same time. It was not possible to use the NAV data because the start times of the load cell recordings were not sufficiently accurate to synchronize the data with enough accuracy (within 0.1 seconds or better). In order to accommodate these issues, an alternate method of calibration of the insole data was derived based on body position and ship dynamics.

An additional issue with the load cell calibration trials is that they were also intended to be used to calculate participant masses, which need to be known to calibrate the insoles. Therefore, the method described in this section will first estimate the mass of a participant, and then in the next section the insole data calibration will be described. A 2D version will first be presented, followed by an expanded 3D analysis.

When a person on the ship is standing oriented at zero degrees with respect to the ship centreline and ship pitch and yaw angles are neglected, the person can be modelled as shown in Figure 3.18.

In the figure, a_y and a_z are the acceleration components of the CoM of the person in the Y and Z directions respectively. If relative motion between the person and the ship is assumed to be negligible, as well as the distance between the inertial sensor and the person's CoM, then a_y and a_z are equivalent to accelerations measured by the inertial sensor, ignoring small acceleration contributions arising from ship rotations. The forces N_L, N_R, F_L, F_R, M_L, and M_R are the reaction forces and moments between the person

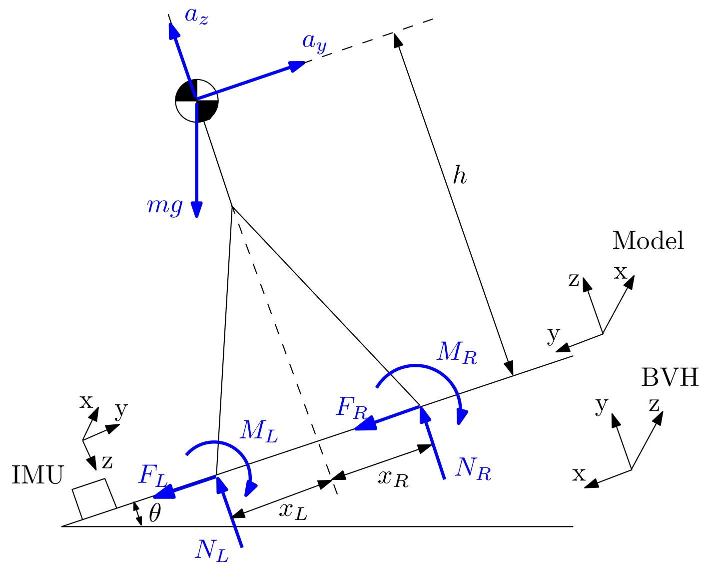

Figure 3.18: Two-dimensional model of person standing at 0° with respect to ship centreline.

and the ship deck. The values of N_L and F_L are measured by the load cell, and the values of N_R, F_R, M_L, and M_R are unknown. The values x_L and x_R are the distances from the body CoM to the left and right feet, respectively. These can be calculated by extracting the CoM and feet positions from the BVH data. The value h is the vertical distance from the ship deck to the CoM, and can also be extracted from the BVH data. The value of mg is the weight of the person. The coordinate axes of the AHRS ship data and the BVH motion capture data are not aligned so they are also placed in the diagram for reference. Figure 3.19 shows the kinematics that can be determined from the AHRS data, where $\mathbf{A}$ is the translational acceleration, $\mathbf{\Omega}$ is the angular velocity, and $\mathbf{\Lambda}$ is the angular acceleration.

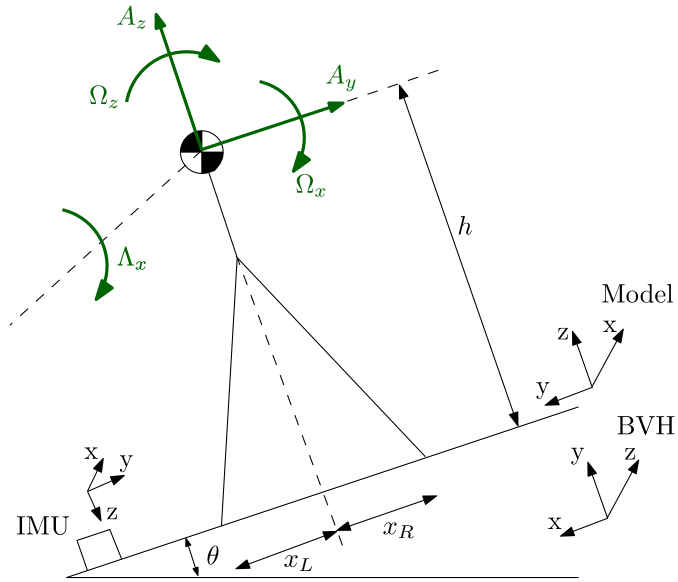

Figure 3.19: Ship motions measured by AHRS relevant to 2D model.

Using the Newton-Euler 2D equations for this system, the person's mass can be written in terms of the defined variables. The equation in the Z direction is:

$$ma_z = N_L + N_R - mg\ \cos\theta \tag{3.16}$$

which can be rearranged as:

$$N_L + N_R = m(a_z + g\ \cos\theta) \tag{3.17}$$

The value of $(a_z + g\ \cos\theta)$ is equivalent to the acceleration measured by the IMU, A_z, so the equation can then be written as:

$$N_R = mA_z - N_L \tag{3.18}$$

A similar process can be carried out in the Y direction. The equation is:

$$ma_y = F_L + F_R - mg\ \sin\theta \tag{3.19}$$

which can be rearranged as:

$$F_L + F_R = m(a_y + g\ \sin\theta) \tag{3.20}$$

The value of $(a_y + g\ \sin\theta)$ is equivalent to the acceleration measured by the IMU, A_y, so the equation can then be written as:

$$F_R = mA_y - F_L \tag{3.21}$$

A third equation can be written for the sum of moments in the X direction about the

CoM:

$$I_{xx}\alpha_x - (I_{zz} - I_{yy})w_z w_y = N_L x_L - N_R x_R - F_L h - F_R h + M_L + M_R \tag{3.22}$$

In this case α_x is equivalent to Λ_x and w_z and w_y are equivalent to Ω_z and Ω_y from the IMU. Since at this point both the inertia terms and mass are unknown, it is necessary to make an assumption that the inertia values are functions of the mass so that there is only one unknown variable:

$$\begin{aligned} I_{yy} = I_{xx} &= md \\ I_{zz} &= mb \end{aligned} \tag{3.23}$$

Using mass properties from previous postural stability research [44] where the mass was set to 78 kg and the inertias were set to 47.2 kg·m^2 and 1.0 kg·m^2. This results in values of d=0.2736 m^2 and b=0.013 m^2.

Substituting Equations 3.18, 3.21, and 3.23, into 3.22 results in:

$$m[d\Lambda_x - (b-d)\Omega_z\Omega_y] = N_L x_L - (mA_z - N_L)x_R - F_L h - (mA_y - F_L)h + M_L + M_R \tag{3.24}$$

and when the right side is expanded the result is:

$$m[d\Lambda_x - (b-d)\Omega_z\Omega_y] = N_L x_L - mA_z x_R + N_L x_R - \cancel{F_L h} - mA_y h + \cancel{F_L h} + M_L + M_R \tag{3.25}$$

The terms containing F_L cancel out and the terms containing m can be collected on the left side of the equation to obtain:

$$m[d\Lambda_x - (b-d)\Omega_z\Omega_y + A_z x_R + A_y h] = N_L x_L + N_L x_R + \cancel{M_L} + \cancel{M_R} \tag{3.26}$$

Finally, the reaction moments about each foot can be neglected since their contributions are small. The equation can then be solved for m to obtain:

$$m = \frac{N_L(x_L + x_R)}{d\Lambda_x - (b-d)\Omega_z\Omega_y + A_z x_R + A_y h} \tag{3.27}$$

To summarize, the simplifying assumptions in this method include: neglecting ship pitch and yaw angles, neglecting relative accelerations between the ship and the subject's CoM, neglecting the reaction moments at each foot, neglecting the difference between the CoM calculated with the motion capture data and the actual CoM location, and that the inertia properties of the person can be represented as linear functions of their mass.

For a given ship motion profile this equation can be used to calculate the person's mass as function of time (as shown in Figure 3.20), and then averaged to obtain a reasonable overall mass estimate. The estimate can be further improved by averaging the value over more than one data recording.

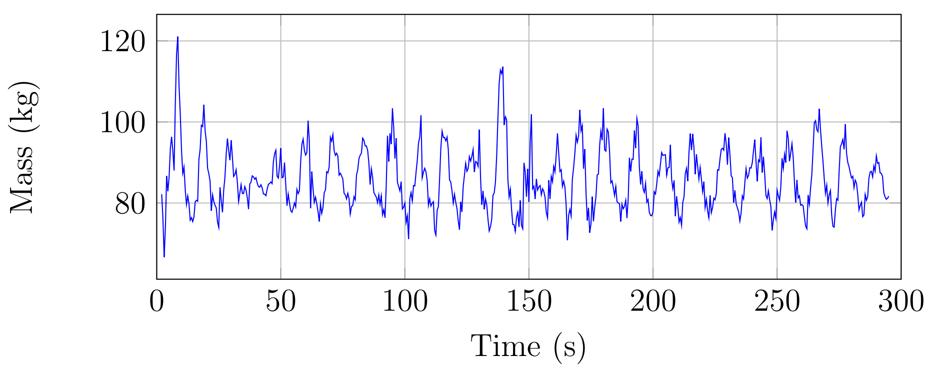

Figure 3.20: Mass calculation over five minute data recording. Value fluctuates due to simplifying assumptions.

This procedure can be generalized to fully-spatial conditions in order to accommodate the full ship motions that would be experienced by a subject standing at any orientation with respect to the ship centreline. A free-body diagram for the full spatial case is shown in Figure 3.21. In this figure **f** and **m** are the reaction forces and moments at the person's feet, $\mathbf{a}_{CoM}$ is the acceleration of the person's CoM, and $\mathbf{r}_L$ and $\mathbf{r}_R$ are vectors from the person's CoM to their feet.

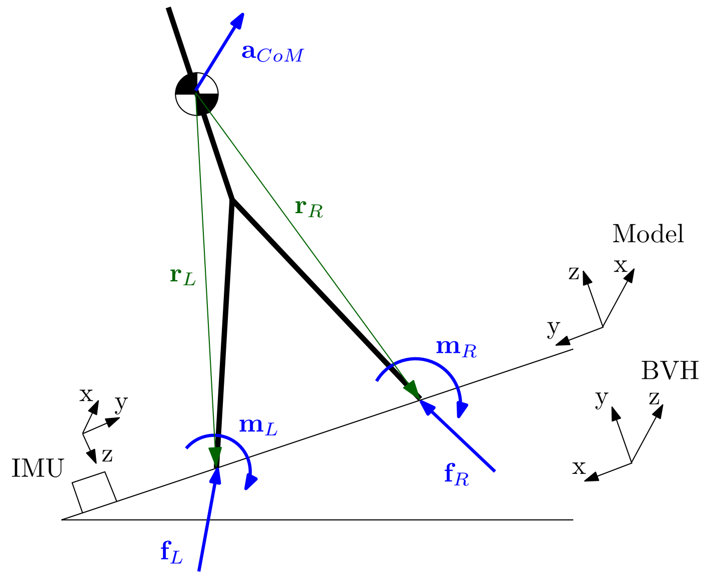

Figure 3.21: Spatial model of person standing on moving ship deck.

The translational and angular equations of motion for this system can be written as:

$$\mathbf{f}_L + \mathbf{f}_R = m\mathbf{a}_{CoM} \tag{3.28}$$

and

$$\mathbf{I}\dot{\boldsymbol{\omega}} + \boldsymbol{\omega} \times \mathbf{I}\boldsymbol{\omega} = \mathbf{r}_L \times \mathbf{f}_L + \mathbf{r}_R \times \mathbf{f}_R + \mathbf{m}_L + \mathbf{m}_R \tag{3.29}$$

where:

$$\begin{aligned} \mathbf{a}_{CoM} &= \mathbf{a}_{SHIP/INERTIAL} + \mathbf{a}_{CoM/SHIP} \\ \dot{\boldsymbol{\omega}} &= \dot{\boldsymbol{\omega}}_{SHIP/INERTIAL} + \dot{\boldsymbol{\omega}}_{CoM/SHIP} \\ \boldsymbol{\omega} &= \boldsymbol{\omega}_{SHIP/INERTIAL} + \boldsymbol{\omega}_{CoM/SHIP} \end{aligned} \tag{3.30}$$

The SHIP/INERTIAL terms are all measured by the inertial sensor, and acceleration due to gravity is included in $\mathbf{a}$. The CoM/SHIP terms can be calculated from the motion capture data, by numerically differentiating Equation 3.13 with respect to time. Equation 3.28 can be substituted into Equation 3.29 to obtain:

$$\mathbf{I}\dot{\boldsymbol{\omega}} + \boldsymbol{\omega} \times \mathbf{I}\boldsymbol{\omega} = \mathbf{r}_L \times \mathbf{f}_L + \mathbf{r}_R \times m\mathbf{a}_{CoM} - \mathbf{r}_R \times \mathbf{f}_L + \mathbf{m}_L + \mathbf{m}_R \tag{3.31}$$

Finally, if it is assumed that the inertia matrix is a linear function of mass as it was before, $\mathbf{I} = m\mathbf{I}'$, where $\mathbf{I}'$ is a 3×3 diagonal matrix with entries d, d, and b, and that the contribution from the reaction moments $\mathbf{m}_L$ and $\mathbf{m}_R$ are negligible, then Equation 3.31 can be written as:

$$m(\mathbf{I}'\dot{\boldsymbol{\omega}} + \boldsymbol{\omega} \times \mathbf{I}'\boldsymbol{\omega} - \mathbf{r}_R \times \mathbf{a}_{CoM}) = (\mathbf{r}_L - \mathbf{r}_R) \times \mathbf{f}_L \tag{3.32}$$

When individual vector components are considered, this provides three equations that can be used to solve for subject mass (with the separate solutions specified here as m_x, m_y, and m_z). In theory they should all predict the same value while in practice they do not. Sample results for a subject standing at 0°, 45°, and 90° with respect to ship centreline are shown in Figures 3.22 through 3.24, respectively.

It can be observed in the figures that for a subject standing at 0°, only m_y gives a reasonable result, for 45°, the m_x and m_y give reasonable results, and for 90°, only m_x gives a reasonable result. The mostly likely reason for this is that these directions are the ones that correspond to the lateral axis of the person in the person's frame, similar to the 2D analysis that was performed previously. In the non-lateral directions the magnitude of $\mathbf{r}_L - \mathbf{r}_R$ is very small, such that the model effectively collapses from a three-bar linkage to an inverted pendulum, so that any noise or other errors from the simplifying assumptions dominate the result. The erroneous results were accommodated by not including them in the total mass average of each subject. It should be noted that some of the erroneous data

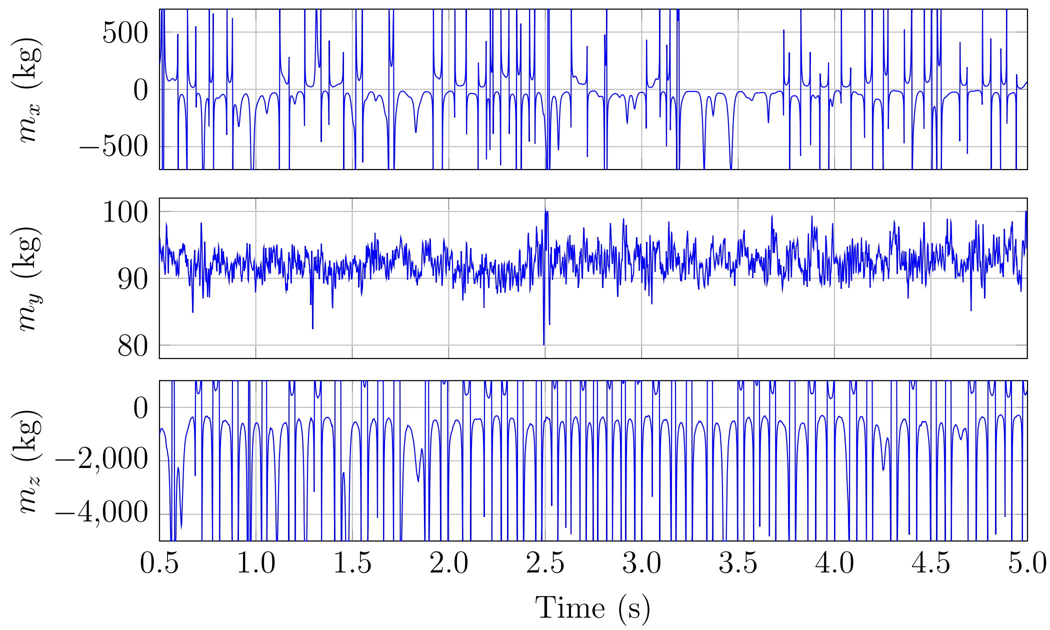

Figure 3.22: Mass estimation calculations with subject standing at 0°.

are many orders of magnitude larger than their mean values. Therefore the graphs have been clipped in order to display meaningful results.

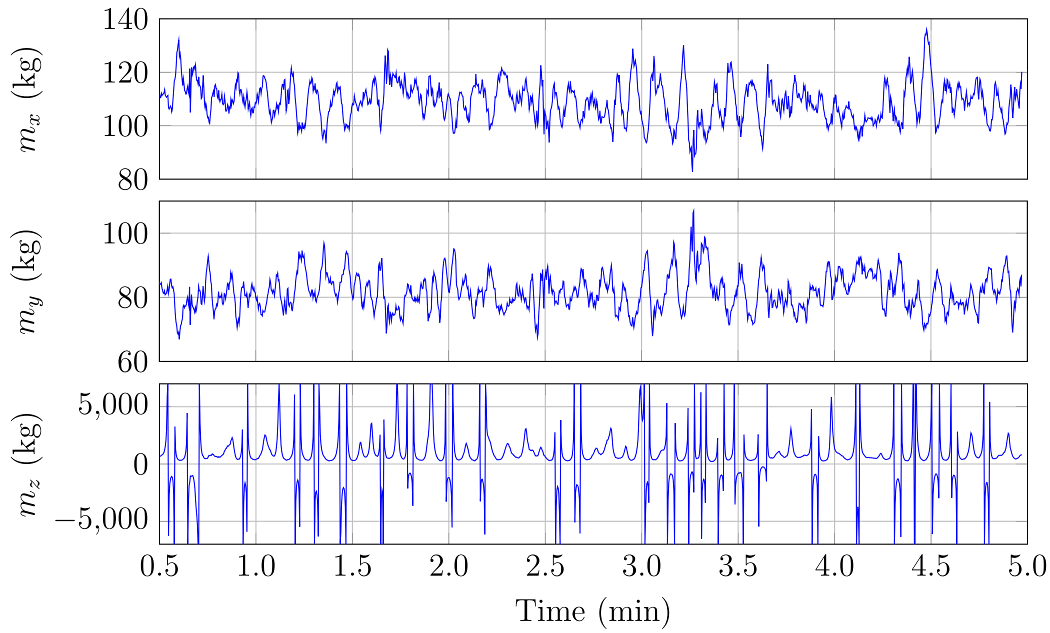

Figure 3.23: Mass estimation calculations with subject standing at 45°.

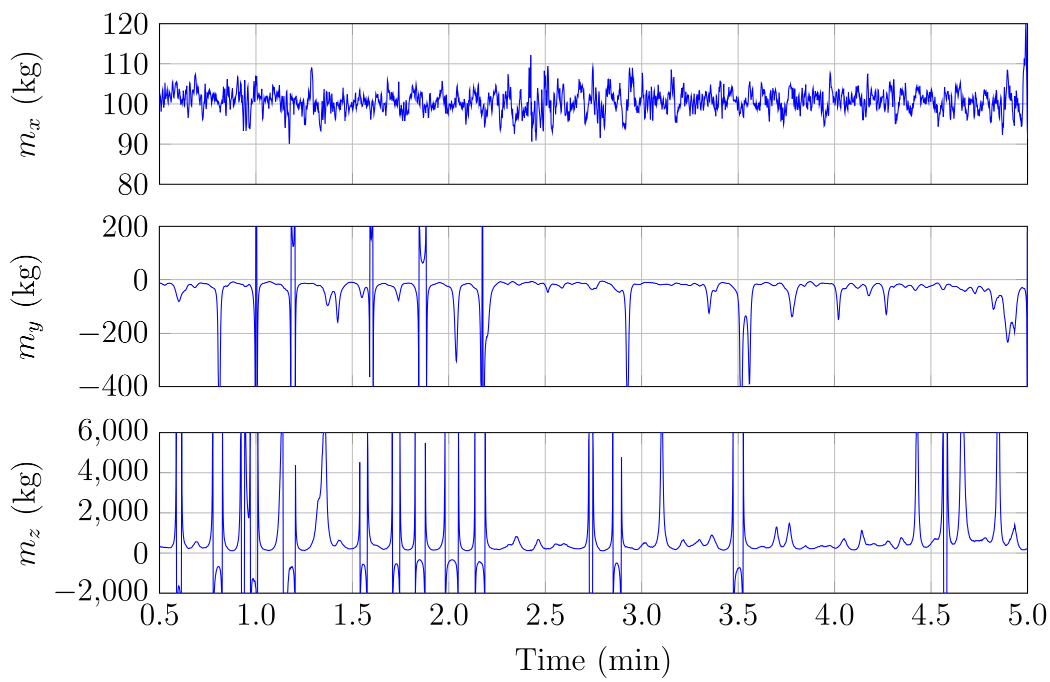

Figure 3.24: Mass estimation calculations with subject standing at 90°.

3.4.3 Insole Calibration

Once a subject's mass had been calculated, Equation 3.28 can be rearranged to solve for the expected reaction force under the subject's right foot:

$$\mathbf{f}_R = m\mathbf{a}_{CoM} - \mathbf{f}_L \tag{3.33}$$

If the measurements made by the load cell are substituted into $\mathbf{f}_L$, the accelerations calculated in Equation 3.30 are substituted into $\mathbf{a}_{CoM}$, and the mass estimated in the previous section is substituted for m, then $\mathbf{f}_R$ should give an estimate of the reaction forces under the subject's right foot. The accuracy of this result is limited to how well the analysis discussed in the previous section matches reality, and the compounding of the experimental errors from the motion capture data and IMU data. Therefore, rather than using the measured left foot and estimated right foot load cell data for further calculations, they were instead used to calibrate the insole data which is not dependent on the IMU or motion capture data for its accuracy.

Best-fit linear correlation coefficients were calculated between the load cell data and insole data for each experimental trial. Sample results for the left foot insole data before and after calibration are shown in Figures 3.25 and 3.26. Sample results for the right foot insole data before and after calibration are shown in Figures 3.27 and 3.28.

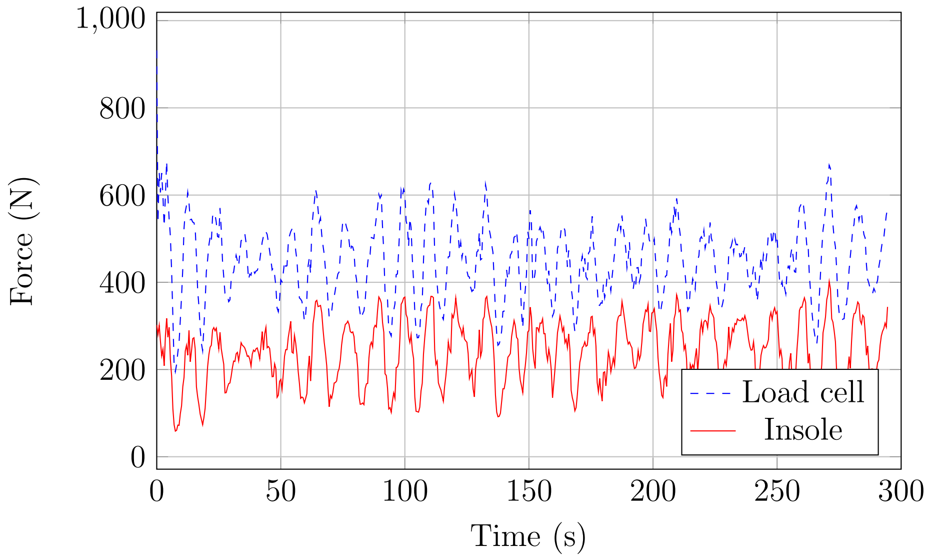

Figure 3.25: Recorded left foot data for the load cell and insole.

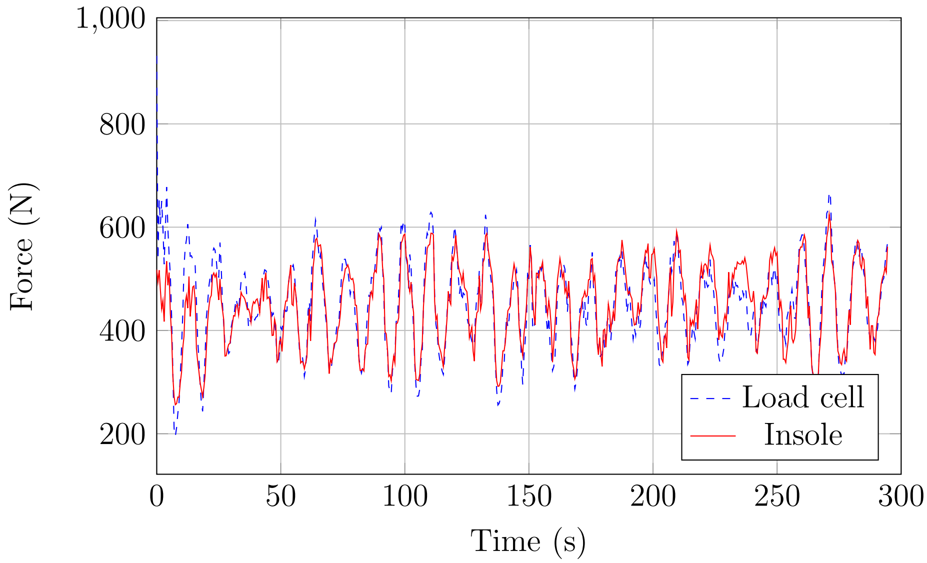

Figure 3.26: Recorded left foot load cell data and calibrated left foot insole data.

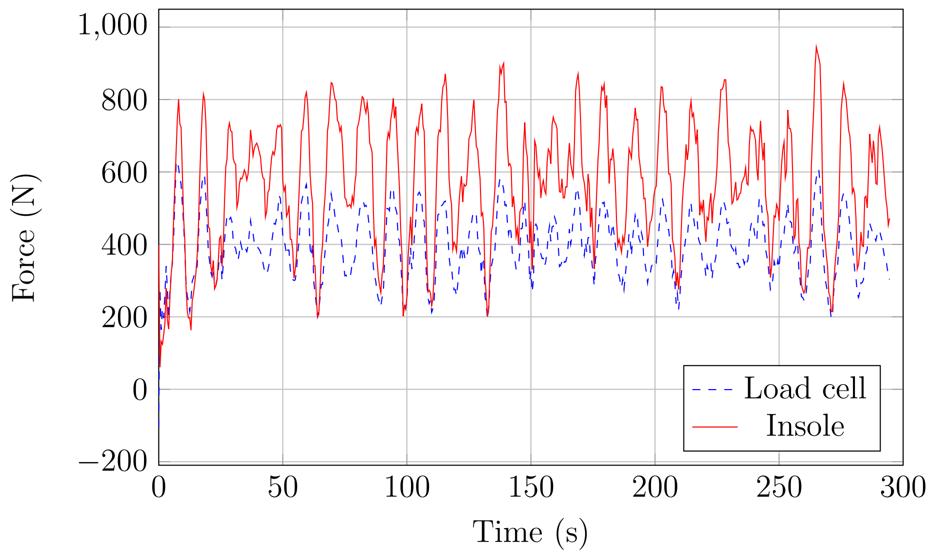

Figure 3.27: Estimated right foot data from load cell and model, and recorded right foot insole data.

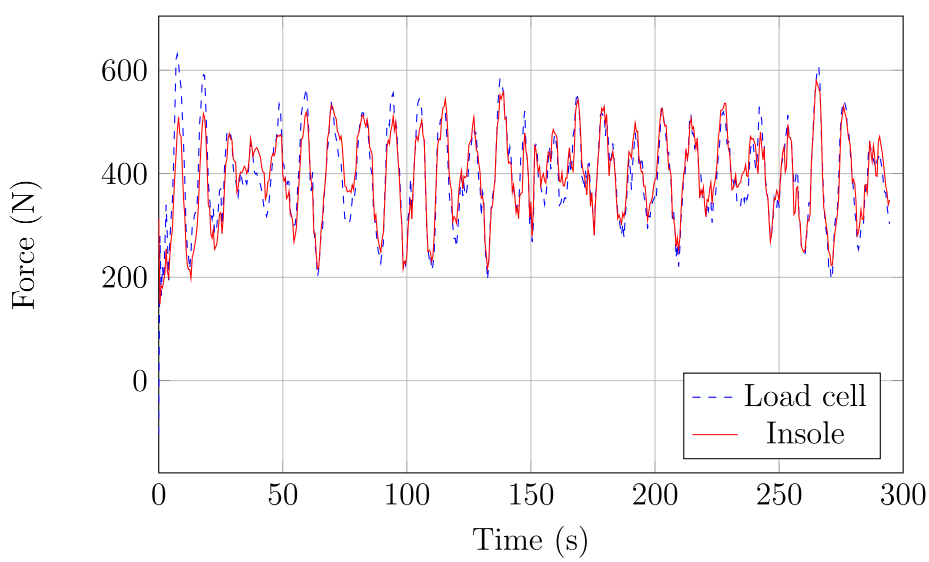

Figure 3.28: Estimated right foot data from load cell and model, and calibrated right foot insole data.

3.4.4 Insole Outlines

The FScan insole data has an advantage over the load cell data as it can provide information on the pressure distribution over each footprint. When combined with information on the positioning of the ankles and feet relative to the rest of the body, an estimation of a person's base of support (BoS) can be obtained.

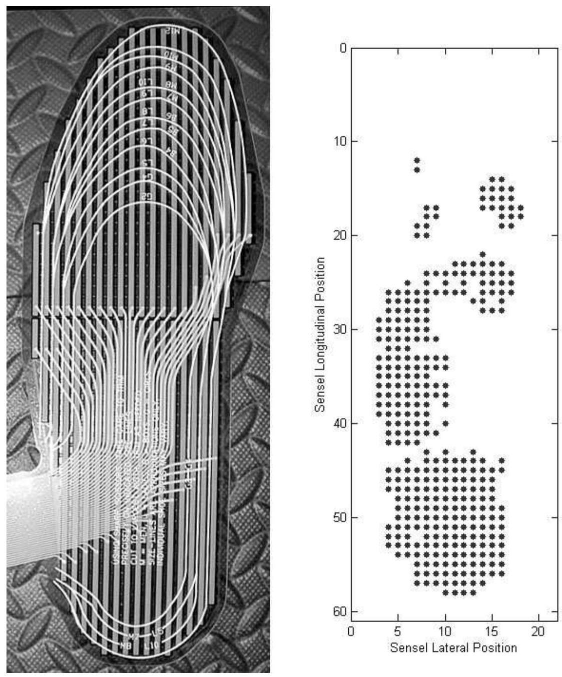

Figure 3.29: Uncut insole and sample measurement.

Insole pressure measurements are made by a grid of pressure-sensitive sensels, which are pockets of ink that have an electrical resistance proportional to the compressive force applied to them. Each insole contains up to 60 sensels along the longitudinal foot axis, and 21 sensels along the lateral axis. Each sensel measures force within an area of approximately 5 mm by 5 mm. Since insoles are cut in advance in order to fit into a person's footwear, they may or may not make measurements up to the limits. Figure 3.29 shows a photograph of an uncut insole and a sample measurement made by it after it had been trimmed and placed into a person's shoes. By summing the measurements made by all of the sensels, the total vertical force acting under the person's feet can be calculated.

In order to calculate a subject's BoS, the insole measurements were used to calculate the outer edges of each subject's footprint.

The first step was to perform a binary OR calculation between all of the measurements for each insole for all of a subject's experimental trials. In other words, for each subject, it was determined which sensels were activated at any time during their experimental trials. This resulted in an insole 'mask' for each subject for each foot.

In order to fill in the holes and gaps in the mask that occur due to how the subject's feet contact their shoes, or because of malfunctioning sensels, it was necessary to calculate the equivalent convex hull of the mask/footprint [54]. The implemented algorithm uses three passes to determine which sensels that did not register a pressure reading are contained within the foot's outline. A sample of the results before and after this calculation are shown in Figure 3.30.

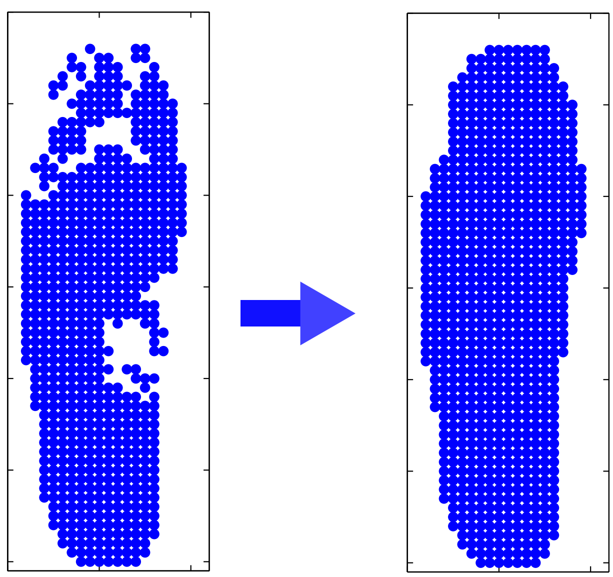

Figure 3.30: Insole mask/footprint before and after the convex hull calculation.

Next, the resulting plot for each participant was manually analyzed in order to determine the minimum and maximum sensel limits that should be used for the insole outline calculations. It was necessary to perform this step manually, rather than with computer code because of cases where there were outlier data points caused by malfunctioning sensels.

Using the insole masks and the limit values, an outline of each insole was calculated. The results of an insole outline calculation are shown in Figure 3.31. The inside edge of the insole outline is not calculated because the insole outlines for each foot are combined into a total-body base of support outline.

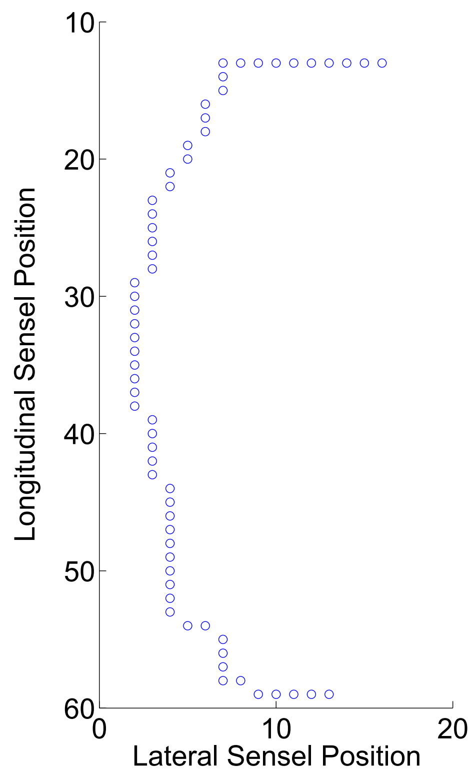

Figure 3.31: Sample calculated insole outline.

3.4.5 Ankle Locations

In order to match the insole measurements with the BVH joint positions, it was necessary to estimate the ankle locations within the insoles. Based on the BVH motion capture files, it was estimated that the ankle location was located approximately just in front of the heel of the foot. A sample screenshot showing where iPi studio places the ankle joint is shown in Figure 3.32.

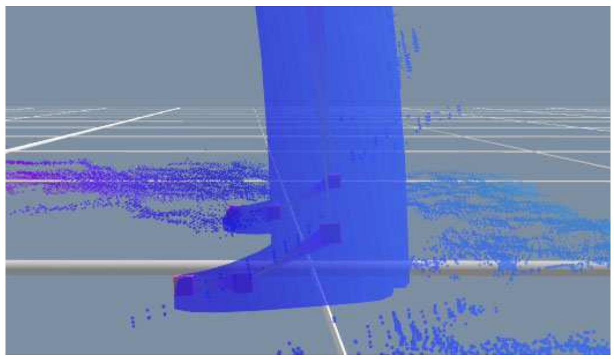

Figure 3.32: Screenshot of iPi Studio showing skeleton ankle position with respect to leg/foot outline.

In the insole data, these locations were determined manually from a series of contour plots where all of the insole pressure measurements were summed together at each x-y position. Sample contour plots with the ankle location indicated on them are shown in Figure 3.33.

3.4.6 Insole Force Centre

The insole pressure data can be summed together to calculate the total vertical force acting on each foot and averaged together by row and by column to obtain the location within the footprint where that force acts. One issue with this calculation is that some of the insole recordings had a few sensels that did not work properly and as a result always read very large erroneous values. In order to compensate for this, a smoothing technique was

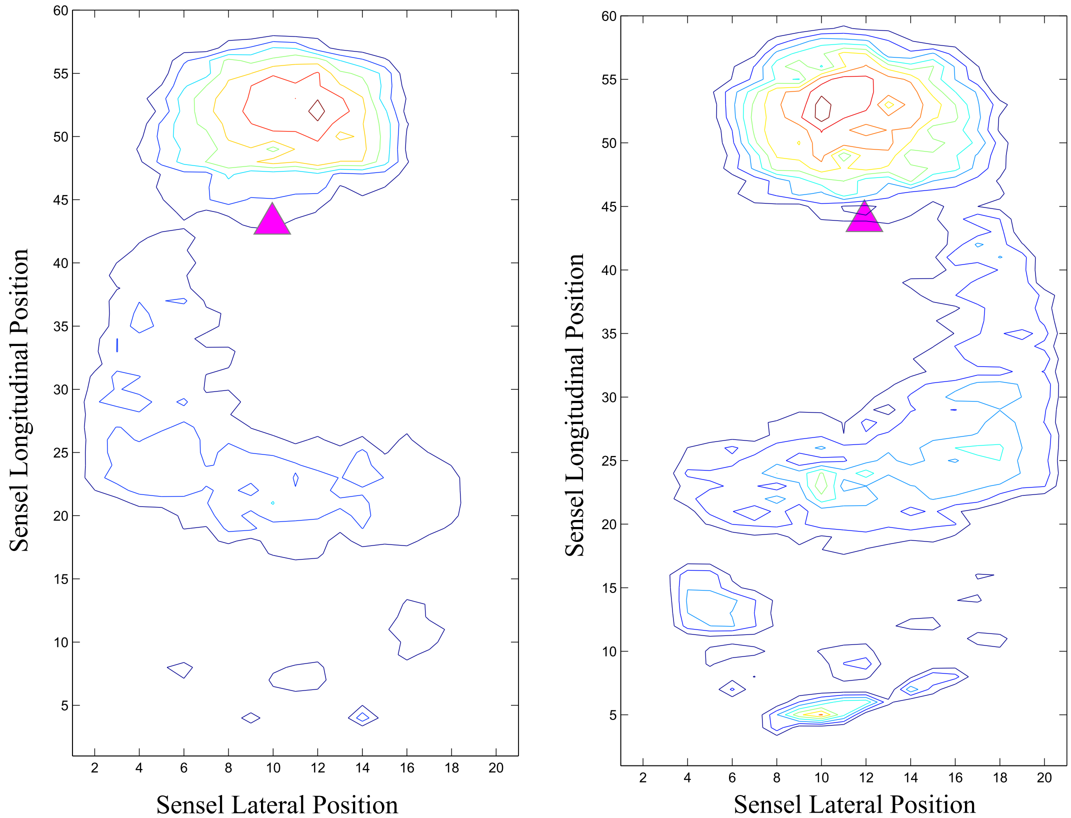

Figure 3.33: Contour graphs showing the sum of all pressure measurements.

applied to the insole data. The implemented algorithm took the largest pressure reading at each longitudinal sensel position and replaced it with the average of the values measured by the four sensels surrounding it (or three for edges). This process was then repeated in the lateral direction. It was confirmed that this amount of smoothing was sufficient when analyzing the contour plots for each subject shown in Figure 3.33. Any sensels that were consistently measuring very large values compared to the sensels surrounding it would appear as a peak in those plots.

3.5 Base of Support Analysis

Once all of the required force and positional data had been filtered and calibrated, the final step was to combine all of the data together. The first step was to combine the BVH joint data with the insole data in order to place the insole measurements in the correct positions with respect to the body. The following actions were performed on both the insole outline data points and insole force centre points.

- The origin of each insole's coordinate system was translated from above the top left side of the foot (as plotted in the figures in the previous sections) to the ankle, and arranged so that the positive vertical axis pointed in the direction of the toe.
- Insole coordinates were rotated from the insole coordinate frame to the ship-fixed coordinate frame so that the vector from the ankle to the toe was pointing in the same direction as the subject.
- Insole coordinates were translated to the positions of the left and right ankles from the BVH data in order to determine the coordinates of each data point in the ship frame.
- Additional data points were generated to form connecting lines between the top and bottom of the left and right insole outlines, equally spaced regardless of subject orientation.
- The overall centre of force location was calculated by averaging the individual foot centres according to their locations and magnitudes.

The CoM location was added to the data set and all points were plotted on the same axes. A sample of the final result is shown in Figure 3.34. Similar graphs were calculated at each timestamp for every experimental trial.

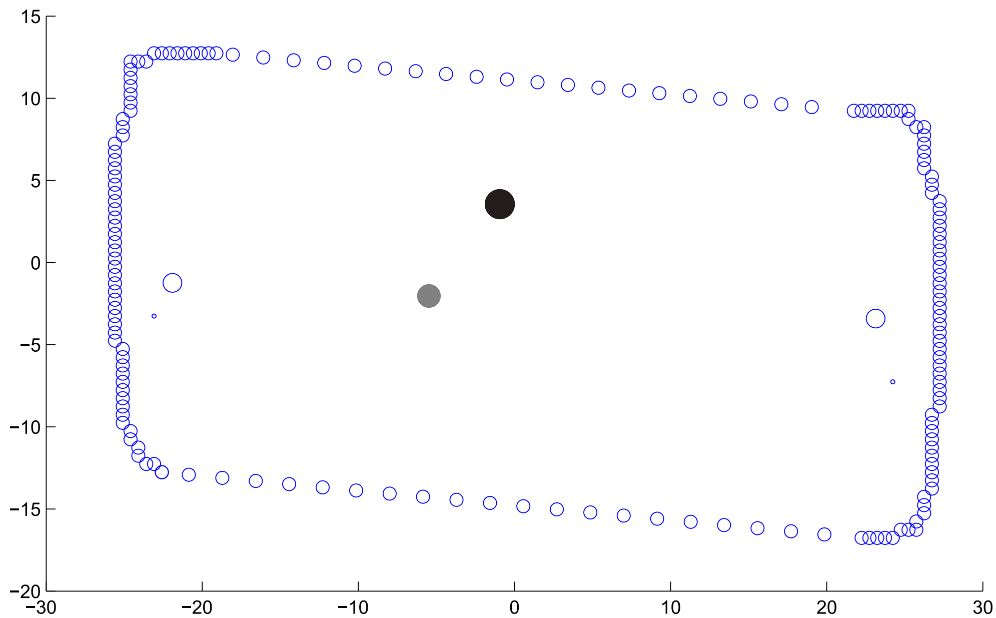

Figure 3.34: Base of support outline with ankle locations (small side circles), individual foot CoF locations (large side circles), body CoM (black and larger filled circle), and overall CoF (gray and smaller filled circle).

3.5.1 Base of Support Time-lapse

From the BoS diagrams generated in the previous section, two results were produced. The first was a series of animations that allow one to monitor in real time the relative motion between the CoM and CoF. The second was a series of graphs which display all of the data points simultaneously. These graphs are useful in that they provide insight into the range of motion that each point of interest experienced. Sample graphs with a subject standing at 45°, 0°, and 90° with respect to ship centreline are shown in Figures 3.35 through 3.37, respectively. In order to reduce clutter in the graphs, only the average of all of the BoS outline data points are shown.

These three BoS graphs are from sequential experimental sessions and are presented in that order. As defined on the graph axes, the positive X axis points towards the front (bow) of the ship and the positive Y axis points towards the left (port) side of the ship.

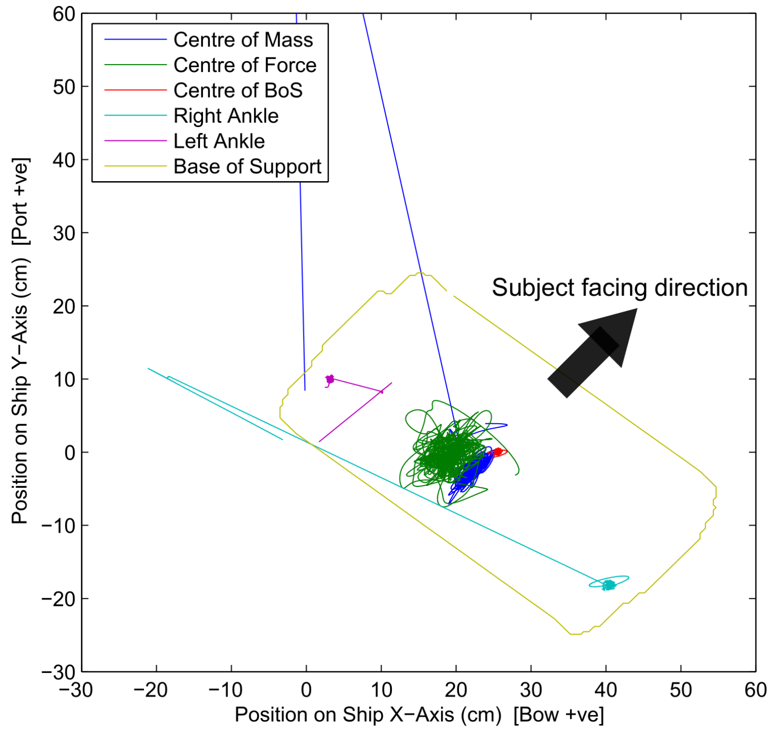

Figure 3.35: Motion of BoS-related parameters for subject standing at 45° with respect to ship centreline.

It can be observed in Figure 3.36 that both the CoM and CoF are offset from the centre of the subject's stance. This can be attributed to two factors. One is that the mean roll angle of the ship was offset from zero, which is supported by the IMU data. The ship tended to roll more to port than it did to starboard. It is also possible that the subject simply had an offset in their stance. Figure 3.37 supports both of these factors since it can be observed that the vertical projection of the CoM is at the back of their stance, which indicates that the subject is leaning backwards when viewed in the ship frame. The CoM is also offset from the centre of their stance, supporting the theory that they are leaning slighty to one side in their stance.

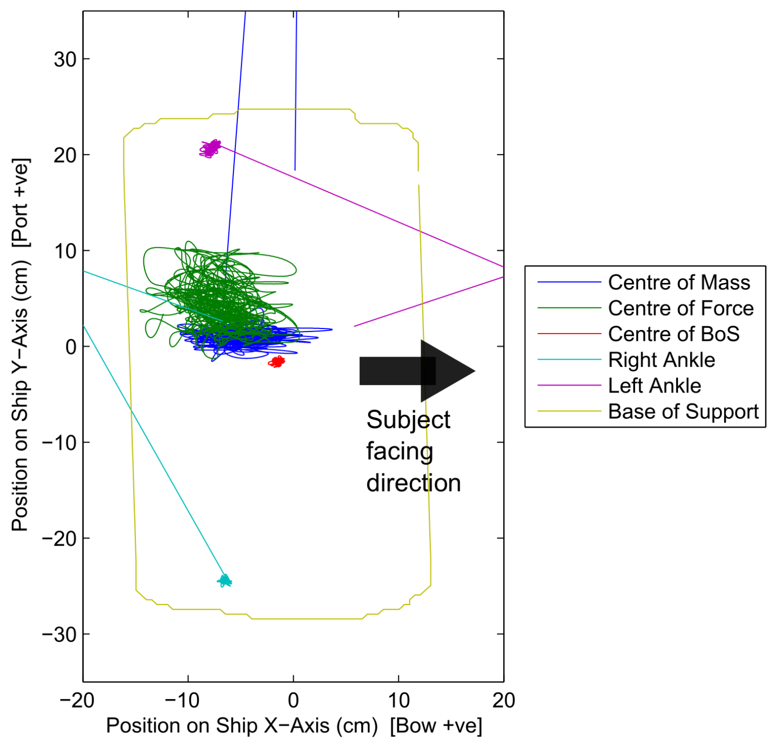

Figure 3.36: Motion of BoS-related parameters for subject standing at 0° with respect to ship centreline.

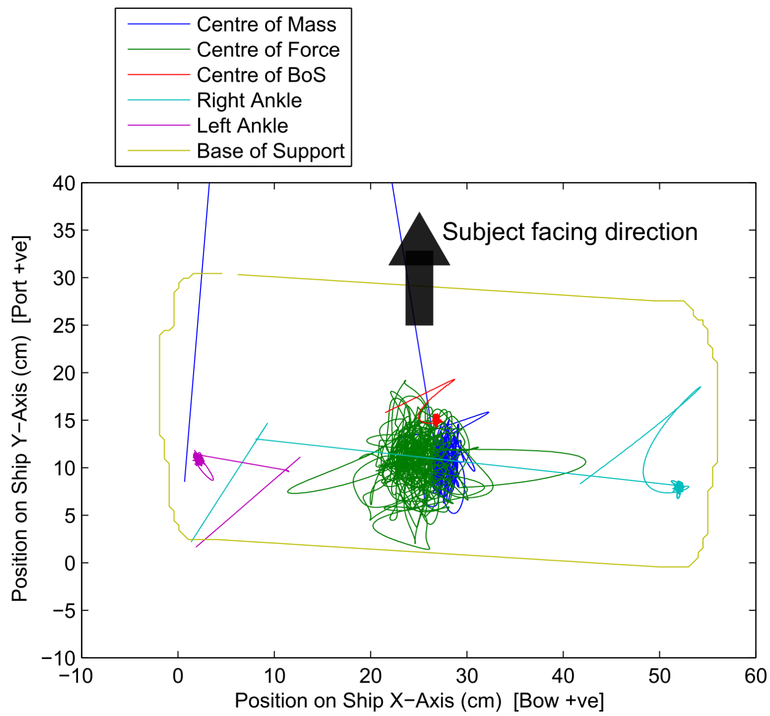

Figure 3.37: Motion of BoS-related parameters for subject standing at 90° with respect to ship centreline.

3.6 MIIs and CoM Kinematics

As discussed earlier in this chapter, previous research implies that there is a relationship between CoM position and velocity whereby even if the CoM is contained within the BoS, if it has sufficient velocity, foot motion will still be required to maintain stability. As discussed in the previous chapter, overall the participants of the sea trial did not experience an abundance of MIIs. However, the ones that did occur were compiled so that the position/velocity combinations could be studied. MIIs were identified both by analyzing the foot position data and by manually verifying in each recording whether the stepping events were actually MII occurrences rather than MII recoveries or simply stance repositioning events. For each subject, only the cases where they were standing at 90° with respect to ship centreline were used since that was the orientation at which participants experienced the most MIIs. For each subject that experienced MIIs, graphs were produced that plotted the values of CoM position and velocity at the times of occurrence of each of the identified MIIs. These results are shown in Figures 3.38 through 3.40. The position is defined as the absolute distance measured from the BoS centre, and the velocity is the rate of change of that magnitude.

For none of the participants is there a clear relationship between CoM position and velocity. MIIs tend to occur at a large variety of position/velocity combinations. This result is not unexpected as the participants were exposed to six-DOF motion that was beyond the capabilities of most motion platforms, which is where the experiments referenced in the literature took place.

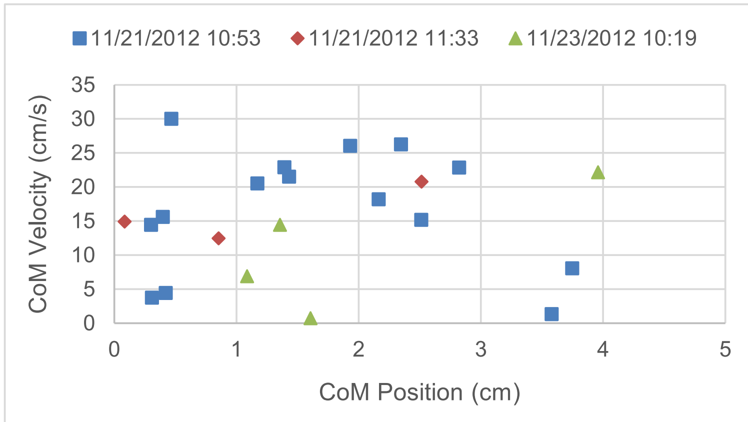

Figure 3.38: CoM position and velocity combinations at MII occurrences for a sea trial participant on November 21, 2012 and November 23, 2012.

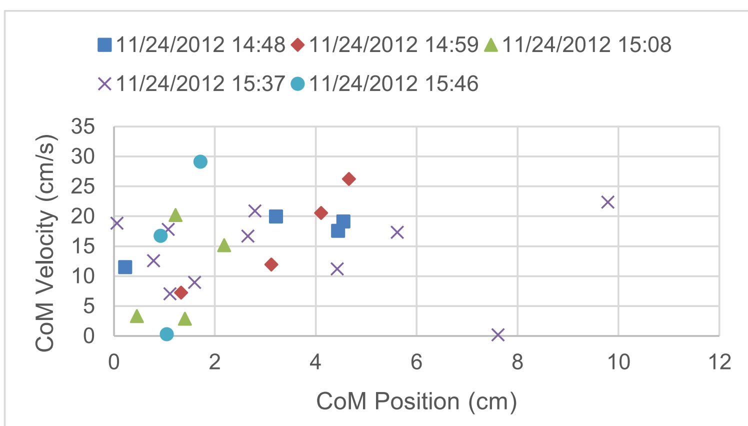

Figure 3.39: CoM position and velocity combinations at MII occurrences for a sea trial participant on November 24, 2012.

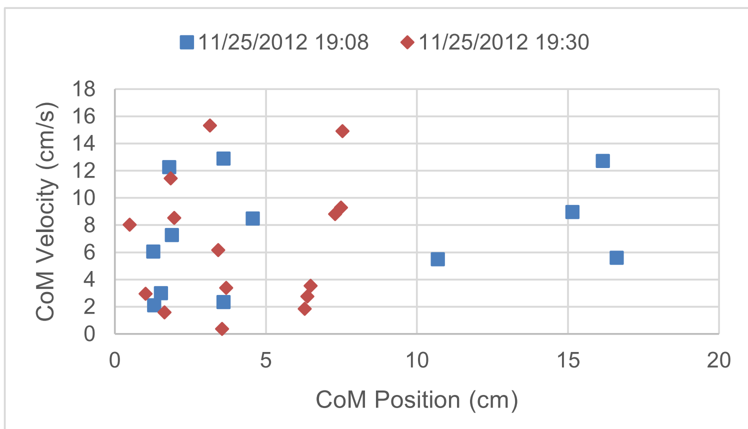

Figure 3.40: CoM position and velocity combinations at MII occurrences for a sea trial participant on November 25, 2012.

3.7 Data Processing Summary

This chapter has presented all of the data processing steps that were required to transform the sea trial data to a useful form for interpretation of the results and application to human postural stability modelling. These procedures were carried out for each of the 13 experiment participants, and the results for the latter 8 of them will be analyzed more closely in subsequent chapters. A summary of the data that were processed in the chapter is provided below.

- Ship kinematics data, with and without the components of acceleration due to gravity.
- Human body kinematics data for 22 joints.
- Human body CoM kinematics.
- Load cell data for the left foot, and estimated data for the right foot.
- Vertical force data measured by the insoles and scaled using the simplified human-ship model.
- The mass of each subject.
- An estimation of the BoS of each subject using the outline of their foot prints.
- The magnitude and position of the CoF within each person's BoS.
- The human-ship reaction moment that the centre of force generates about the CoM in order to maintain upright stance.
- Time history data of the motion of the CoM and CoF within the BoS for each experimental trial.

- Time stamps for MII occurrences for subjects that experienced them while standing at 90° with respect to the ship centreline, and the values of all of the above parameters at those times.

The data from each source was low-pass filtered using the techniques detailed in this chapter, and transformed from each independent coordinate system to the standard modelling coordinate conventions of this thesis, which is X positive forward, Y positive left, and Z positive up.

Chapter 4

Derivation and Validation of a Spatial Human Postural Stability Model

4.1 Motivation

In naval engineering and related disciplines, one field of study involves using dynamic models of the human body in conjunction with quantitative records of body centre of mass kinematics and ship motions to model human balance behaviour. Research in this area can lead to improvements in ship operations and designs that improve crew safety and efficiency.

This chapter will present the development of a new spatial human postural stability model for use in prediction of human postural response to ship motion. The derivation of this model is novel for two primary reasons. The first is that the six-degree-of-freedom equations of motion are derived in an automated way, which means that additional bodies can easily be added or removed, without greatly increasing the complexity of the formulation. The second reason is that the equations can be expressed in matrix form as opposed to the tensor notation which is typically required for dynamics formulations derived in an automated way. Additionally, the way that the model is coded allows individual components to be easily identified and modified as required. The derived model is then validated by comparing it to existing simpler models derived using other methods but exposed to equivalent input conditions.

The human will be modelled as a four-link inverted pendulum. Therefore, the most general case of the model should have six degrees of freedom for the ship motion, and three for each of the inverted pendulum links.

4.2 Notation Conventions

This section will present the mathematical notation conventions that are used to derive the equations of motion in subsequent sections.

A scalar value is written in lowercase normal italics in the form of z_b^a, where a indicates which body the value corresponds to and b indicates which degree of freedom, if applicable. For example, the mass of body k would be written as m^k. A vector value is written in lowercase bold in the form of ${}^a\mathbf{z}^b$ where a indicates which frame the vector is defined in and b indicates which body the vector corresponds to. For example, ${}^0\mathbf{w}^3$ would be the angular velocity vector of body 3, defined in frame 0. Matrix values are written in uppercase bold and the surrounding subscripts and superscripts vary according to the nature of the matrix. Two special matrices are $\mathbf{I}$, a 3×3 identity matrix, and $\mathbf{O}$, a 3×3 zero matrix.

In order to reduce the number of transpose symbols required, any multiplication operation which includes a vector and a matrix implicitly indicates whether the vector is a row vector or a column vector. This means that writing $\mathbf{Ab}$ would indicate that $\mathbf{A}$ is a matrix and $\mathbf{b}$ is a column vector with length equal to the number of columns in $\mathbf{A}$ and that writing $\mathbf{bA}$ indicates that $\mathbf{b}$ is a row vector with length equal to the number of rows in $\mathbf{A}$.

The rotation convention used is XYZ body-fixed Euler angles, also referred to as Bryant angles. This rotation convention is commonly used in ship-based simulations because the numerical singularity that can be an issue with Euler angles would occur at $\pm 90°$ pitch, an unlikely orientation for a ship to encounter.

In order to define the rotation mathematically, consider the rotation from coordinate frame J to frame K, the three Bryant angles θ_1, θ_2, and θ_3, and two intermediate coordinate frames, J' and J''. The rotation is performed by first rotating θ_1 about the X axis in frame J to obtain J'. Next, one rotates θ_2 about the Y axis in J' to obtain J''. Finally, one rotates θ_3 about the Z axis in J'' to obtain K.

The individual transformations in matrix form are defined as:

$$\mathbf{R}_x = \begin{bmatrix} 1 & 0 & 0 \\ 0 & \cos(\theta_1) & -\sin(\theta_1) \\ 0 & \sin(\theta_1) & \cos(\theta_1) \end{bmatrix} \tag{4.1}$$

$$\mathbf{R}_y = \begin{bmatrix} \cos(\theta_2) & 0 & \sin(\theta_2) \\ 0 & 1 & 0 \\ -\sin(\theta_2) & 0 & \cos(\theta_2) \end{bmatrix} \tag{4.2}$$

$$\mathbf{R}_z = \begin{bmatrix} \cos(\theta_3) & -\sin(\theta_3) & 0 \\ \sin(\theta_3) & \cos(\theta_3) & 0 \\ 0 & 0 & 1 \end{bmatrix} \tag{4.3}$$

and compiled together as:

$$\mathbf{R}^{JK} = \mathbf{R}_x \mathbf{R}_y \mathbf{R}_z \tag{4.4}$$

The transformation matrix $\mathbf{R}^{JK}$ is read as the transformation from frame J to frame K where the multiplication operation is performed as:

$$ {}^{k}\mathbf{r}^{n} = {}^{j}\mathbf{r}^{n}\ \mathbf{R}^{JK} \tag{4.5}$$

The reverse transformation is obtained with the transpose or inverse operation since for homogeneous rotational transformations the inverse and transpose are the same:

$$\mathbf{R}^{KJ} = (\mathbf{R}^{JK})^{-1} = (\mathbf{R}^{JK})^{T} \tag{4.6}$$

Coordinate rotations are calculated between subsequent body coordinate systems and are then multiplied together to obtain the overall rotation matrix from individual body frames to the inertial frame. For example, the rotation matrix from a system's fourth coordinate system to the inertial frame (assuming all frames are linked together in order) would be calculated as:

$$\mathbf{R}^{40} = \mathbf{R}^{43}\mathbf{R}^{32}\mathbf{R}^{21}\mathbf{R}^{10} \tag{4.7}$$

The skew-symmetric matrix of a vector ${}^{a}\mathbf{q}^{b}$ is defined as:

$$ {}^{a}\mathbf{S}_{q}^{b} = \begin{bmatrix} 0 & -q_z^b & q_y^b \\ q_z^b & 0 & -q_x^b \\ -q_y^b & q_x^b & 0 \end{bmatrix} \tag{4.8}$$

Writing a vector quantity as a skew matrix is most commonly used when one wishes to write a vector cross product as a matrix multiplication. For example:

$$\mathbf{u} \times \mathbf{v} = \mathbf{u}\ \mathbf{S}_{v} \tag{4.9}$$

4.3 System Configuration

The coordinate systems and degrees of freedom defined in the model are shown in Figure 4.1. There are 18 degrees of freedom (DOF) divided among the 5 bodies, which are modelled using generalized coordinate derivatives labelled as $\dot{x}_i^k$, where k indicates body number, and i is a sequential coordinate index for each body. The selected generalized coordinate derivatives are all body-fixed relative angular velocity components, except for $\dot{x}_4^1$, $\dot{x}_5^1$, and $\dot{x}_6^1$ that are used to define the ship translational DOF. These three DOF are also written as $\dot{x}_1^{1s}$, $\dot{x}_2^{1s}$, and $\dot{x}_3^{1s}$ so that all vector quantities in the derivation have dimensions of 1×3 or 3×1 (aside from the system state vector). Coordinate system 0 is the origin in inertial space. Coordinate system 1 is the ship body-fixed coordinate system and is located at the inverted pendulum attachment point. The X axis points toward the front of the ship (bow) and the Y axis points toward the left side of the ship (port). Coordinate system 2 is used to define the orientation of the person with respect to the ship centreline. Coordinate systems 3 through 6 are body-fixed coordinate systems for each of the four inverted pendulum links.

In the model, the value of $\dot{x}_1^2$ is always zero as the subject's orientation does not change within a single simulation. Therefore there is no equation corresponding to this DOF.

The first six DOF define the kinematics of the ship's motion. The translational DOF of the ship are defined in the ship frame rather than the inertial frame for reasons that will be discussed subsequently.

The state vector of the system can be defined as:

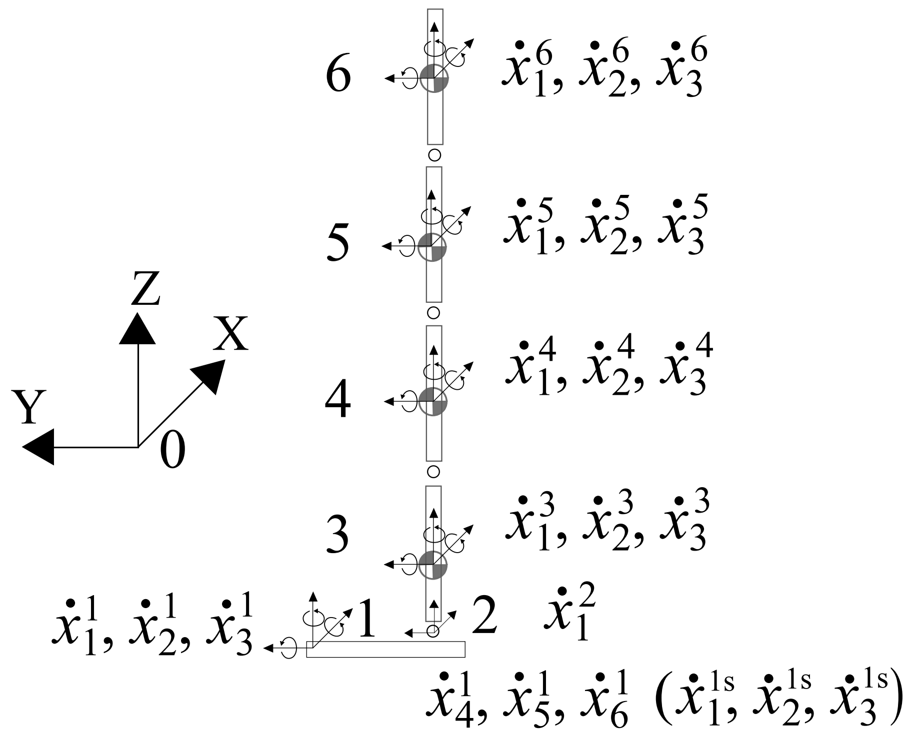

Figure 4.1: Model coordinate systems and generalized coordinate derivatives.

$$\dot{\mathbf{x}} = \begin{bmatrix} {}^1\dot{\mathbf{x}}^1 \\ {}^1\dot{\mathbf{x}}^{1s} \\ {}^3\dot{\mathbf{x}}^3 \\ {}^4\dot{\mathbf{x}}^4 \\ {}^5\dot{\mathbf{x}}^5 \\ {}^6\dot{\mathbf{x}}^6 \end{bmatrix} = \begin{bmatrix} \dot{\mathbf{x}}^1 \\ \dot{\mathbf{x}}^{1s} \\ \dot{\mathbf{x}}^3 \\ \dot{\mathbf{x}}^4 \\ \dot{\mathbf{x}}^5 \\ \dot{\mathbf{x}}^6 \end{bmatrix} \tag{4.10}$$

4.4 Derivation of the Equations of Motion

The derivation of the equations of motion presented here is based on an automated method of deriving the equations of motion for open chain-like mechanisms in a form that lends itself well to matrix mathematics [55]. Some of the notations used in [55] have been modified for this document in order to satisfy standard variable labelling practices. At time of writing, a condensed version of this derivation has been published [56]. The method presented in [55] also does not go into detail on several important aspects, including how to properly extend the procedure to three degrees of freedom per joint, how to incorporate translational degrees of freedom, and how to solve for reaction forces resulting from constrained motion. In order to accommodate these limitations, a second reference was used which documents a similar automated method of deriving the equations of motion, but in tensor notation [57]. While tensor notation lends itself well to the syntax of programming languages, ensuring that the simulation code is correctly implemented can be more difficult. For this reason, the following derivation is performed using matrix notation.

4.4.1 General Equations of Motion

Based on Kane's method and the principle of virtual work [55], Euler's equations of motion of a system can be written as:

$$\sum^{k}\sum^{i}\mathbf{f}^{\,k}\frac{\partial \mathbf{v}^{\,k}}{\partial \dot{x}_i} = \sum^{k}\sum^{i} m^k \dot{\mathbf{v}}_G^k \frac{\partial \mathbf{v}^{\,k}}{\partial \dot{x}_i} \tag{4.11}$$

for translational motion, and:

$$\sum^{k}\sum^{i}\mathbf{m}^k\frac{\partial \mathbf{w}^k}{\partial \dot{x}_i} = \sum^{k}\sum^{i}\left[\mathbf{I}^k\dot{\mathbf{w}}^k + \mathbf{w}^k\times\left(\mathbf{I}^k\mathbf{w}^k\right)\right]\frac{\partial \mathbf{w}^k}{\partial \dot{x}_i} \tag{4.12}$$

for rotational motion of rigid bodies. The index k is cycled over the number of bodies in the system, and the index i is cycled over the total number of generalized coordinate derivatives, $\dot{x}_i$. The terms $\mathbf{w}^k$ and $\mathbf{v}_G^k$ are the angular velocity and velocity of the centre of mass (CoM), respectively. The mass scalar and inertia matrix of each body are represented by m^k and $\mathbf{I}^k$, and $\mathbf{f}^k$ and $\mathbf{m}^k$ are the external forces and moments acting on each body. The following sections will determine the matrix formulation for each of the terms used in these equations.

4.4.2 Translational Equations

The centre of mass (CoM) of body n in inertial coordinates can be defined as:

$$ {}^{0}\mathbf{p}^{n} = \sum_{k=1}^{n-1} {}^{k}\mathbf{q}^{k}\ \mathbf{R}^{k0} + {}^{n}\mathbf{r}^{n}\ \mathbf{R}^{n0} \tag{4.13} $$

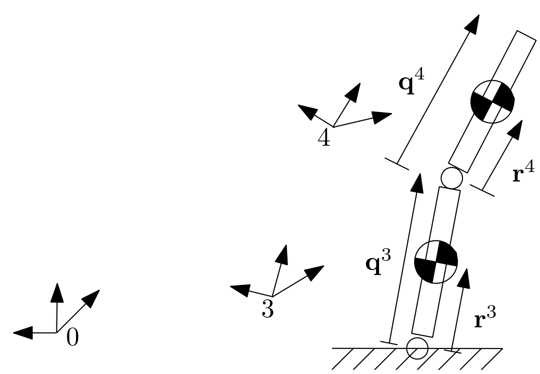

Figure 4.2: Sample inverted pendulum coordinate definitions for partial velocity matrix determination.

where, as shown in Figure 4.2, ${}^{k}\mathbf{q}^{k}$ is a vector in local coordinates which defines the connecting point of the subsequent link and ${}^{n}\mathbf{r}^{n}$ is a vector in local coordinates which defines the location of the link's CoM. The rotation matrices $\mathbf{R}^{k0}$ and $\mathbf{R}^{n0}$ are the transformations from frame k to the inertial frame and from frame n to the inertial frame respectively.

The velocity of the CoM in inertial coordinates can be calculated by differentiating the position with respect to time:

$$ {}^{0}\mathbf{v}^{n} = \frac{\mathrm{d}}{\mathrm{dt}}({}^{0}\mathbf{p}^{n}) = \sum_{k=1}^{n-1} \cancel{{}^{k}\dot{\mathbf{q}}^{k}}\ \mathbf{R}^{k0} + \sum_{k=1}^{n-1} {}^{k}\mathbf{q}^{k}\ \dot{\mathbf{R}}^{k0} + \cancel{{}^{n}\dot{\mathbf{r}}^{n}}\ \mathbf{R}^{n0} + {}^{n}\mathbf{r}^{n}\ \dot{\mathbf{R}}^{n0} \tag{4.14} $$

The vectors defined within the individual body frames are constant with respect to time so the result can be reduced to:

$$ {}^{0}\mathbf{v}^{n} = \sum_{k=1}^{n-1} {}^{k}\mathbf{q}^{k}\ \dot{\mathbf{R}}^{k0} + {}^{n}\mathbf{r}^{n}\ \dot{\mathbf{R}}^{n0} \tag{4.15} $$

The time derivative of the transformation matrix can be calculated as:

$$ \dot{\mathbf{R}}^{k0} = ({}^{k}\mathbf{Y}^{k0})^{T}\ \mathbf{R}^{k0} \tag{4.16} $$

where ${}^{k}\mathbf{Y}^{k0}$ is the skew-symmetric matrix of ${}^{k}\mathbf{w}^{k0}$, the absolute angular velocity of body k, defined in k local coordinates. Since ${}^{k}\mathbf{q}^{k}({}^{k}\mathbf{Y}^{k0})^{T}$ is equivalent to the cross product ${}^{k}\mathbf{q}^{k} \times -{}^{k}\mathbf{w}^{k0}$, and $\mathbf{u} \times \mathbf{v} = -\mathbf{v} \times \mathbf{u}$, Equation 4.15 can be written as:

$$ {}^{0}\mathbf{v}^{n} = \sum_{k=1}^{n-1} {}^{k}\mathbf{w}^{k0}\ {}^{k}\mathbf{S}_{q}^{k}\ \mathbf{R}^{k0} + {}^{n}\mathbf{w}^{n0}\ {}^{k}\mathbf{S}_{r}^{k}\ \mathbf{R}^{n0} \tag{4.17} $$

where ${}^{k}\mathbf{S}_{q}^{k}$ and ${}^{k}\mathbf{S}_{r}^{k}$ are the skew-symmetric matrices of ${}^{k}\mathbf{q}^{k}$ and ${}^{n}\mathbf{r}^{n}$, respectively. This equation can be simplified to:

$$ {}^{0}\mathbf{v}^{n} = \mathbf{w}\mathbf{V}^{n} \tag{4.18} $$

where $\mathbf{w} = [\ {}^{1}\mathbf{w}^{10}\ {}^{2}\mathbf{w}^{20}\ ...\ {}^{n}\mathbf{w}^{n0}]$ and $\mathbf{V}^{n}$ is referred to as the partial velocity matrix of body n defined by:

$$\mathbf{V}^n = \begin{bmatrix} {}^1\mathbf{S}_q^1\ \mathbf{R}^{10} \\ {}^2\mathbf{S}_q^2\ \mathbf{R}^{20} \\ \vdots \\ {}^{(n-1)}\mathbf{S}_q^{(n-1)}\ \mathbf{R}^{(n-1)0} \\ {}^n\mathbf{S}_r^n\ \mathbf{R}^{n0} \\ \mathbf{O} \\ \vdots \end{bmatrix} \tag{4.19}$$

In the ship–inverted pendulum system there are six DOF associated with the ship and twelve associated with the inverted pendulum, so the resulting partial velocity matrices (with dimensions 18×3) can be defined as:

$$\mathbf{V}^1 = \begin{bmatrix} \mathbf{S}_r^1\mathbf{R}^{10} \\ \mathbf{O} \\ \mathbf{O} \\ \mathbf{O} \\ \mathbf{O} \\ \mathbf{O} \end{bmatrix} \mathbf{V}^{1s} = \begin{bmatrix} \mathbf{S}_q^1\mathbf{R}^{10} \\ \mathbf{R}^{10} \\ \mathbf{O} \\ \mathbf{O} \\ \mathbf{O} \\ \mathbf{O} \end{bmatrix} \mathbf{V}^3 = \begin{bmatrix} \mathbf{S}_q^1\mathbf{R}^{10} \\ \mathbf{R}^{10} \\ \mathbf{S}_r^3\mathbf{R}^{30} \\ \mathbf{O} \\ \mathbf{O} \\ \mathbf{O} \end{bmatrix}$$

$$\mathbf{V}^4 = \begin{bmatrix} \mathbf{S}_q^1\mathbf{R}^{10} \\ \mathbf{R}^{10} \\ \mathbf{S}_q^3\mathbf{R}^{30} \\ \mathbf{S}_r^4\mathbf{R}^{40} \\ \mathbf{O} \\ \mathbf{O} \end{bmatrix} \mathbf{V}^5 = \begin{bmatrix} \mathbf{S}_q^1\mathbf{R}^{10} \\ \mathbf{R}^{10} \\ \mathbf{S}_q^3\mathbf{R}^{30} \\ \mathbf{S}_q^4\mathbf{R}^{40} \\ \mathbf{S}_r^5\mathbf{R}^{50} \\ \mathbf{O} \end{bmatrix} \mathbf{V}^6 = \begin{bmatrix} \mathbf{S}_q^1\mathbf{R}^{10} \\ \mathbf{R}^{10} \\ \mathbf{S}_q^3\mathbf{R}^{30} \\ \mathbf{S}_q^4\mathbf{R}^{40} \\ \mathbf{S}_q^5\mathbf{R}^{50} \\ \mathbf{S}_r^6\mathbf{R}^{60} \end{bmatrix} \tag{4.20}$$

where the superscript (^{s}) differentiates the ship translational DOF from angular DOF. The second entry in the matrices is simply $\mathbf{R}^{10}$ because it corresponds to the translational

DOF. In order to write Equation 4.18 in terms of the generalized coordinate derivatives, a transformation, $\mathbf{Q}$, can be defined such that:

$$^{0}\mathbf{v}^{n} = \mathbf{w}\mathbf{V}^{n} = \dot{\mathbf{x}}\mathbf{Q}\mathbf{V}^{n} = \dot{\mathbf{x}}\mathbf{V}_{Q}^{n} \tag{4.21}$$

where:

$$\mathbf{Q} = \begin{bmatrix} \mathbf{I} & \mathbf{R}^{01} & \mathbf{R}^{02} & \cdots & \mathbf{R}^{0n} \\ \mathbf{O} & \mathbf{I} & \mathbf{R}^{12} & \cdots & \mathbf{R}^{1n} \\ \mathbf{O} & \mathbf{O} & \mathbf{I} & \cdots & \mathbf{R}^{2n} \\ \vdots & \vdots & \ddots & \ddots & \vdots \\ \mathbf{O} & \mathbf{O} & \mathbf{O} & \mathbf{O} & \mathbf{I} \end{bmatrix} \tag{4.22}$$

For the ship–inverted pendulum model, this matrix is defined as:

$$\mathbf{Q} = \begin{bmatrix} \mathbf{I} & \mathbf{O} & \mathbf{R}^{13} & \mathbf{R}^{14} & \mathbf{R}^{15} & \mathbf{R}^{16} \\ \mathbf{O} & \mathbf{R}^{10} & \mathbf{O} & \mathbf{O} & \mathbf{O} & \mathbf{O} \\ \mathbf{O} & \mathbf{O} & \mathbf{I} & \mathbf{R}^{34} & \mathbf{R}^{35} & \mathbf{R}^{36} \\ \mathbf{O} & \mathbf{O} & \mathbf{O} & \mathbf{I} & \mathbf{R}^{45} & \mathbf{R}^{46} \\ \mathbf{O} & \mathbf{O} & \mathbf{O} & \mathbf{O} & \mathbf{I} & \mathbf{R}^{56} \\ \mathbf{O} & \mathbf{O} & \mathbf{O} & \mathbf{O} & \mathbf{O} & \mathbf{I} \end{bmatrix} \tag{4.23}$$

By inspection of Equation 4.21, it can be observed that for body k:

$$\mathbf{V}_{Q}^{k} = \frac{\partial \mathbf{v}^{k}}{\partial \dot{\mathbf{x}}^{k}} \tag{4.24}$$

Equation 4.21 can be differentiated with respect to time in order to obtain the acceleration of each body CoM:

$$ {}^{0}\dot{\mathbf{v}}^{n} = \frac{\mathrm{d}}{\mathrm{dt}}\, {}^{0}\mathbf{v}^{n} = \ddot{\mathbf{x}}\mathbf{V}_{Q}^{n} + \dot{\mathbf{x}}\dot{\mathbf{V}}_{Q}^{n} \tag{4.25} $$

The only term in Equation 4.25 that has not yet been defined is $\dot{\mathbf{V}}_{Q}^{n}$ which can be calculated from:

$$ \dot{\mathbf{V}}_{Q}^{n} = \mathbf{Q}\dot{\mathbf{V}}^{n} = \mathbf{Q} \begin{bmatrix} {}^{1}\mathbf{S}_{q}^{1}\ \dot{\mathbf{R}}^{10} \\ {}^{2}\mathbf{S}_{q}^{2}\ \dot{\mathbf{R}}^{20} \\ \vdots \\ {}^{(n-1)}\mathbf{S}_{q}^{(n-1)}\ \dot{\mathbf{R}}^{(n-1)0} \\ {}^{n}\mathbf{S}_{r}^{n}\ \dot{\mathbf{R}}^{n0} \\ \mathbf{O} \\ \vdots \end{bmatrix} \tag{4.26} $$

where $\dot{\mathbf{R}}^{k0}$ is defined by Equation 4.16. Equations 4.24 and 4.25 can be substituted into Equation 4.11 to obtain:

$$ \sum^{k} \left[\mathbf{f}^{k}(\mathbf{V}_{Q}^{k})^{T} = m^{k}\ddot{\mathbf{x}}\mathbf{V}_{Q}^{k}(\mathbf{V}_{Q}^{k})^{T} + m^{k}\dot{\mathbf{x}}\dot{\mathbf{V}}_{Q}^{k}(\mathbf{V}_{Q}^{k})^{T} \right] \tag{4.27} $$

The equation can then be rearranged using the matrix identity:

$$ \mathbf{A}\ \mathbf{B}\ \mathbf{C} = (\mathbf{C}^{T}\mathbf{B}^{T}\mathbf{A}^{T})^{T} \tag{4.28} $$

to obtain:

$$ \sum^{k} \left[\mathbf{V}_{Q}^{k}\mathbf{f}^{\ k} = m^{k}\mathbf{V}_{Q}^{k}(\mathbf{V}_{Q}^{k})^{T}\ddot{\mathbf{x}} + m^{k}\mathbf{V}_{Q}^{k}(\dot{\mathbf{V}}_{Q}^{k})^{T}\dot{\mathbf{x}} \right] \tag{4.29} $$

4.4.3 Angular Equations

The absolute angular velocity of body n in inertial coordinates can be defined as:

$$^{0}\mathbf{w}^{n} = \sum_{k=1}^{n} {}^{k}\dot{\mathbf{x}}^{k}\ \mathbf{R}^{k0} \tag{4.30}$$

This equation can be simplified to:

$$^{0}\mathbf{w}^{n} = \dot{\mathbf{x}}\mathbf{W}^{n} \tag{4.31}$$

where $\mathbf{W}^n$ is referred to as the partial angular velocity of body n defined by:

$$\mathbf{W}^{n} = \begin{bmatrix} \mathbf{R}^{10} \\ \mathbf{R}^{20} \\ \vdots \\ \mathbf{R}^{(n-1)0} \\ \mathbf{R}^{n0} \\ \mathbf{O} \\ \vdots \end{bmatrix} \tag{4.32}$$

The partial angular velocity matrices of the ship-inverted pendulum model are:

$$\mathbf{W}^{1} = \begin{bmatrix} \mathbf{R}^{10} \\ \mathbf{O} \\ \mathbf{O} \\ \mathbf{O} \\ \mathbf{O} \\ \mathbf{O} \end{bmatrix} \mathbf{W}^{1s} = \begin{bmatrix} \mathbf{O} \\ \mathbf{O} \\ \mathbf{O} \\ \mathbf{O} \\ \mathbf{O} \\ \mathbf{O} \end{bmatrix}$$

$$\mathbf{W}^3 = \begin{bmatrix} \mathbf{R}^{10} \\ \mathbf{O} \\ \mathbf{R}^{30} \\ \mathbf{O} \\ \mathbf{O} \\ \mathbf{O} \end{bmatrix} \mathbf{W}^4 = \begin{bmatrix} \mathbf{R}^{10} \\ \mathbf{O} \\ \mathbf{R}^{30} \\ \mathbf{R}^{40} \\ \mathbf{O} \\ \mathbf{O} \end{bmatrix} \mathbf{W}^5 = \begin{bmatrix} \mathbf{R}^{10} \\ \mathbf{O} \\ \mathbf{R}^{30} \\ \mathbf{R}^{40} \\ \mathbf{R}^{50} \\ \mathbf{O} \end{bmatrix} \mathbf{W}^6 = \begin{bmatrix} \mathbf{R}^{10} \\ \mathbf{O} \\ \mathbf{R}^{30} \\ \mathbf{R}^{40} \\ \mathbf{R}^{50} \\ \mathbf{R}^{60} \end{bmatrix} \tag{4.33}$$

On inspection of Equation 4.31, it can be observed that for body k:

$$\mathbf{W}^k = \frac{\partial \mathbf{w}^k}{\partial \dot{\mathbf{x}}^k} \tag{4.34}$$

Equation 4.31 can be differentiated with respect to time in order to obtain the angular acceleration of each body:

$${}^0\dot{\mathbf{w}}^n = \frac{\mathrm{d}}{\mathrm{dt}}\, {}^0\mathbf{w}^n = \ddot{\mathbf{x}}\mathbf{W}^n + \dot{\mathbf{x}}\dot{\mathbf{W}}^n \tag{4.35}$$

In this equation, the only undefined value is $\dot{\mathbf{W}}^n$ which is simply equal to:

$$\dot{\mathbf{W}}^n = \begin{bmatrix} \dot{\mathbf{R}}^{10} \\ \dot{\mathbf{R}}^{20} \\ \vdots \\ \dot{\mathbf{R}}^{(n-1)0} \\ \dot{\mathbf{R}}^{n0} \\ \mathbf{O} \\ \vdots \end{bmatrix} \tag{4.36}$$

where $\dot{\mathbf{R}}^{k0}$ is defined by Equation 4.16. Equations 4.31, 4.34, and 4.35 can be substituted into Equation 4.12 to obtain:

$$\sum^{k}\left[\mathbf{m}^{k}(\mathbf{W}^{k})^{T}=\ddot{\mathbf{x}}\mathbf{W}^{k}\mathbf{I}^{k0}(\mathbf{W}^{k})^{T}+\dot{\mathbf{x}}\dot{\mathbf{W}}^{k}\mathbf{I}^{k0}(\mathbf{W}^{k})^{T}+\dot{\mathbf{x}}\mathbf{W}^{k}\mathbf{\Omega}^{k0}(\mathbf{W}^{k})^{T}\right] \tag{4.37}$$

where $\mathbf{\Omega}^{k0}$ is the skew-symmetric matrix of $\dot{\mathbf{x}}(\mathbf{W}^{k})(\mathbf{I}^{k0})$, and:

$$\mathbf{I}^{k0}=(\mathbf{R}^{k0})^{T}({}^{k}\mathbf{I}^{k})\mathbf{R}^{k0} \tag{4.38}$$

where ${}^{k}\mathbf{I}^{k}$ is the inertia matrix of body k about its centre of mass in local body coordinates. Equation 4.37 can be rearranged using the identity in Equation 4.28 to obtain:

$$\sum^{k}\left[\mathbf{W}^{k}\mathbf{m}^{k}=\mathbf{W}^{k}\mathbf{I}^{0k}(\mathbf{W}^{k})^{T}\ddot{\mathbf{x}}+\mathbf{W}^{k}\mathbf{I}^{0k}(\dot{\mathbf{W}}^{k})^{T}\dot{\mathbf{x}}+\mathbf{W}^{k}\mathbf{\Omega}^{0k}(\mathbf{W}^{k})^{T}\dot{\mathbf{x}}\right] \tag{4.39}$$

4.4.4 Combined Equations

Equations 4.29 and 4.39 can be combined since they are written in terms of the same variables and the following similar terms can be collected:

$$\mathbf{A}=\sum^{k}\left[m^{k}\mathbf{V}_{Q}^{k}(\mathbf{V}_{Q}^{k})^{T}+\mathbf{W}^{k}\mathbf{I}^{0k}(\mathbf{W}^{k})^{T}\right] \tag{4.40}$$

$$\mathbf{B}=\sum^{k}\left[m^{k}\mathbf{V}_{Q}^{k}(\dot{\mathbf{V}}_{Q}^{k})^{T}+\mathbf{W}^{k}\mathbf{I}^{0k}(\dot{\mathbf{W}}^{k})^{T}\right] \tag{4.41}$$

$$\mathbf{C}=\sum^{k}\mathbf{W}^{k}\mathbf{\Omega}^{0k}(\mathbf{W}^{k})^{T} \tag{4.42}$$

$$\boldsymbol{f}=\sum^{k}\mathbf{V}_{Q}^{k}\mathbf{f}^{\,k}+\sum^{k}\mathbf{W}^{k}\mathbf{m}^{k} \tag{4.43}$$

The equations of motion can then be simply written as:

$$\mathbf{A}\ddot{\mathbf{x}}+\mathbf{B}\dot{\mathbf{x}}+\mathbf{C}\dot{\mathbf{x}}=\boldsymbol{f} \tag{4.44}$$

where **A** contains the mass and inertia-related terms, and where **B** and **C** contain the linear and nonlinear velocity-related terms respectively. The right-side term $\boldsymbol{f}$ contains the external forces and moments acting on the system.

4.4.5 Forces and Moments

The sum of the forces and moments acting on each of the system's bodies are **f** and **m** respectively. The only external forces are the force of gravity acting on each link which is formulated as:

$$\mathbf{f}^{\,k} = \sum^{k} \mathbf{V}_Q^k m^k \, {}^0\mathbf{g} \tag{4.45}$$

where ${}^0\mathbf{g}$ is equal to (0, 0, -9.807) m/s^2. The forces acting between the links do not need to be included explicitly in the equations since it is assumed that there is no relative translational motion between the links. The sums of the moments are the control moments acting on each link.

The control moments are calculated as the moments that would be generated directly at the joint, and thus would be applied to both links that the joint is connected to. Therefore, the total contribution to $\boldsymbol{f}$ would be calculated as:

$$\mathbf{m}^k = \sum^{k} \mathbf{W}^k({}^0\mathbf{m}^k - \, {}^0\mathbf{m}^{k+1}) = \sum^{k} \mathbf{W}^k \mathbf{m}^{0k} \tag{4.46}$$

where the control algorithm calculates ${}^k\mathbf{m}^k$ and:

$${}^0\mathbf{m}^k = \, {}^k\mathbf{m}^k \, \mathbf{R}^{k0} \tag{4.47}$$

The control system will be discussed in detail in Chapter 5.

4.4.6 Prescribed Ship Motion

The model's first six DOF are ship angular and translational motions, and thus have already been determined a priori either through past simulations or from experimental measurements. This means that Equation 4.44 can be rearranged (with $\mathbf{y}$ substituted for $\dot{\mathbf{x}}$ in order to avoid confusion with specific generalized coordinate derivatives defined at the start of this chapter) as:

$$\mathbf{A}\dot{\mathbf{y}} = \boldsymbol{f} - \mathbf{B}\mathbf{y} - \mathbf{C}\mathbf{y} = \mathbf{d} \tag{4.48}$$

and partitioned by degrees of freedom as:

$$\begin{bmatrix} \underset{6x6}{\begin{bmatrix} \mathbf{A}_1 \end{bmatrix}} & \underset{6x12}{\begin{bmatrix} \mathbf{A}_2 \end{bmatrix}} \\ \underset{12x6}{\begin{bmatrix} \mathbf{A}_3 \end{bmatrix}} & \underset{12x12}{\begin{bmatrix} \mathbf{A}_4 \end{bmatrix}} \end{bmatrix} \begin{bmatrix} \underset{6x1}{\begin{bmatrix} \dot{\mathbf{y}}_1 \end{bmatrix}} \\ \underset{12x1}{\begin{bmatrix} \dot{\mathbf{y}}_2 \end{bmatrix}} \end{bmatrix} = \begin{bmatrix} \underset{6x1}{\begin{bmatrix} \mathbf{d}_1 \end{bmatrix}} \\ \underset{12x1}{\begin{bmatrix} \mathbf{d}_2 \end{bmatrix}} \end{bmatrix} \tag{4.49}$$

where $\mathbf{A}_1$, $\mathbf{A}_2$, $\mathbf{d}_1$, and $\dot{\mathbf{y}}_1$ correspond to the equations for the ship DOF and $\mathbf{A}_3$, $\mathbf{A}_4$, $\mathbf{d}_2$, and $\dot{\mathbf{y}}_2$ correspond to the equations for the inverted pendulum DOF. This allows the dynamic problem to be solved using the lower partition:

$$\underset{12x12}{\begin{bmatrix} \mathbf{A}_4 \end{bmatrix}} \underset{12x1}{\begin{bmatrix} \dot{\mathbf{y}}_2 \end{bmatrix}} = \underset{12x1}{\begin{bmatrix} \mathbf{d}_2 \end{bmatrix}} - \underset{12x6}{\begin{bmatrix} \mathbf{A}_3 \end{bmatrix}} \underset{6x1}{\begin{bmatrix} \dot{\mathbf{y}}_1 \end{bmatrix}} \tag{4.50}$$

This is convenient because $\mathbf{A_1}$ contains the mass properties of the ship and $\mathbf{d}_1$ contains the external forces acting on the ship, both of which are unknown. However, if the ship inertial properties were known, the applied forces could be determined, should they be of interest. Further, it is observed that the fully-coupled nature of the equations is retained such that the effect of the inverted pendulum on the ship, though small in practice, is not neglected.

4.4.7 Ship – Pendulum Reaction Forces

The translational DOF are defined such that they represent the accelerations of the ship in the ship frame rather than the inertial frame. They are modelled this way because the ship acceleration data, that typically will be used with the model, is usually recorded in the ship frame with an inertial sensor located near the point of interest. Alternatively, if obtained from simulation, it could be expressed in this coordinate frame. This avoids the need to transform the data to the point of interest which would require knowledge of the location of the centre of mass of the ship which is not generally known and is not constant due to consumption of fuel, potable water, stores, and active stabilization systems (when present and engaged).

It is useful to be able to solve for the translational reaction forces between the ship and the inverted pendulum. By adding new unknown force terms to the corresponding equations that were removed in the previous section, one can rearrange the equations to solve for the reaction forces while still including the prescribed ship accelerations. Following the form of the gravitational forces presented in Equation 4.45, these forces can be added to the equations in the form of:

$$\mathbf{V}_Q^{1s}\mathbf{f}^{1s} \tag{4.51}$$

where $\mathbf{f}^{1s}$ are the forces and $\mathbf{V}_Q^{1s}$ is the partial velocity matrix for the translational DOF as defined by Equation 4.20. If Equation 4.50 is rewritten to include the equations for the first six DOF it would appear as:

$$\begin{bmatrix} \begin{bmatrix} \mathbf{O} \end{bmatrix}_{18x6} & \begin{bmatrix} \begin{bmatrix} \mathbf{A}_2 \end{bmatrix}_{6x12} \\ \begin{bmatrix} \mathbf{A}_4 \end{bmatrix}_{12x12} \end{bmatrix} \end{bmatrix} \begin{bmatrix} \begin{bmatrix} \mathbf{O} \end{bmatrix}_{6x1} \\ \begin{bmatrix} \dot{\mathbf{y}}_2 \end{bmatrix}_{12x1} \end{bmatrix} = \begin{bmatrix} \begin{bmatrix} \mathbf{O} \end{bmatrix}_{6x1} \\ \begin{bmatrix} \mathbf{d}_2 \end{bmatrix}_{12x1} \end{bmatrix} - \begin{bmatrix} \begin{bmatrix} \mathbf{A}_1 \end{bmatrix}_{6x6} \\ \begin{bmatrix} \mathbf{A}_3 \end{bmatrix}_{12x6} \end{bmatrix} \begin{bmatrix} \dot{\mathbf{y}}_1 \end{bmatrix}_{6x1} + \begin{bmatrix} \mathbf{V}_Q^{1s} \end{bmatrix}_{18x3} \begin{bmatrix} \mathbf{f}^{1s} \end{bmatrix}_{3x1} \tag{4.52}$$

The $\mathbf{V}_Q^{1s}\mathbf{f}^{1s}$ term can be brought over to the left side of the equation and the equations corresponding to the ship angular DOF removed, to obtain:

$$\begin{bmatrix} \begin{bmatrix} \mathbf{V}_Q^{1s} \end{bmatrix}_{15x3} & \begin{bmatrix} \begin{bmatrix} \mathbf{A}_2 \end{bmatrix}_{3x12} \\ \begin{bmatrix} \mathbf{A}_4 \end{bmatrix}_{12x12} \end{bmatrix} \end{bmatrix} \begin{bmatrix} \begin{bmatrix} \mathbf{f}^{1s} \end{bmatrix}_{3x1} \\ \begin{bmatrix} \dot{\mathbf{y}}_2 \end{bmatrix}_{12x1} \end{bmatrix} = \begin{bmatrix} \begin{bmatrix} \mathbf{O} \end{bmatrix}_{3x1} \\ \begin{bmatrix} \mathbf{d}_2 \end{bmatrix}_{12x1} \end{bmatrix} - \begin{bmatrix} \begin{bmatrix} \mathbf{A}_1 \end{bmatrix}_{3x6} \\ \begin{bmatrix} \mathbf{A}_3 \end{bmatrix}_{12x6} \end{bmatrix} \begin{bmatrix} \dot{\mathbf{y}}_1 \end{bmatrix}_{6x1} \tag{4.53}$$

In this form the translational reaction forces can be solved for using the same mathematical procedure used to solve for the angular accelerations.

4.4.8 Joint Constraints

In order to temporarily simplify the model to compare it to other models it is useful to be able to constrain the DOF of the inverted pendulum. This can be done by simply removing any control forces, setting the positions and speeds of those DOF to zero at each time step, and removing the acceleration terms from the equations of motion. Furthermore, the equations for those DOF can be easily modified to solve for joint reaction moments instead of the accelerations. Since relative angular velocity components between bodies are used as generalized speeds, the constraining moment components will appear uncoupled in the corresponding equations [57]. For example, all of the joints can be locked and reaction moments solved for in Equation 4.53 by setting all of the $\dot{\mathbf{y}}$ terms to zero and substituting with terms that allow one to solve for the reaction moments instead. The result with substitutions on the left hand side of the equation is:

$$\left[\begin{bmatrix} -\mathbf{V}_Q^{1s} \end{bmatrix}_{15\text{x}3} \begin{bmatrix} -\mathbf{W}^3 \end{bmatrix}_{15\text{x}3} \begin{bmatrix} -\mathbf{W}^4 \end{bmatrix}_{15\text{x}3} \begin{bmatrix} -\mathbf{W}^5 \end{bmatrix}_{15\text{x}3} \begin{bmatrix} -\mathbf{W}^6 \end{bmatrix}_{15\text{x}3}\right] \begin{bmatrix} \mathbf{f}^{1s} \\ \mathbf{m}^{03} \\ \mathbf{m}^{04} \\ \mathbf{m}^{05} \\ \mathbf{m}^{06} \end{bmatrix} = \begin{bmatrix} \mathbf{d} \end{bmatrix}_{15\text{x}1} - \begin{bmatrix} \begin{bmatrix} \mathbf{A}_1 \end{bmatrix}_{3\text{x}6} \\ \begin{bmatrix} \mathbf{A}_3 \end{bmatrix}_{12\text{x}6} \end{bmatrix} \begin{bmatrix} \dot{\mathbf{y}}_1 \end{bmatrix}_{6\text{x}1} \tag{4.54}$$

where $\mathbf{m}^{0k}$ are the sum of the moments acting on body k as defined in Equation 4.46.

4.4.9 Inverse Dynamics

If instead of setting the inverted pendulum kinematics to zero they are set to prescribed values, the reaction moments solved for in the previous section would instead become the control moments that would be required to achieve the specified system state. The equations in this case would take the form:

$$\left[\begin{bmatrix} -\mathbf{V}_Q^{1s} \end{bmatrix}_{15\text{x}3} \begin{bmatrix} -\mathbf{W}^3 \end{bmatrix}_{15\text{x}3} \begin{bmatrix} -\mathbf{W}^4 \end{bmatrix}_{15\text{x}3} \begin{bmatrix} -\mathbf{W}^5 \end{bmatrix}_{15\text{x}3} \begin{bmatrix} -\mathbf{W}^6 \end{bmatrix}_{15\text{x}3}\right] \begin{bmatrix} \mathbf{f}^{1s} \\ \mathbf{m}^{03} \\ \mathbf{m}^{04} \\ \mathbf{m}^{05} \\ \mathbf{m}^{06} \end{bmatrix} = \begin{bmatrix} \mathbf{d} \end{bmatrix}_{15\text{x}1} - \begin{bmatrix} \mathbf{A} \end{bmatrix}_{15\text{x}18} \begin{bmatrix} \dot{\mathbf{y}} \end{bmatrix}_{18\text{x}1} \tag{4.55}$$

where all of the accelerations ($\dot{\mathbf{y}}$) and angular velocities and orientations contained in $\mathbf{d}$

($\mathbf{y}$ and $\boldsymbol{\theta}$) would be determined in advance.

4.4.10 Numerical Solution

As it was shown with Equation 4.44 and the preceding sections which derived its components, the equations of motion can be written as:

$$\mathbf{A}(\boldsymbol{\theta})\ddot{\mathbf{x}} + \mathbf{B}(\boldsymbol{\theta})\dot{\mathbf{x}} + \mathbf{C}(\boldsymbol{\theta}, \dot{\mathbf{x}})\dot{\mathbf{x}} = \boldsymbol{f}(\boldsymbol{\theta}) \tag{4.56}$$

which indicates that all of $\mathbf{A}$, $\mathbf{B}$, $\mathbf{C}$, and $\boldsymbol{f}$ are functions of the current state and therefore must be recalculated at each time step of the simulation. When performing a simulation using this equation the only unknown is $\ddot{\mathbf{x}}$ so the equation can be rearranged as:

$$\ddot{\mathbf{x}} = \mathbf{A}^{-1}(\boldsymbol{f} - \mathbf{B}\dot{\mathbf{x}} - \mathbf{C}\dot{\mathbf{x}}) \tag{4.57}$$

In order to use this equation with a time integration algorithm it is necessary to reduce it in order from N second order differential equations to $2N$ first order differential equations. One approach is to write,

$$\begin{bmatrix} \dot{\boldsymbol{\theta}} \\ \ddot{\mathbf{x}} \end{bmatrix} = \begin{bmatrix} \mathbf{T}\dot{\mathbf{x}} \\ \mathbf{A}^{-1}(\boldsymbol{f} - \mathbf{B}\dot{\mathbf{x}} - \mathbf{C}\dot{\mathbf{x}}) \end{bmatrix} \tag{4.58}$$

where $\mathbf{T}$ is the transformation from generalized coordinate derivatives, $\dot{\mathbf{x}}$, to Bryant angle derivatives, $\dot{\boldsymbol{\theta}}$. These equations are numerically integrated to calculate updated values of $\dot{\mathbf{x}}$ and $\boldsymbol{\theta}$ at each time step. The matrix $\mathbf{T}$ is defined as:

$$\mathbf{T} = \begin{bmatrix} \mathbf{T}^3 & O & O & O \\ O & \mathbf{T}^4 & O & O \\ O & O & \mathbf{T}^5 & O \\ O & O & O & \mathbf{T}^6 \end{bmatrix} \tag{4.59}$$

where $\mathbf{T}^k$ is defined as [53]:

$$\mathbf{T}^k = \frac{1}{\cos(\theta_2^k)} \begin{bmatrix} \cos(\theta_3^k) & -\sin(\theta_3^k) & 0 \\ \sin(\theta_3^k)\cos(\theta_2^k) & \cos(\theta_3^k)\cos(\theta_2^k) & 0 \\ -\cos(\theta_3^k)\sin(\theta_2^k) & \sin(\theta_3^k)\sin(\theta_2^k) & \cos(\theta_2^k) \end{bmatrix} \tag{4.60}$$

The superscript k corresponds to the body number. This equation is undefined if θ_2^k is equal to $\frac{\pi}{2} \pm n\pi$, which is outside of the range of possible states for the simulation, and therefore not a concern.

4.4.11 Time Integration Method

A numerical integration algorithm is used in dynamic simulations to determine updated state positions and velocities after calculating the updated state accelerations based on the dynamics of the system. If the current state of the system is $\mathbf{z}$, the derivatives of the state vector are $\dot{\mathbf{z}}$, and the time step is h, then the simulation can be propagated, in theory, using Euler integration:

$$\mathbf{z}_{n+1} = \mathbf{z}_n + h \cdot \dot{\mathbf{z}}_{n+1} \tag{4.61}$$

This first-order integration procedure was found to be insufficient for calculating the four-link inverted pendulum dynamics due to the requirement of a very small time step. Therefore, a fourth-order Runge-Kutta algorithm was used instead. A standard formulation of the procedure is as follows. Let:

$$\dot{\mathbf{z}}_{n+1} = f(\mathbf{z}_n, t_n) \tag{4.62}$$

where $\mathbf{z}_n$ is the current state and t_n is the current time. Next define:

$$\begin{aligned} \mathbf{f}_1 &= h \cdot f(\mathbf{z}_n, t_n) \\ \mathbf{f}_2 &= h \cdot f(\mathbf{z}_n + 0.5\mathbf{f}_1, t_n + 0.5h) \\ \mathbf{f}_3 &= h \cdot f(\mathbf{z}_n + 0.5\mathbf{f}_2, t_n + 0.5h) \\ \mathbf{f}_4 &= h \cdot f(\mathbf{z}_n + \mathbf{f}_3, t_n + h) \end{aligned} \tag{4.63}$$

Since later f values depend on earlier ones, these calculations must be performed sequentially. The current state is then updated using:

$$\mathbf{z}_{n+1} = \mathbf{z}_n + \frac{1}{6}(\mathbf{f}_1 + 2\mathbf{f}_2 + 2\mathbf{f}_3 + \mathbf{f}_4) \tag{4.64}$$

There is one detail that must be observed in the time integration of Equations 4.58 when they have been modified for constraint cases defined in Section 4.4.8; if a joint is locked, care must be taken to not treat the reaction moments as accelerations and include them in the first N equations.

4.4.12 Simulation Procedure

After initialization of all files and variables, the simulation cycles through the following procedure.

1. Interpolate the current ship state from an input file at the current time. Assign ship motions to simulation state variables after rotating them into simulation coordinates.

2. Calculate control forces and moments based on the current state.

3. Update system dynamics using an RK4 integration algorithm (Section 4.4.11), which solves for accelerations four times per simulation time step (detailed below). Use updated control forces if they are available.

4. Update Bryant angles and generalized coordinate derivatives using Equation 4.64.

5. Save data for that time step to output variables.

The input arguments for the function that calculates system accelerations are the inverted pendulum states $\boldsymbol{\theta}^3$, $\boldsymbol{\theta}^4$, $\boldsymbol{\theta}^5$, $\boldsymbol{\theta}^6$ and $\dot{\mathbf{x}}^3$, $\dot{\mathbf{x}}^4$, $\dot{\mathbf{x}}^5$, $\dot{\mathbf{x}}^6$, the ship motion states $\boldsymbol{\theta}^{\mathbf{1}}$, $\dot{\mathbf{x}}^{\mathbf{1(s)}}$, and $\ddot{\mathbf{x}}^{\mathbf{1(s)}}$, and the control moments $\mathbf{m}^3$, $\mathbf{m}^4$, $\mathbf{m}^5$, $\mathbf{m}^6$. It then performs the following steps.

1. Calculate rotation matrices between each local frame and the global frame, $\mathbf{R}^{k0}$.

2. Using the angular velocities from the previous time step, calculate the rotation matrix derivatives, $\dot{\mathbf{R}}^{k0}$.

3. Define the angular partial velocity matrices, $\mathbf{W}^k$, and partial velocity matrices, $\mathbf{V}^k$, and their derivatives, for each body.

4. Rotate each inertia matrix $\mathbf{I}^k$ from local coordinates to global coordinates to obtain $\mathbf{I}^{k0}$.

5. Calculate $\boldsymbol{\Omega}^{0k}$ for each body.

6. Premultiply each partial velocity matrix by $\mathbf{Q}$.

7. Calculate $\mathbf{A}$, $\mathbf{B}$, $\mathbf{C}$, and $\boldsymbol{f}$ from Equations 4.40 through 4.43.

8. If an entire joint is constrained, replace the corresponding rows and columns in $\mathbf{A}$ with reaction moment coefficients. If individual DOF are constrained, set the rows

and columns to zero and do not include the equation rows corresponding to those DOF in the solution.

9. Solve for $\ddot{\mathbf{x}}$ and $\dot{\boldsymbol{\theta}}$.

4.4.13 Dynamics Code

The code that simulates the dynamic equations of the four-link inverted pendulum was written in MATLAB and the primary function which calculates $\ddot{\mathbf{x}}$ is included in Appendix B. This function has been included to show how the dynamics equations, when coded, are made up of simple products of the transformation matrices and geometrical properties of the model, rather than long strings of algebraic equations containing individual geometric components and many trigonometric functions as is common when dealing with multibody dynamics equations. This is one of the primary advantages of this dynamics derivation procedure.

4.5 Validation

The behaviour of the four-link inverted pendulum model, 4BAR, was compared with three existing models that were created by members of the Carleton University Applied Dynamics Laboratory. The models were assigned the same mass properties and exposed to the same ship motions and control forces, and their states and reaction forces were compared.

The first model, GRM3D, was equivalent to having all four inverted pendulum joints constrained. The second model, PSM3D, was equivalent to having all but the first joint constrained. Input ship motion for these validations was obtained from two sources. The first was simulated ship data that was originally used to validate GRM3D against PSM3D. The second was actual ship motion data recorded during the recent heavy-weather sea trial aboard the Quest research vessel [48] using an inertial sensor. The third model was equivalent to having no joints constrained, but gravity terms were not included and input ship motion was limited to one DOF of translation.

In addition to the published models, a model was built in MATLAB Simulink with the SimMechanics toolkit (SIM3D) for each of the above validation cases, as well as for an additional case that expands the third model to also include gravity forces and one DOF of angular motion.

4.5.1 SimMechanics Model

SimMechanics is a modelling tool for dynamic systems available as an add-on to MATLAB Simulink. It is a useful tool for prototype design of linkages and control systems. A Simulink model, referred to as SIM3D, of the inverted pendulum dynamics was developed in order to aid in the design of the control system for the four-link inverted pendulum model. This model was also used as an additional source of validation for the derived model.

Figure 4.3 shows the SimMechanics model that was developed for the majority of the validation tests. It contains a ship motion 'joint' which actuates a ship deck body. That body is connected to the inverted pendulum joint and body. The inverted pendulum joint is modelled as a joint with two rotational DOF with axes of [1 0 0] and [0 1 0]. The inverted pendulum is controlled with a PD control system which takes the pendulum position and angular velocity as proportional and derivative inputs, respectively. For the multi-link test case, all of the SimMechanics blocks except for the two ship-related components were replicated three times and connected to each other.

Since the primary use of the SIM3D model was to add an additional validation case for the 4BAR model, the following sections will only include the numerical results comparing SIM3D to 4BAR in order to show that the SIM3D model was a valid model of the system.

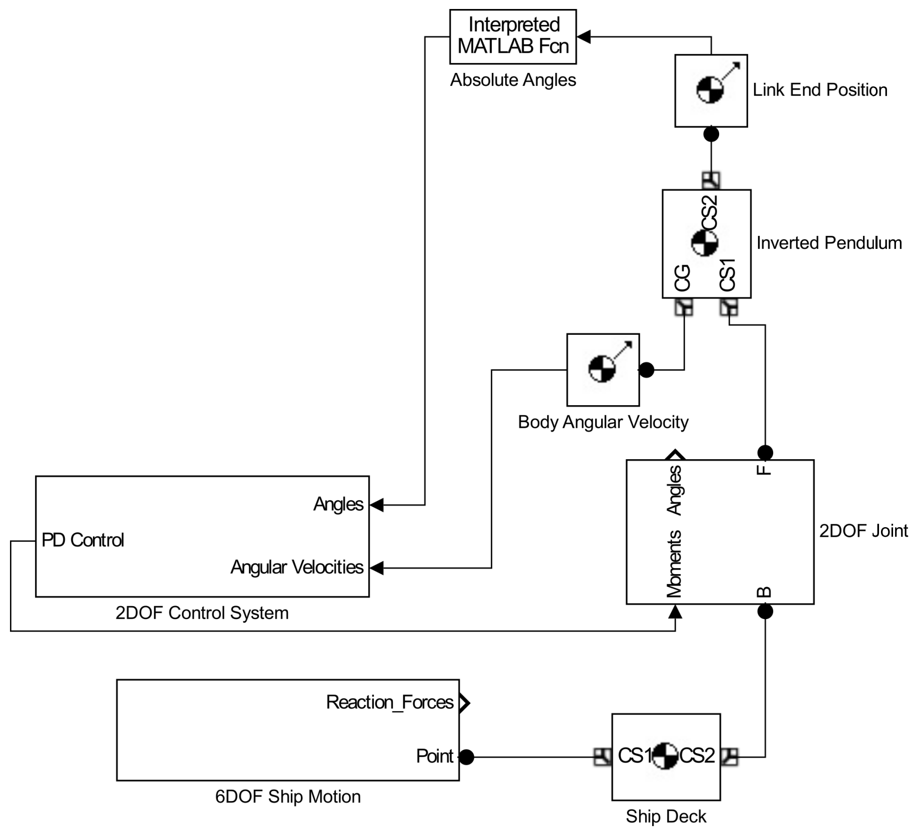

Figure 4.3: SimMechanics model of single-link inverted pendulum subjected to six-DOF ship motion.

4.5.2 Mass and Inertia Equivalence

In order to properly compare the 4BAR model to GRM3D and PSM3D the mass and inertia properties of the models were required to be equivalent. For these comparisons the 4BAR model was assumed to consist of four links of equivalent mass and inertia. Therefore the mass of each of the links was one fourth the mass of the models with one link. The value of I_{zz}, the mass moment of inertia about the yaw axis, was also one fourth of the inertia of a single link. The roll and pitch inertia properties required additional calculations for their determination.

Consider the two model diagrams in Figure 4.4. If one were to write the inertia about the centre of mass of link (a) in terms of the inertia properties of the links in (b) it would

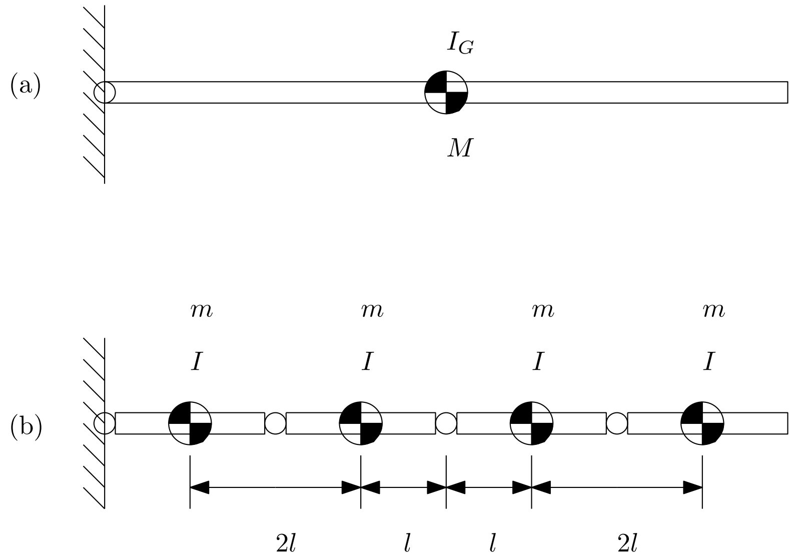

Figure 4.4: Inverted pendulum with (a) one link as in GRM3D/PSM3D and (b) four links as in 4BAR.

be:

$$I_G = 2(I + ml^2 + I + m(3l)^2) \tag{4.65}$$

This can be reduced to:

$$I_G = 4I + 20ml^2 \tag{4.66}$$

and rearranged for I to obtain:

$$I = \frac{1}{4}I_G - 5ml^2 \tag{4.67}$$

Table 4.1 contains the mass properties for the two models.

Table 4.1: Mass and length properties of PSM3D/GRM3D (one segment) and 4BAR (four constrained segments).

	Link Mass	Link Length	I_{xx}	I_{yy}	I_{zz}
Single Segment	78.0 kg	1.74 m	47.2 kg·m^2	47.2 kg·m^2	1.00 kg·m^2
Multi-segment	19.5 kg	0.435 m	7.19 kg·m^2	7.19 kg·m^2	0.250 kg·m^2

4.5.3 Validation Tests Metric

The metric used to compare the simulation results between models is called a normalized root mean square error (NRMSE) and is defined as:

$$NRMSE\ (\%) = \frac{\sqrt{\frac{1}{n}\sum(x_i^1 - x_i^2)^2}}{x_{max} - x_{min}} \times 100 \tag{4.68}$$

where x_i^1 and x_i^2 are corresponding data points from the reference and validated data sets, n is the number of data points, and x_{max} and x_{min} are the maximum and minimum values of the validated data set.

Root mean square error is a useful metric for evaluation of the differences between data sets when data are cyclic with respect to time. With standard percent error calculations, error calculations become inflated when both data sets approach zero which is less of an issue with root mean square calculations. A sample of these two types of error calculations are shown in Figure 4.5. The first graph shows two data sets which are nearly identical. The second graph shows the error calculated using a standard absolute percent error formula, and the third graph shows the error calculated using Equation 4.68 with the $\frac{1}{n}$ and $\sum$ terms removed. It can clearly be seen in the figure that the percent error graph displays many very large errors when the difference between the measurements is small, but large compared to the magnitude of the instantaneous measurements.

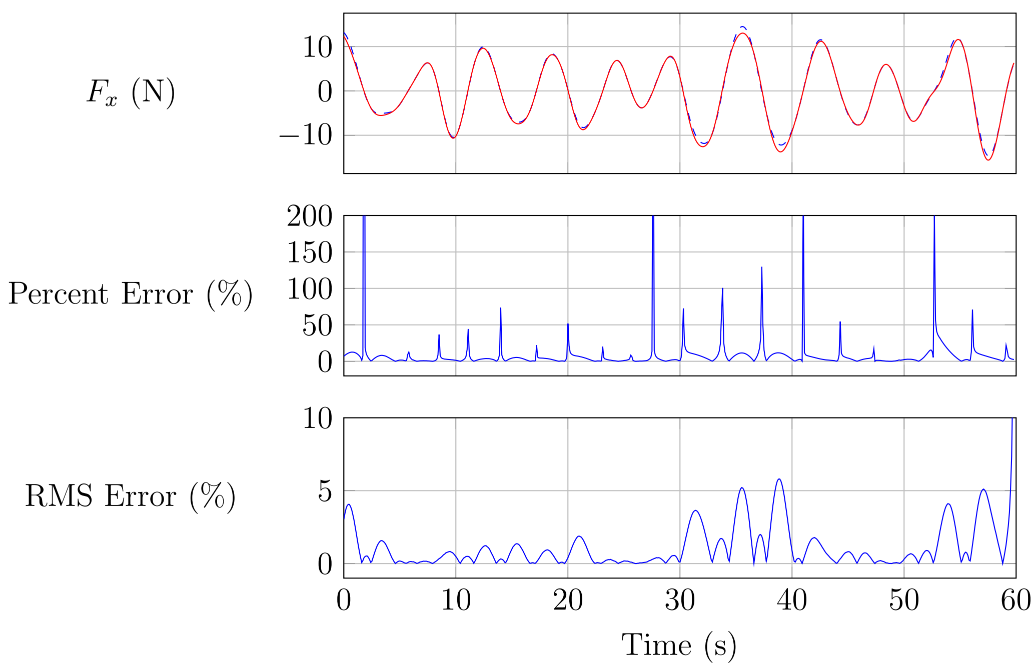

Figure 4.5: Comparison of percent error with RMS error.

4.5.4 Validation with GRM3D

Graham's model is a 2D rigid body model having no DOF relative to a ship base which itself has one DOF of angular motion and two DOF of translational motion. The model is intended for studying human reactions to ship motion [1]. GRM3D, shown in Figure 4.6, is a spatial version of Graham's model that can be simulated in FORTRAN for any six-DOF input deck motion and with various options for attachments to a hanging pendulum or a cart load [58]. Its equations were derived using a Newton-Euler approach. If all of the joints in the 4BAR model are locked as formulated in Equation 4.54, then it should behave the same as GRM3D, which provides an opportunity for model validation.

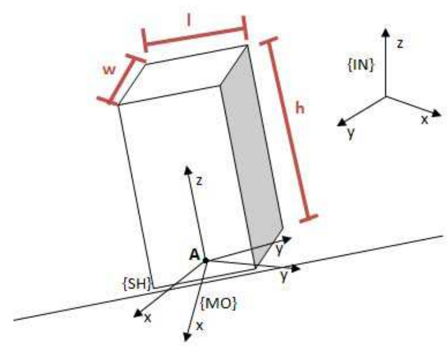

Figure 4.6: Diagram of GRM3D model [58].

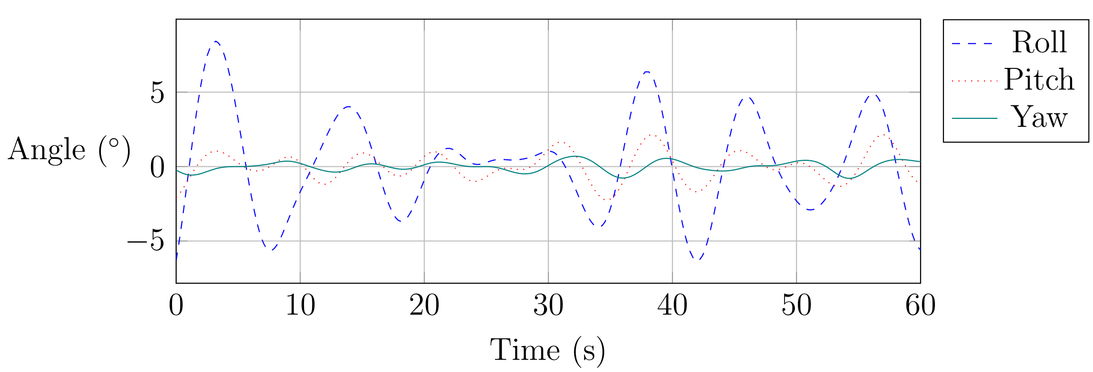

Figure 4.7: Bryant angles of simulated ship motions used in comparison between GRM3D and 4BAR.

The simulated ship motion included velocities, accelerations, angular orientations, angular velocities, and angular accelerations. The angular motions are shown in Figure 4.7. Reaction forces and moments were compared between the two models and the results are shown in Figures 4.8 and 4.9.

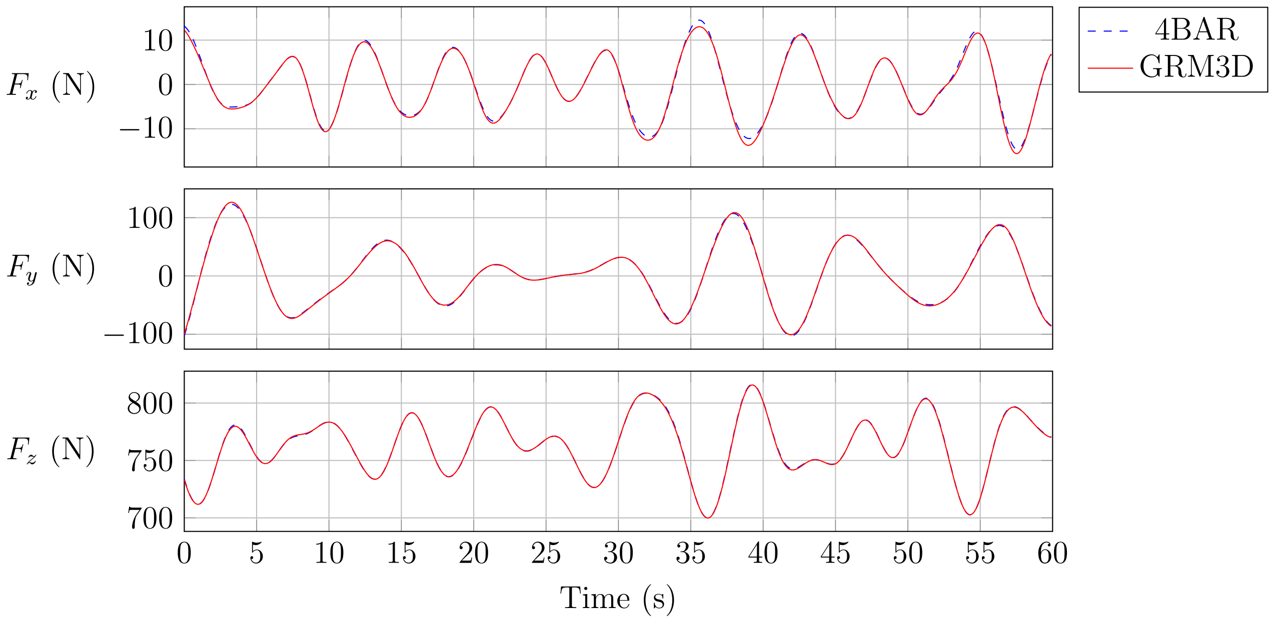

Figure 4.8: Comparison of reaction forces between 4BAR and GRM3D. NRMSE 1.6% (F_x), 0.56% (F_y), and 0.38% (F_z).

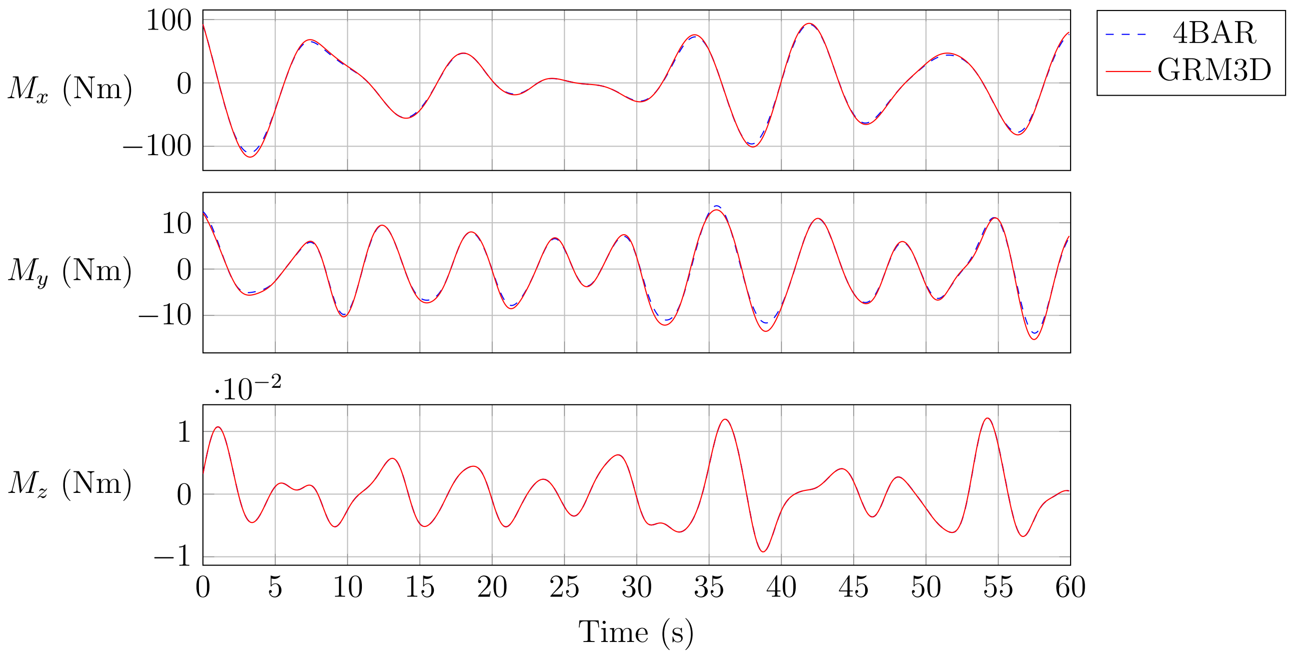

Figure 4.9: Comparison of reaction moments between 4BAR and GRM3D. NRMSE 0.98% (M_x), 1.7% (M_y), and 0.014% (M_z).

It can be seen in Figures 4.8 and 4.9 that the results match very closely. The NRMSE results are summarized in Table 4.2. The results of comparing 4BAR to SIM3D are also included to show that the SIM3D model produced results similar to the other two models when its joints were constrained.

Table 4.2: Normalized root mean square error (NRMSE) results for all validation tests between 4BAR and GRM3D, and between 4BAR and SIM3D.

Model	F_x	F_y	F_z	M_x	M_y	M_z
GRM3D	1.601	0.5624	0.3782	0.9791	1.691	0.01374
SIM3D	1.5918	0.5589	0.3522	0.5409	1.461	1.3×10^{-12}

4.5.5 Validation with PSM3D

PSM3D is a single-segment, single-joint spatial inverted pendulum postural stability model [9] simulated in FORTRAN. It was also derived using a Newton-Euler approach. A diagram of the model is shown in Figure 4.10. In the figure, frame 'SH' corresponds to frame (1) in 4BAR, frame 'MO' corresponds to frame (2), and frame 'LO' corresponds to frame (3). PSM3D can also be simulated under any prescribed motions and has various options for attachments to other rigid bodies and loadings. If all of the four-link inverted pendulum's joints are locked except for the most-inboard one, then it should behave the same as the PSM3D inverted pendulum model.

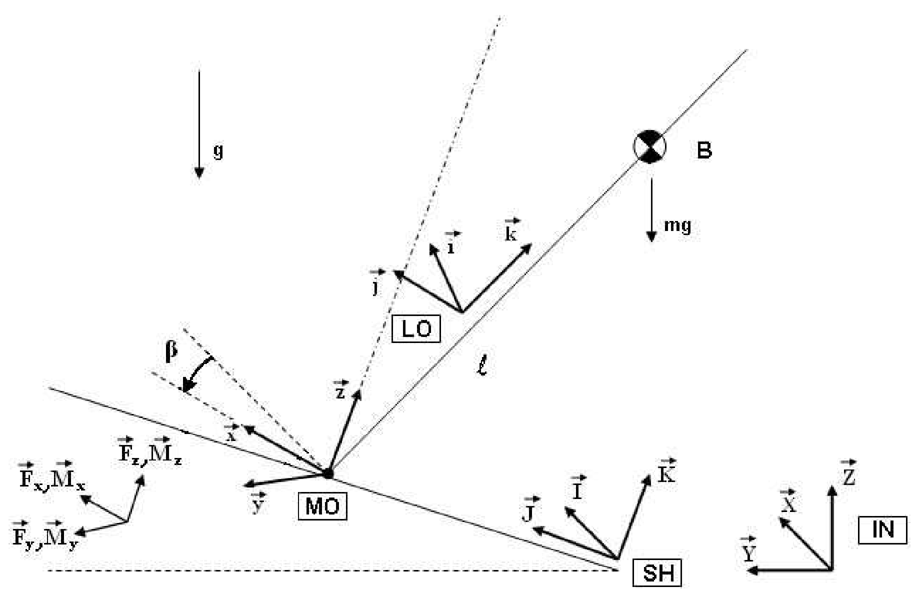

Figure 4.10: Diagram of PSM3D model [9].

In order to replicate identical behaviour as the single-link inverted pendulum it was necessary to implement a controller in the four-link model that was equivalent to the controller implemented in the single-link model. In PSM3D there are control moments calculated for roll and pitch. The control moments are calculated as:

$$\begin{aligned} M_{Ax} &= T_{x\ control} = A_{kx}\theta_{tot\ x} + A_{cx}\dot{\theta}_{tot\ x} \\ M_{Ay} &= T_{y\ control} = A_{ky}\theta_{tot\ y} + A_{cy}\dot{\theta}_{tot\ y} \end{aligned} \tag{4.69}$$

where the total angles, $\theta_{tot\ x}$ and $\theta_{tot\ y}$, and angular rates, $\dot{\theta}_{tot\ x}$ and $\dot{\theta}_{tot\ y}$, are measured relative to the absolute vertical reference in the inertial frame. The angles can be easily calculated if one knows the relative position of any point on the inverted pendulum that is not at the link origin. The end point of the first link can be calculated as:

$${}^{0}\mathbf{p}^{3} = \cancel{{}^{1}\mathbf{q}^{1}\mathbf{R}^{10}} + {}^{3}\mathbf{q}^{3}\mathbf{R}^{30} = {}^{3}\mathbf{q}^{3}\mathbf{R}^{30} \tag{4.70}$$

Since the ship coordinate system is located at the inverted pendulum attachment point ${}^{1}\mathbf{q}^{1}$ is equal to zero. The total angles can then be calculated as:

$$\begin{aligned} \theta_{tot\ x} &= -\mathrm{atan}({}^{0}p_2^3/\ {}^{0}p_3^3) \\ \theta_{tot\ y} &= \ \ \mathrm{atan}({}^{0}p_1^3/\ {}^{0}p_3^3) \end{aligned}$$

The total angular velocity of the link can be calculated by adding the angular velocity of the ship to the angular velocity of the inverted pendulum in inertial coordinates such that:

$$\dot{\boldsymbol{\theta}}_{tot} = \begin{bmatrix} \dot{\theta}_{tot\ x} \\ \dot{\theta}_{tot\ y} \\ \dot{\theta}_{tot\ z} \end{bmatrix} = \dot{\mathbf{x}}^{1}\mathbf{R}^{10} + \dot{\mathbf{x}}^{3}\mathbf{R}^{30} \tag{4.71}$$

Validation Test 1: Generated Ship Motion Data

The two models were first compared using the same generated ship motion file that was used for the GRM3D comparison shown in Figure 4.7.

The following graphs compare the inverted pendulum roll and pitch angles (Figure 4.11), reaction forces (Figure 4.12), and control moments (Figure 4.13). Since the results are often very close, the normalized errors are included in the captions, as well as at the end of the PSM3D validation section.

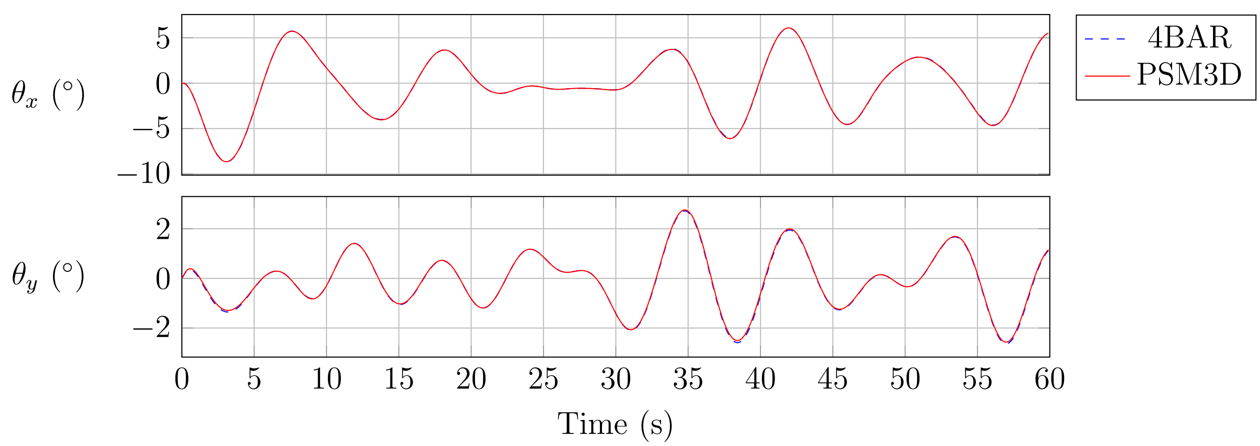

Figure 4.11: Validation Test 1 angles for 4BAR and PSM3D. NRMSE 0.16% (θ_x) and 0.69% (θ_y).

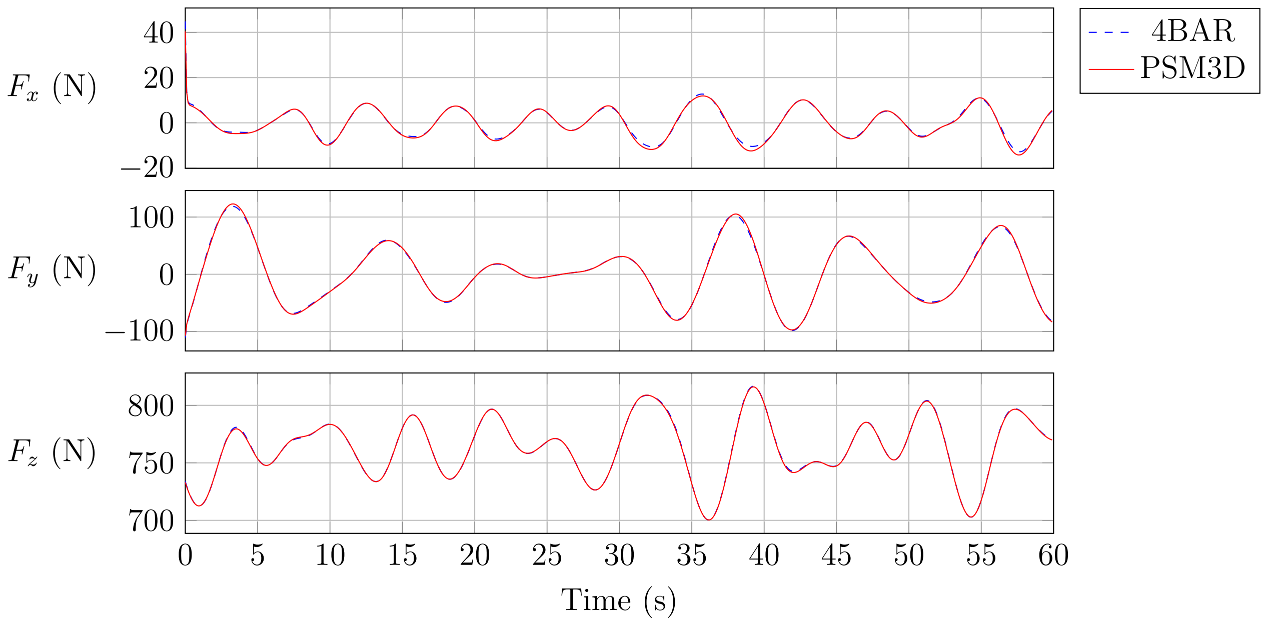

Figure 4.12: Validation Test 1 reaction forces for 4BAR and PSM3D. NRMSE 0.99% (F_x), 0.67% (F_y), and 0.40% (F_z).

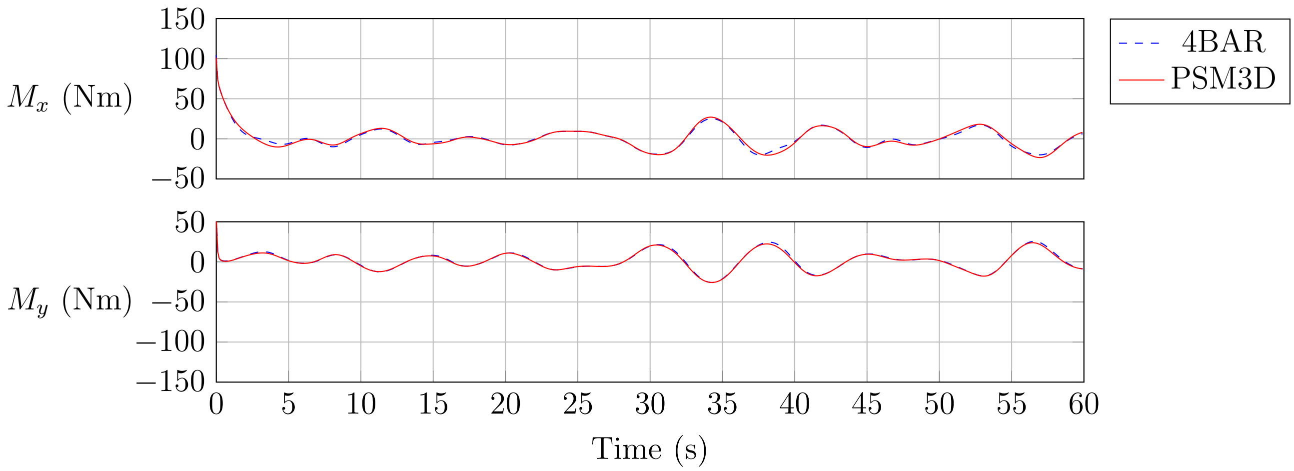

Figure 4.13: Validation Test 1 control moments for 4BAR and PSM3D. NRMSE 1.4% (M_x) and 1.1% (M_y).

Validation Test 2: AHRS Ship Data 1

Test 2 was performed with a six-minute IMU ship data recording. The ship angular motions are shown in Figure 4.14. Figures 4.15 through 4.17 compare the inverted pendulum angles, reaction forces, and control moments.

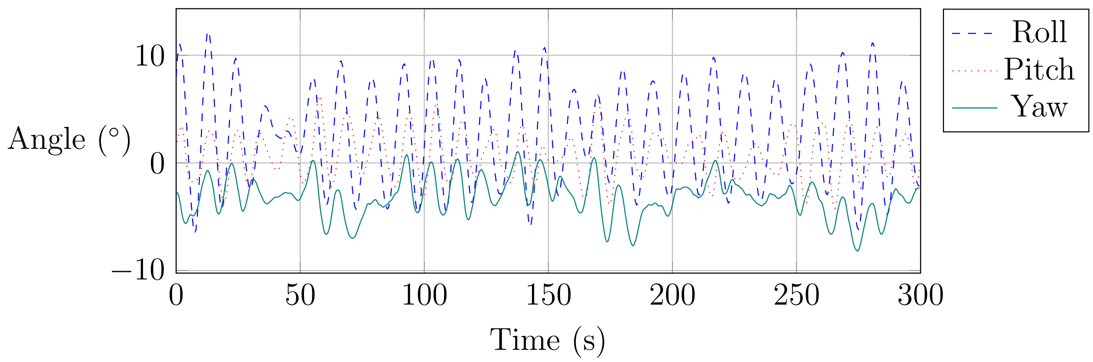

Figure 4.14: Validation Test 2 angular values of IMU-measured ship motions.

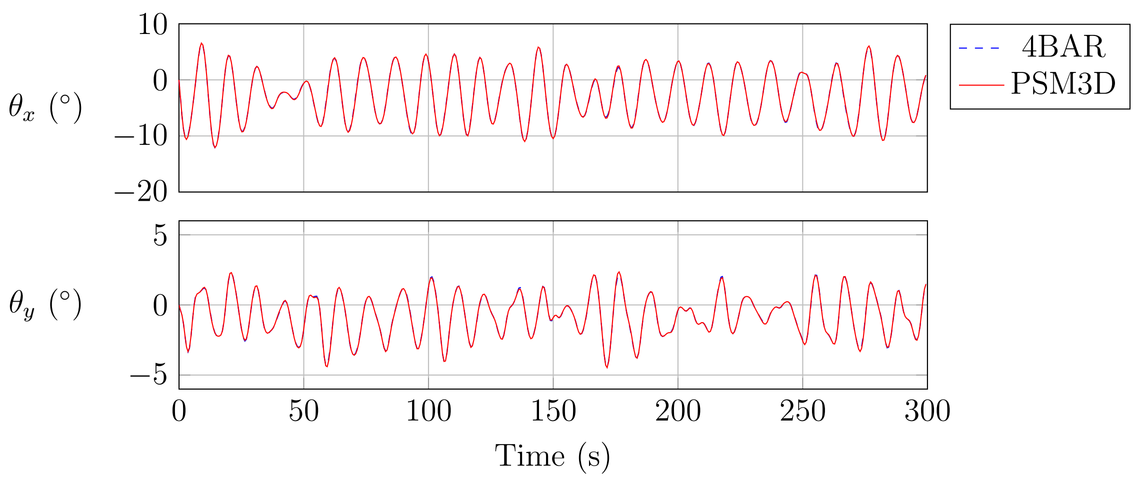

Figure 4.15: Validation Test 2 angles for 4BAR and PSM3D. NRMSE 0.61% (θ_x) and 0.65% (θ_y).

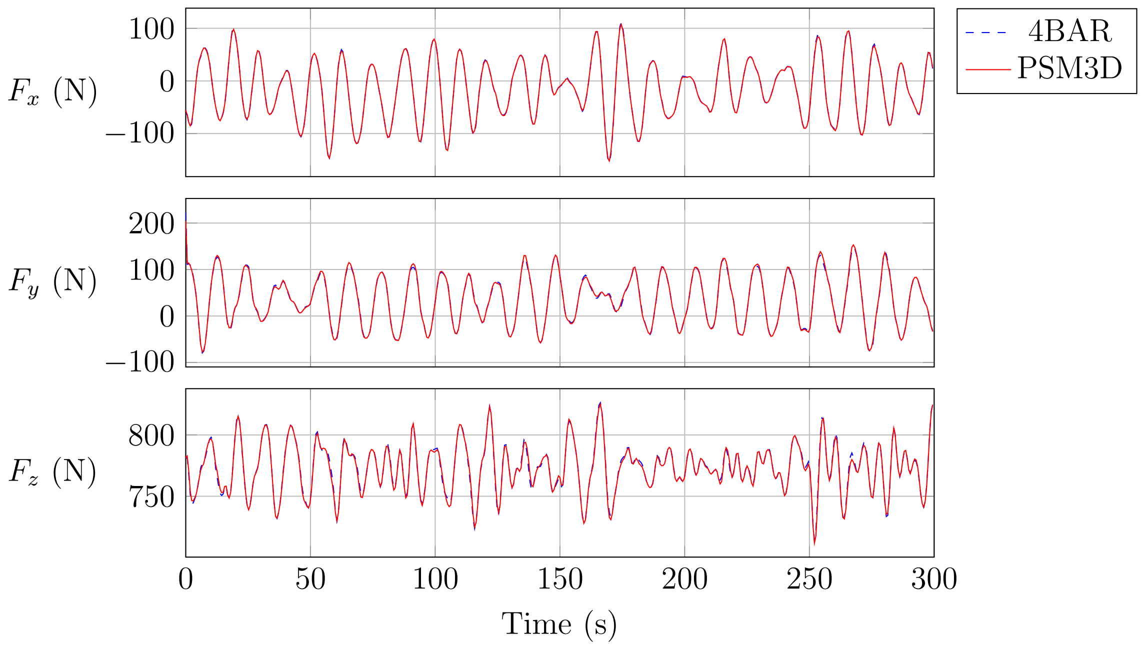

Figure 4.16: Validation Test 2 reaction forces for 4BAR and PSM3D. NRMSE 0.46% (F_x), 0.86% (F_y), and 1.5% (F_z).

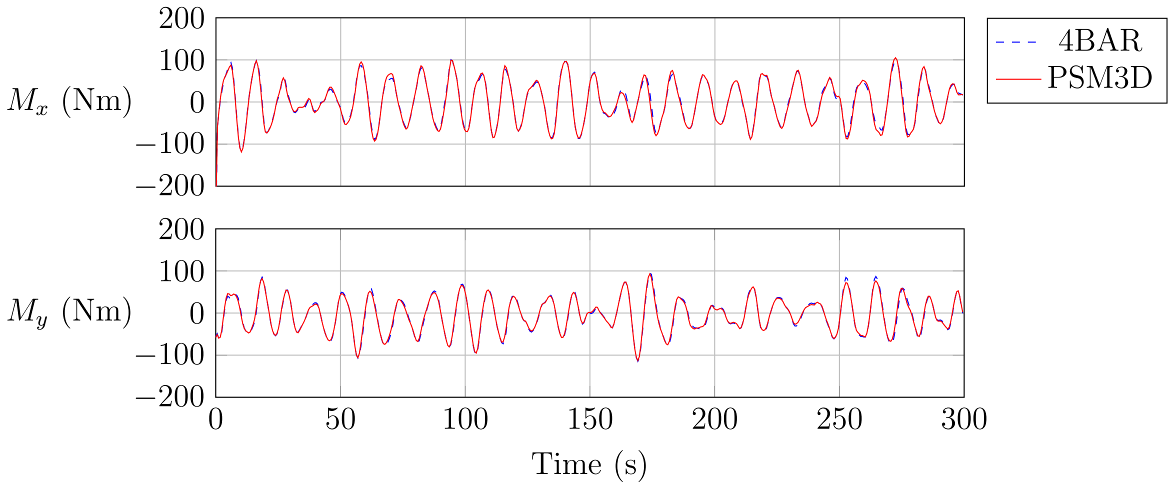

Figure 4.17: Validation Test 2 control moments for 4BAR and PSM3D. NRMSE 1.4% (M_x) and 1.9% (M_y).

Validation Test 3: AHRS Ship Data 2

Test 3 was performed with another six-minute AHRS data recording. The ship angular motions are shown in Figure 4.18. This recording was selected because the ranges of the motions differed from those in Test 2. Specifically, the motion was less dominated by roll, and the yaw offset was greater. Figures 4.19 through 4.21 compare the inverted pendulum angles, reaction forces, and control moments.

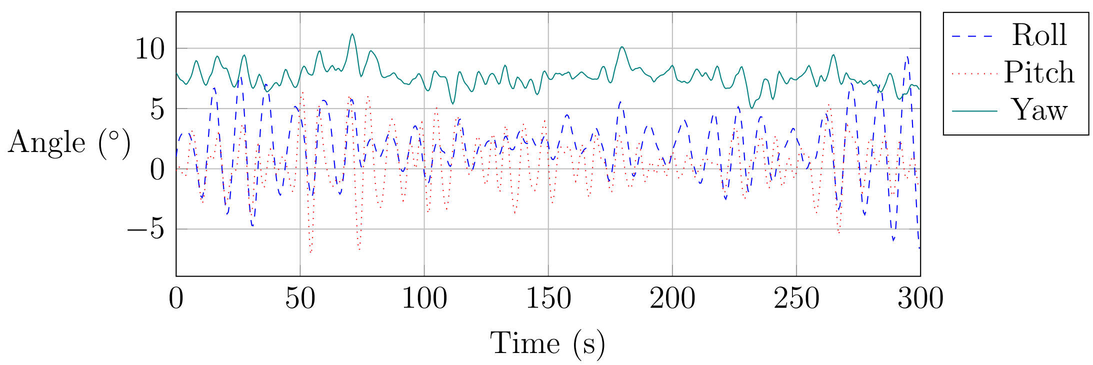

Figure 4.18: Validation Test 3 angular values of IMU-measured ship motions.

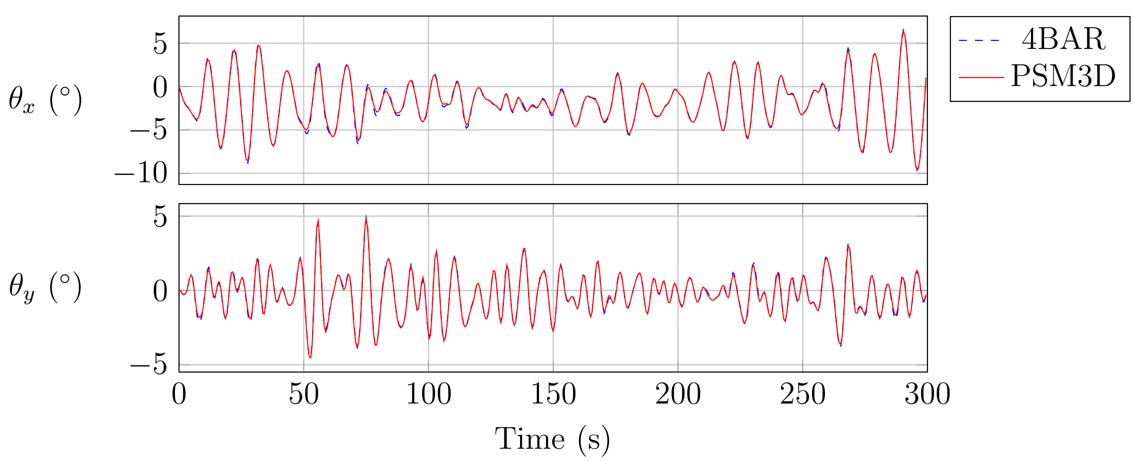

Figure 4.19: Validation Test 3 angles for 4BAR and PSM3D. NRMSE 1.0% (θ_x) and 1.0% (θ_y).

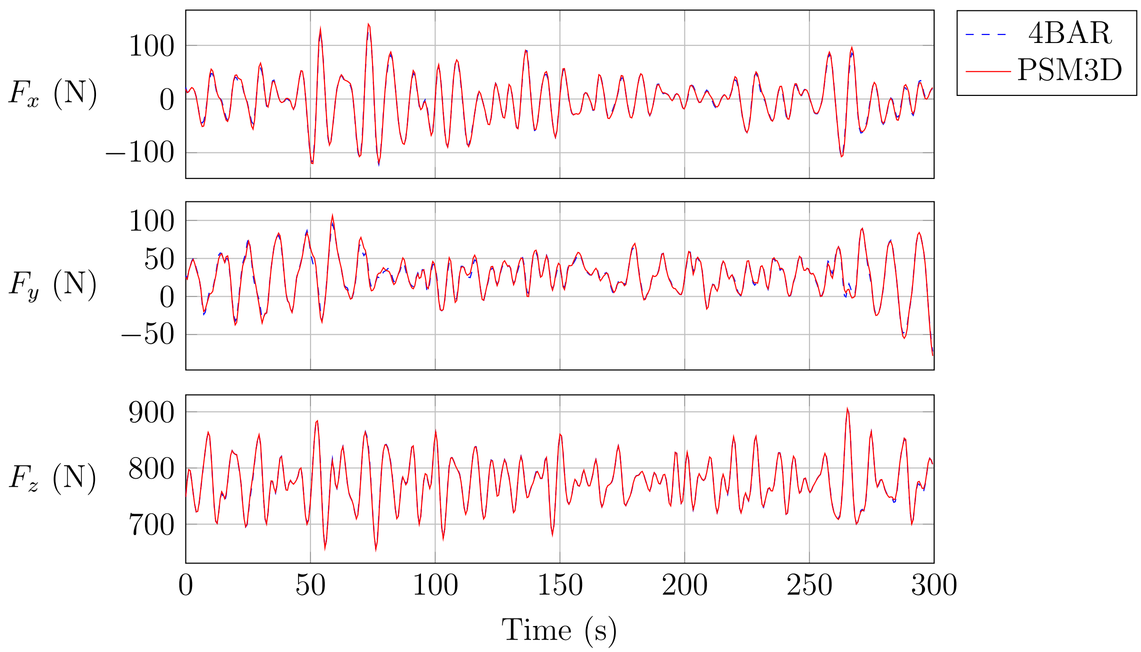

Figure 4.20: Validation Test 3 reaction forces for 4BAR and PSM3D. NRMSE 1.3% (F_x), 1.6% (F_y), and 0.59% (F_z).

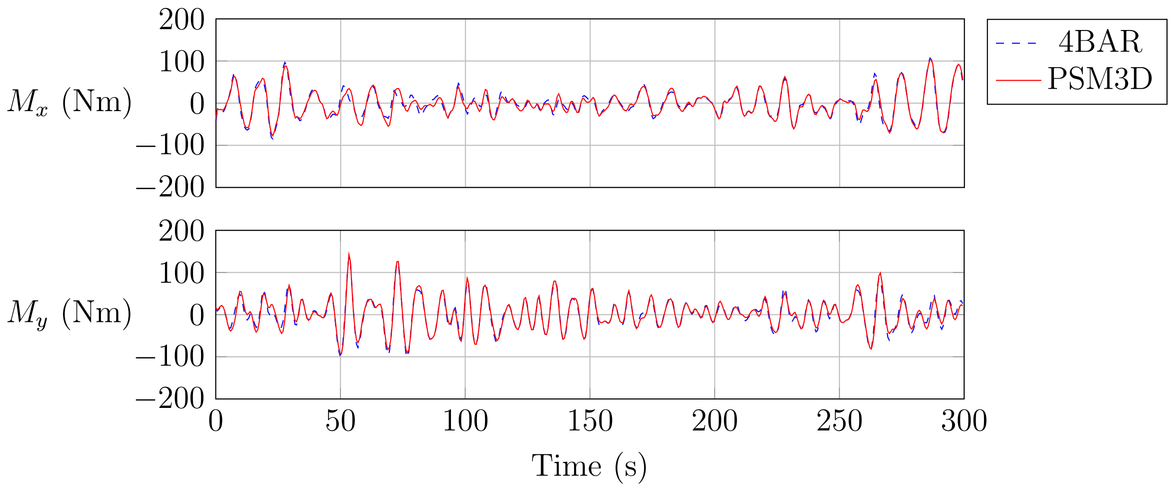

Figure 4.21: Validation Test 3 control moments for 4BAR and PSM3D. NRMSE 4.2% (M_x) and 3.1% (M_y).

Validation Test 4: AHRS Ship Data 3

Test 4 was performed with a forty-minute AHRS data recording in order to test whether the models remained consistent over a long period of time. Figures 4.22 through 4.24 compare the inverted pendulum angles, reaction forces, and control moments, for the last 10 minutes of the simulation.

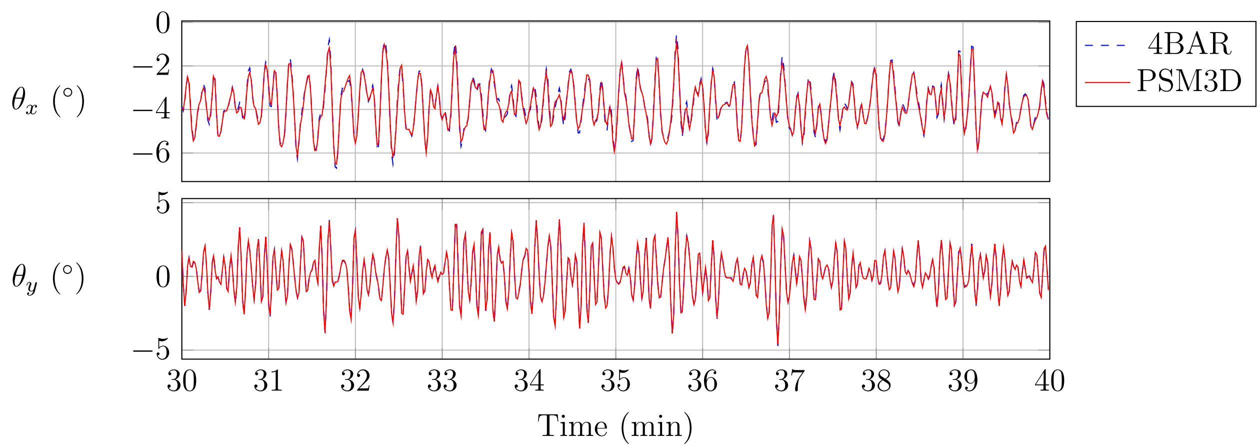

Figure 4.22: Validation Test 4 angles for 4BAR and PSM3D. NRMSE 1.7% (θ_x) and 0.59% (θ_y).

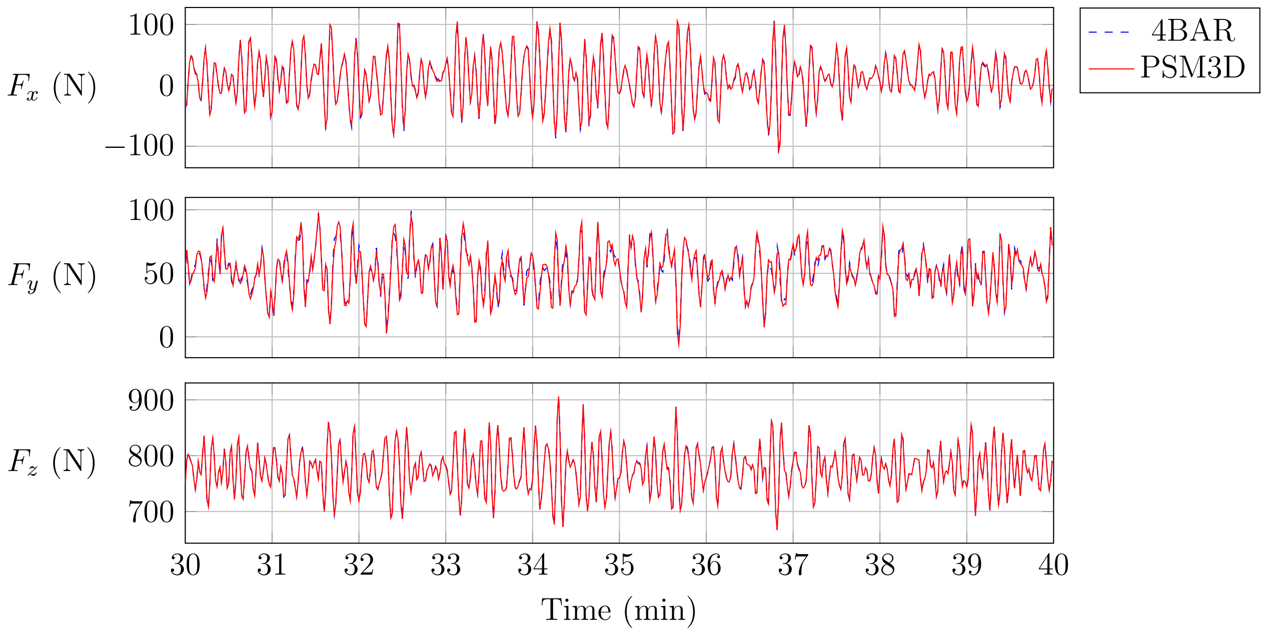

Figure 4.23: Validation Test 4 reaction forces for 4BAR and PSM3D. NRMSE 0.86% (F_x), 1.6% (F_y), and 0.48% (F_z).

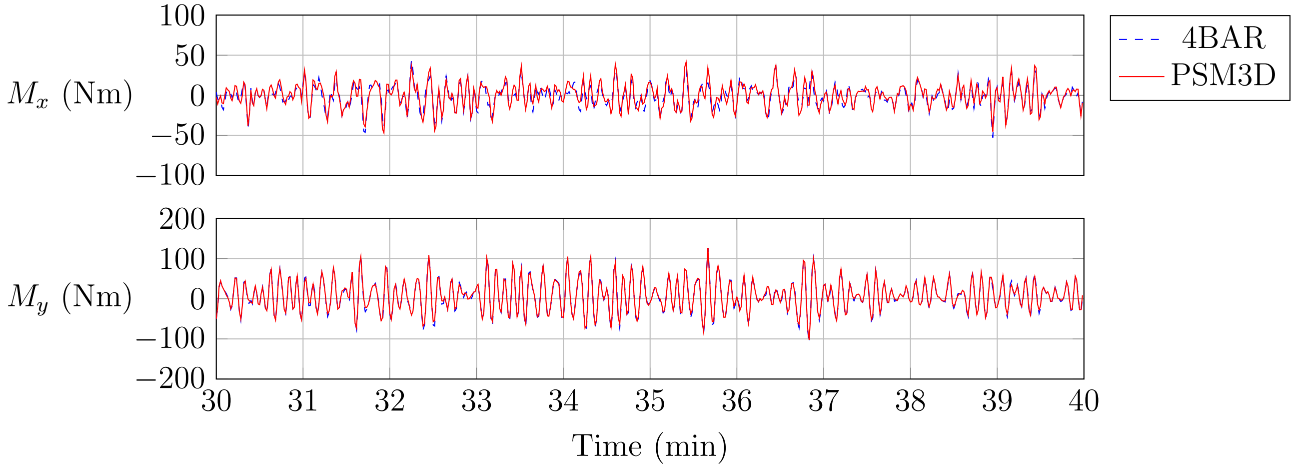

Figure 4.24: Validation Test 4 control moments for 4BAR and PSM3D. NRMSE 2.2% (M_x) and 1.6% (M_y).

Summary of Error Results

Table 4.3 shows the NRMSE results for all of the tests that were calculated between 4BAR and PSM3D. Similar tests were carried out between 4BAR and SIM3D and the results are shown in Table 4.4. All of the test results show that the models match closely when simulated under equivalent conditions.

Table 4.3: Normalized root mean square error (NRMSE) results for all validation tests between 4BAR and PSM3D.

	Test 1 (%)	Test 2 (%)	Test 3 (%)	Test 4 (%)
θ_x	0.1632	0.6121	1.0476	1.6527
θ_y	0.6859	0.6529	1.0433	0.5939
$\dot{x}_1$	0.2604	0.6725	1.4188	1.8641
$\dot{x}_2$	0.2921	0.8234	0.8975	0.6110
$\ddot{x}_1$	4.3396	0.5477	1.8491	0.2573
$\ddot{x}_2$	0.9267	1.3536	4.4321	3.4262
F_x	0.9937	0.4575	1.2516	0.8565
F_y	0.6674	0.8580	1.6452	1.5585
F_z	0.4005	1.5378	0.5939	0.4796
M_x	1.4449	1.3686	4.1833	2.1835
M_z	1.0885	1.9040	3.0509	1.5516

Table 4.4: Normalized root mean square error (NRMSE) results for all validation tests between 4BAR and SIM3D.

	Test 1 (%)	Test 2 (%)	Test 3 (%)	Test 4 (%)
θ_x	0.2022	0.6955	1.0570	1.6485
θ_y	0.7168	0.6660	1.0672	0.5713
$\dot{x}_1$	0.3376	1.2153	3.3498	4.7533
$\dot{x}_2$	0.6025	3.8150	1.8816	0.7545
$\ddot{x}_1$	0.4544	0.1090	1.1945	0.3370
$\ddot{x}_2$	0.5402	0.1114	0.6295	0.1389
F_x	0.7602	0.4396	1.2673	0.8364
F_y	0.5569	0.8680	1.6473	1.4248
F_z	0.3524	1.5106	0.5929	0.4626
M_x	0.9971	1.3484	4.1987	1.9705
M_z	0.7776	1.7988	2.9731	1.4115

4.5.6 Validation of Multiple Links

For validation of the model with no joints constrained there was not a spatial model readily available, so instead a comparison was made with a published 2D cart-inverted-pendulum model shown in Figure 4.25 [59].

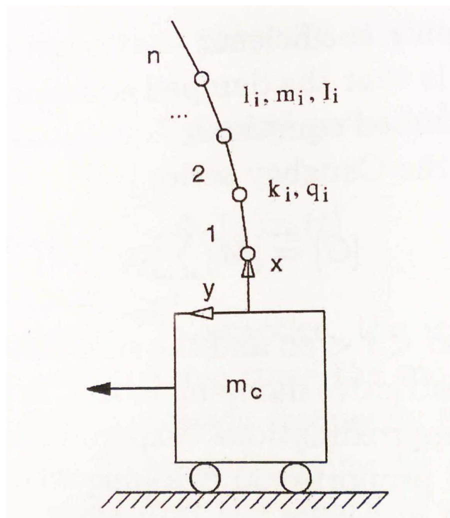

Figure 4.25: Diagram of cart and multi-link inverted pendulum model [59].

The published equations of motion for the cart-inverted pendulum model, evaluated for the case of 4 segments representing the beam, were:

$$\mathbf{A}\ddot{\mathbf{x}} + \mathbf{C}\dot{\mathbf{x}} + \mathbf{K}\mathbf{x} = 0 \tag{4.72}$$

with mass, damping, and stiffness matrices defined as:

$$\mathbf{A} = \begin{bmatrix} 5m + m_c & -\frac{7}{2}ml & -\frac{5}{2}ml & -\frac{3}{2}ml & -\frac{1}{2}ml \\ -\frac{7}{2}ml & \frac{13}{4}ml^2 + I & \frac{5}{2}ml^2 & \frac{3}{2}ml^2 & \frac{1}{2}ml^2 \\ -\frac{5}{2}ml & \frac{5}{2}ml^2 & \frac{9}{4}ml^2 + I & \frac{3}{2}ml^2 & \frac{1}{2}ml^2 \\ -\frac{3}{2}ml & \frac{3}{2}ml^2 & \frac{3}{2}ml^2 & \frac{5}{4}ml^2 + I & \frac{1}{2}ml^2 \\ -\frac{1}{2}ml & \frac{1}{2}ml^2 & \frac{1}{2}ml^2 & \frac{1}{2}ml^2 & \frac{1}{4}ml^2 + I \end{bmatrix} \tag{4.73}$$

$$\mathbf{C} = \begin{bmatrix} 0 & 0 & 0 & 0 & 0 \\ 0 & c_1 + c_2 & -c_2 & 0 & 0 \\ 0 & -c_2 & c_2 + c_3 & -c_3 & 0 \\ 0 & 0 & -c_3 & c_3 + c_4 & -c_4 \\ 0 & 0 & 0 & -c_4 & c_4 \end{bmatrix} \tag{4.74}$$

$$\mathbf{K} = \begin{bmatrix} 0 & 0 & 0 & 0 & 0 \\ 0 & k_1 + k_2 & -k_2 & 0 & 0 \\ 0 & -k_2 & k_2 + k_3 & -k_3 & 0 \\ 0 & 0 & -k_3 & k_3 + k_4 & -k_4 \\ 0 & 0 & 0 & -k_4 & k_4 \end{bmatrix} \tag{4.75}$$

The equations were derived using a Lagrange-based approach. In 2D the only difference between the cart-inverted pendulum model and the ship-inverted pendulum model is that the ship can experience rotational motion as well as translational motion. For this test, the input ship motion, taken from the first minute of PSM3D Validation Test 4, was reduced to one DOF translational motion. The acceleration data for this test is shown in Figure 4.26.

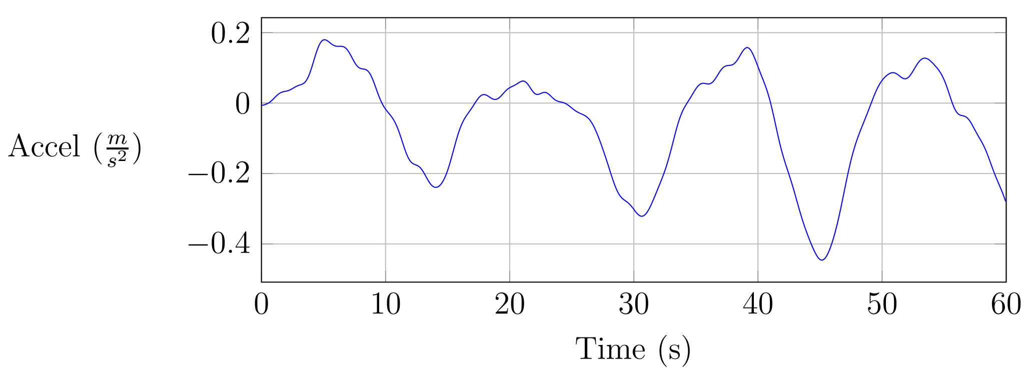

Figure 4.26: Ship acceleration used for multi-link validation simulations.

The 4BAR model was modified so that none of its joints were constrained, but it was also limited to motion in the X-Z plane. Its control system was also modified to match the cart-pendulum model's stiffness and damping inputs, and the gravity terms were removed to match the published model. The stiffness and damping coefficients used for both models have been included in Table 4.5.

Table 4.5: Stiffness (k_i) and damping (c_i) coefficients used in 4BAR – CARTIP validation tests.

Link Number (i)	1	2	3	4
k_i (N · m/rad)	512	256	128	32
c_i (N · m · s/rad)	128	32	16	4

The results of the test are shown in Figure 4.27. The data shown is for the fourth link, because its motion was the greatest. The other links all had very similar responses. The NRSME values for each link (angle comparison) are shown in Table 4.6.

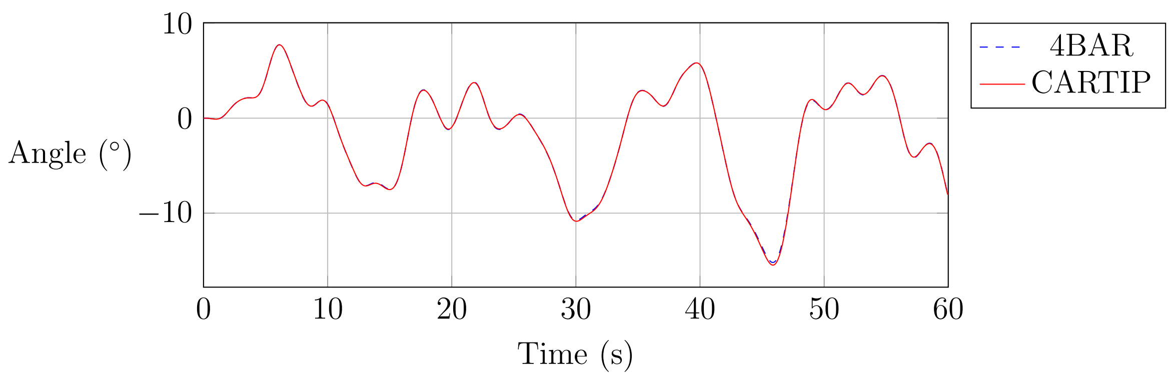

Figure 4.27: Multi-link validation test results for fourth (most outboard) link. NRMSE values range from 0.21% to 0.48%.

Table 4.6: NRMSE between inverted pendulum angles for the multi-link test which compares the 4BAR model to the cart – inverted pendulum model, and to the SIM3D SimMechanics model.

	x_3 (%)	x_6 (%)	x_9 (%)	x_{12} (%)
4BAR/CARTIP	0.2073	0.2745	0.3612	0.4778
4BAR/SIM3D	0.1216	0.1282	0.1354	0.1479

4.5.7 Validation of Multiple Links with Two-DOF Ship Motion and Gravity

In order to expand the multiple-link validation to include angular ship motions and gravitational forces, the Simulink model SIM3D was expanded to include these additional motions and forces. Figures 4.28 and 4.29 indicate the angles of the first and fourth links for the two models. Again, the model responses match closely. Table 4.7 contains all of the angular error results. The same control gains as presented in Table 4.5 were used, which, as shown in the figures, were not sufficient to maintain vertical upright posture.

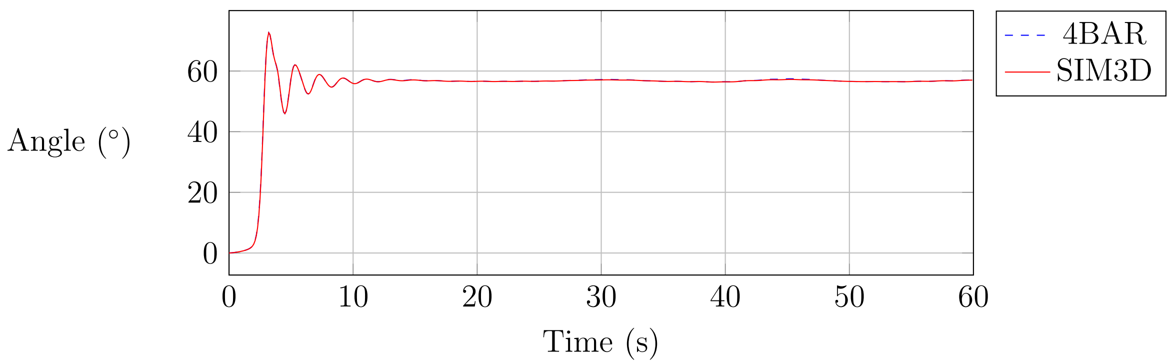

Figure 4.28: Multi-link validation Test 2 results for inboard link (Link 1). NRMSE 0.17%.

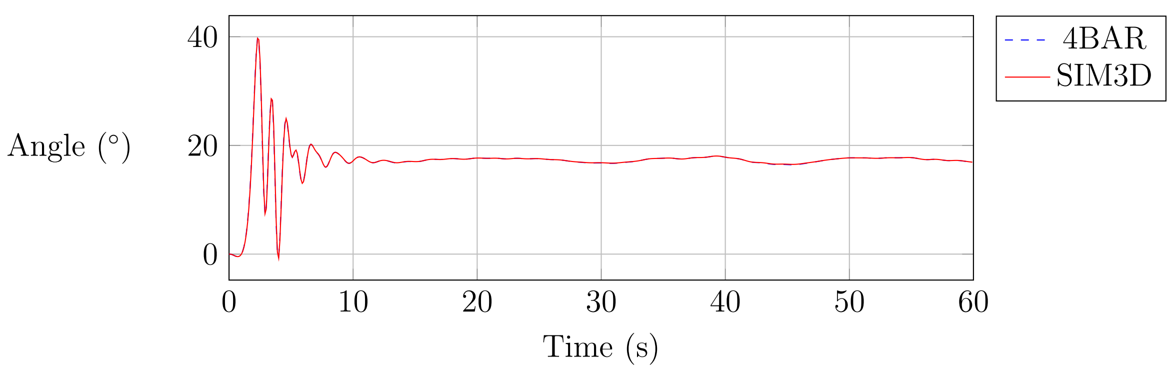

Figure 4.29: Multi-link validation test 2 results for outboard link (Link 4). NRMSE 0.30%.

Table 4.7: NRMSE between inverted pendulum angles for the multi-link test with two-DOF ship motion and gravity terms, comparing 4BAR model to SIM3D model.

	x_1 (%)	x_4 (%)	x_7 (%)	x_{10} (%)
4BAR/SIM3D	0.1662	0.1418	0.1905	0.3011

4.6 Chapter Summary

This chapter has presented the development of a spatial four-link inverted pendulum model that is intended to represent a human with motion at ankles, knees, hips, and neck. The equations of motion are derived using an automated method which allows the mathematics to be written in a simple matrix form. The sections in this chapter have also described how the equations can be modified to accommodate prescribed ship motions and joint constraints.

The model has been validated against a variety of simpler existing published models that encompass separate qualities of the model. In order to validate the interface forces and moments between the model and ship, it was validated against a model with no relative DOF between itself and the ship. In order to validate that the model could be controlled in a spatial environment the model was compared to a spatial inverted pendulum model. Finally, in order to validate the motion of multiple links in the model, it was compared to similar 2D models since a spatial multi-link model was not available.

The simulation results all show that the derived model matches the behaviour of the other validated models. Therefore the next chapter will focus on the development of a novel human-like control system for the model.

Chapter 5

Sensory-Based Control

5.1 Introduction

One objective of the control algorithm for the four-link inverted pendulum is to maintain stability of the inverted pendulum while it experiences six-DOF ship motion as recorded from the sea trial. The simplest solution for this would be to use the angles the inverted pendulum makes with respect to the inertial vertical as errors and increase the control gains until they are sufficiently large such that the ship's motions would not have a significant effect on the pendulum's position. This however would not fulfil the overall objective of the model, which is that the control moments and motions of the pendulum should be able to be correlated to the forces and motions that were measured during the sea trial for every subject, thereby behaving similarly to actual human balance control.

Figure 5.1 shows a visual overview of the design problem. It shows the control moments as they are applied to each link and the mass distribution between the links as a percentage of the total mass. Since the control moments are generated at the joints, they will contribute equal and opposite torques to the two links they are connected to. One can immediately see that care must be taken to balance the moments within each individual

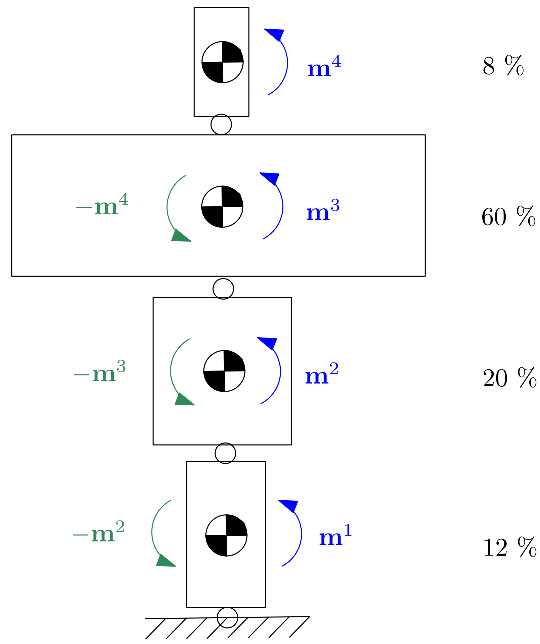

Figure 5.1: Diagram of four-link inverted pendulum which shows a sample of the relative mass of each link and how the control moments are applied to the system.

link such that the desired orientation is reached, and to coordinate the moments between links such that the very large torso mass does not cause the lower links to buckle.

The procedure that was used to determine control gains for each subject is presented in this chapter. It is divided into the following primary components.

1. Determination of subject kinematics from motion capture data.

2. Determination of subject dynamics from measured kinematics and inverted pendulum model.

3. Correlation of torque results from the inverse dynamics with experimental results.

4. Development of closed-loop and open-loop control strategies based on the total ship acceleration.

5. Evaluation of control system results with comparisons to the inverse dynamics and

experimental results.

5.2 Inverse Kinematics

The equations for calculating the inverse dynamics of the four-link inverted pendulum model were presented in Section 4.4.9. Using that formulation, one can take the motion capture data recorded during the sea trial, reduce it to the kinematics of a four-link inverted pendulum, and calculate the control moments that would be required to reproduce those kinematics. In theory, a control strategy which matches the results of the inverse dynamics calculations should be a good representation of human balance control.

The first step is to reduce the full-body motion capture data into equivalent motion of a four-link inverted pendulum. This was done by dividing body segments into four sections representing the lower legs, upper legs, trunk, and head. The specific assignments are shown in Table 5.1. The centre of mass, geometry, and inertia properties were calculated for each section and assigned to the corresponding link in the inverted pendulum model. Exact link dimensions were customized for each subject based on their motion capture data.

The next step was to determine the local Bryant angles of each link. The position of the centre of mass of link n in the rotated inverted pendulum coordinate frame (Frame 2) can be written as:

$$ {}^{2}\mathbf{p}^{n} = \sum_{k=3}^{n-1} {}^{k}\mathbf{q}^{k}\mathbf{R}^{k0} + {}^{n}\mathbf{r}^{n} \prod_{k=3}^{n} \mathbf{R}^{(k)(k-1)} \tag{5.1} $$

where $\mathbf{q}$ and $\mathbf{r}$ are consistent with the link dimensions defined in Figure 4.2. For the first link, where $k = 3$, the result would be:

$$ {}^{2}\mathbf{p}^{3} = {}^{3}\mathbf{r}^{3}\ \mathbf{R}^{32} \tag{5.2} $$

Table 5.1: Body segments with corresponding 4-link inverted pendulum segment.

Segment	Section
Left Foot	1
Right Foot	1
Left Lower Leg	1
Right Lower Leg	1
Left Upper Leg	2
Right Upper Leg	2
Trunk	3
Left Upper Arm	3
Right Upper Arm	3
Left Forearm	3
Right Forearm	3
Head	4

which can be simplified to:

$$\mathbf{a} = \mathbf{b}\ \mathbf{R}^{32} \tag{5.3}$$

The problem to solve then becomes: given $\mathbf{a}$ and $\mathbf{b}$, determine the X and Y Bryant angles (roll, θ_x, and pitch, θ_y) of the rotation matrix $\mathbf{R}^{32}$, if the Z Bryant angle (yaw) is zero. For $k = 4$ the result is:

$$\begin{gathered} {}^{2}\mathbf{p}^{4} = {}^{3}\mathbf{q}^{3}\ \mathbf{R}^{32} + {}^{4}\mathbf{r}^{4}\ \mathbf{R}^{43}\mathbf{R}^{32} \\ ({}^{2}\mathbf{p}^{4} - {}^{3}\mathbf{q}^{3}\ \mathbf{R}^{32})(\mathbf{R}^{32})^{T} = {}^{4}\mathbf{r}^{4}\ \mathbf{R}^{43} \\ \mathbf{a} = \mathbf{b}\ \mathbf{R}^{43} \end{gathered} \tag{5.4}$$

For $k = 5$ the result is:

$$({}^{2}\mathbf{p}^{5} - {}^{3}\mathbf{q}^{3}\ \mathbf{R}^{32} - {}^{4}\mathbf{q}^{4}\ \mathbf{R}^{42})(\mathbf{R}^{42})^{T} = {}^{5}\mathbf{r}^{5}\ \mathbf{R}^{54} \tag{5.5}$$

For $k = 6$ the result is:

$$({}^{2}\mathbf{p}^{6} - {}^{3}\mathbf{q}^{3}\ \mathbf{R}^{32} - {}^{4}\mathbf{q}^{4}\ \mathbf{R}^{42} - {}^{5}\mathbf{q}^{5}\ \mathbf{R}^{52})(\mathbf{R}^{52})^{T} = {}^{6}\mathbf{r}^{6}\ \mathbf{R}^{65} \tag{5.6}$$

The rotation matrix defined by the X and Y Bryant angles can be calculated as:

$$\begin{aligned} \mathbf{R}(\theta_x, \theta_y, 0) &= \begin{bmatrix} 1 & 0 & 0 \\ 0 & \cos(\theta_x) & -\sin(\theta_x) \\ 0 & \sin(\theta_x) & \cos(\theta_x) \end{bmatrix} \begin{bmatrix} \cos(\theta_y) & 0 & \sin(\theta_y) \\ 0 & 1 & 0 \\ -\sin(\theta_y) & 0 & \cos(\theta_y) \end{bmatrix} \\ &= \begin{bmatrix} \cos(\theta_y) & 0 & \sin(\theta_y) \\ \sin(\theta_x)\sin(\theta_y) & \cos(\theta_x) & -\sin(\theta_x)\cos(\theta_y) \\ -\cos(\theta_x)\sin(\theta_y) & \sin(\theta_x) & \cos(\theta_x)\cos(\theta_y) \end{bmatrix} \end{aligned} \tag{5.7}$$

The transformation from $\mathbf{b}$ to $\mathbf{a}$ can then be calculated as:

$$\begin{bmatrix} a_1 \\ a_2 \\ a_3 \end{bmatrix} = \begin{bmatrix} \cos(\theta_y) & 0 & \sin(\theta_y) \\ \sin(\theta_x)\sin(\theta_y) & \cos(\theta_x) & -\sin(\theta_x)\cos(\theta_y) \\ -\cos(\theta_x)\sin(\theta_y) & \sin(\theta_x) & \cos(\theta_x)\cos(\theta_y) \end{bmatrix} \begin{bmatrix} b_1 \\ b_2 \\ b_3 \end{bmatrix} \tag{5.8}$$

In order to solve for θ_x and θ_y, either the first and second, or first and third equations can be used. The first equation can be written as:

$$b_3 \sin(\theta_y) + b_1 \cos(\theta_y) = a_1 \tag{5.9}$$

To solve an equation of this form, the left side can be rewritten in the form of the identity:

$$A\sin\phi \pm B\cos\phi = \sqrt{A^2+B^2}\sin(\phi \pm \tan^{-1}\left(\frac{B}{A}\right)) = C \tag{5.10}$$

where $A = b_3$, $B = b_1$, and $C = a_1$. The value of θ_y can then be solved for as:

$$\theta_y = \sin^{-1}\left(\frac{a_1}{\sqrt{b_3^2+b_1^2}}\right) - \tan^{-1}\left(\frac{b_1}{b_3}\right) \tag{5.11}$$

If A is negative, the equation must be multiplied by (-1) to ensure compliance with the identity's signs. The other angle, θ_x, is calculated in a similar manner. The corresponding equation to solve from Equation 5.8 is:

$$b_1\sin(\theta_x)\sin(\theta_y) + b_2\cos(\theta_x) - b_3\sin(\theta_x)\cos(\theta_y) = a_2 \tag{5.12}$$

which can be rewritten in the form of the identity as:

$$[b_1\sin(\theta_y) - b_3\cos(\theta_y)]\sin(\theta_x) + b_2\cos(\theta_x) = a_2 \tag{5.13}$$

where $A = b_1\sin(\theta_y) - b_3\cos(\theta_y)$, $B = b_2$, and $C = a_2$. The value of θ_x can then be calculated as:

$$\theta_x = \sin^{-1}\left(\frac{a_2}{\sqrt{(b_1\sin(\theta_y)-b_3\cos(\theta_y))^2+b_2^2}}\right) - \tan^{-1}\left(\frac{b_2}{(b_1\sin(\theta_y)-b_3\cos(\theta_y))}\right) \tag{5.14}$$

As before, the terms in the equation that correspond to A in the identity must be positive for the identity to be valid. This condition must be checked for every calculation because of the negative term in A. Now that the Bryant angles for each link have been calculated, they can be differentiated to obtain Bryant angular velocities and angular accelerations. Low-pass data filtering was performed on the XYZ mass positions, on the angular velocities, and the angular accelerations in order to remove high-frequency noise from the data. The cutoff frequencies for each are shown in Table 5.2, which were determined using the procedure presented in Section 3.2.1.

Table 5.2: Optimum cutoff frequencies for mass section CoM, angular velocities, and angular accelerations sampled at 30 Hz.

	X	Y	Z	$\dot{\mathbf{x}}_1$	$\dot{\mathbf{x}}_2$	$\ddot{\mathbf{x}}_1$	$\ddot{\mathbf{x}}_2$
Link 1	0.8	0.8	1.3	1.3	1.5	1.6	1.8
Link 2	1.2	1.0	1.6	1.7	1.5	2.1	1.8
Link 3	1.5	0.9	1.3	1.5	1.7	1.5	1.7
Link 4	1.3	1.0	1.0	1.7	1.8	1.7	2.3

The last step is to convert the Bryant angular velocities and accelerations into the body-fixed generalized coordinate derivatives and second derivatives. Conveniently, for only two rotations these values are actually equivalent so no transformation is required.

One simplifying assumption made by the inverse kinematics calculations outlined above is that they assume that the CoM of each segment is located at ${}^k\mathbf{r}^k$ in each body, which may or may not be true, especially for the torso link. Including the distribution of mass within each link, however, is beyond the scope of this analysis.

5.3 Inverse Dynamics

An inverse dynamics analysis can be used to calculate what moments would need to be generated about each of the inverted pendulum's links in order to achieve the human body kinematics that were observed during the sea trial, in the form of a four-link inverted pendulum. The ship and inverted pendulum kinematics are input to the equations of motion and the solution is the array of moments defined in Equation 4.46. In theory, if a controller can be designed that produces exactly the same output for every combination of ship and body motions, for each person, that controller would be an accurate representation of how the human central nervous system maintains balance. In practice, however, this is a nontrivial task since human balance control is a very complex multiple-input multiple-output system of which much is still unknown.

The accuracy of the inverse dynamics calculations was assessed by comparing the ankle reaction moment of the model to the ground reaction moment measured by the insoles. These measures are independent in that the measurements made by the insoles were not affected by the motion capture measurement, but also do have some interdependency in that the scaling and moment arm of the reaction moment are both influenced by the motion capture data. Even with this dependency though, there is no guarantee that the two data sets should correlate. The vertical reaction force from the inverse dynamics was also compared to the total vertical force measured by the insoles in order to verify that the calculations had been performed correctly.

Figure 5.2 shows the results for a subject standing at $0°$ with respect to the ship centreline. The results for the reaction moments have had their mean value subtracted from them so that both data sets are centred about zero. While the results are not exactly the same, they are remarkably close in both magnitude and phase. The results from 49 different cases comprising $0°$, $45°$, and $90°$ cases are included in Appendix C.

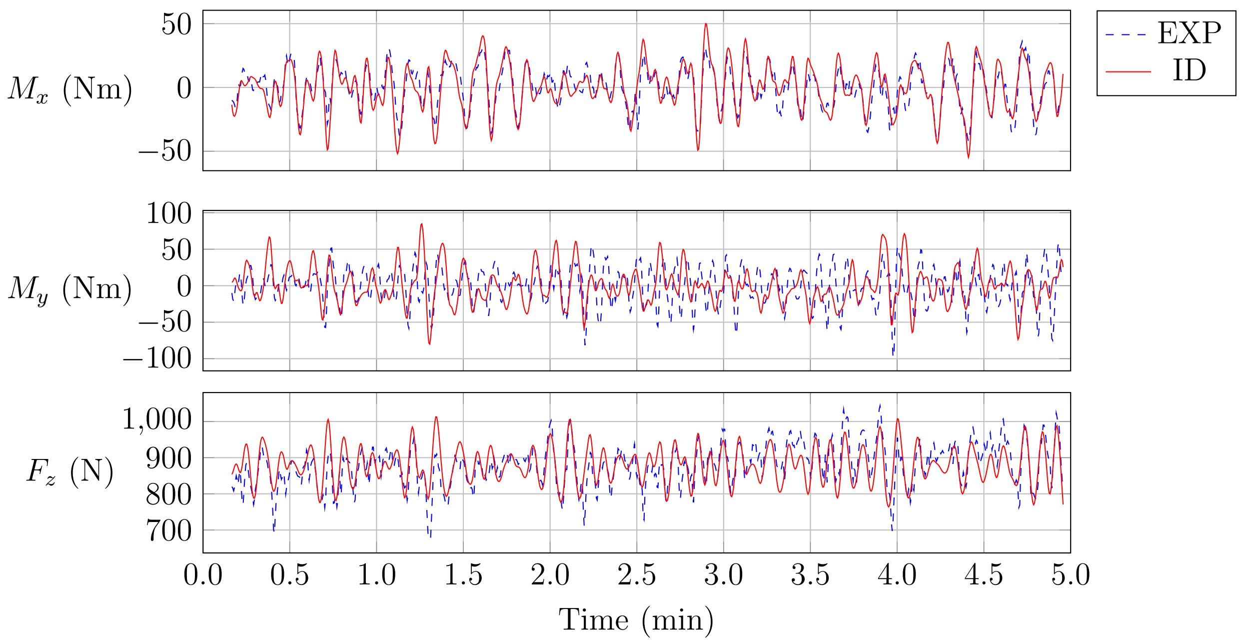

Figure 5.2: Comparison of reaction moments and forces between experimental data (EXP) and inverse dynamics (ID) simulation for a typical subject standing at 0°.

5.4 Sensory-Based Control

Maintenance of upright stance for humans relies on three major sources of sensory information. One is the pressure sensed under each of the feet, otherwise known as somatosensory information. This provides information on the location of the CoM within the BoS and indirectly provides knowledge of the direction of the total acceleration vector in the local human body frame. In normal standing conditions, humans can sense the direction of gravity and tend to align themselves with it. In shipboard environments, however, a person would only be able to estimate the total acceleration vector, which is the acceleration due to gravity plus the translational acceleration contribution from the ship's motions.

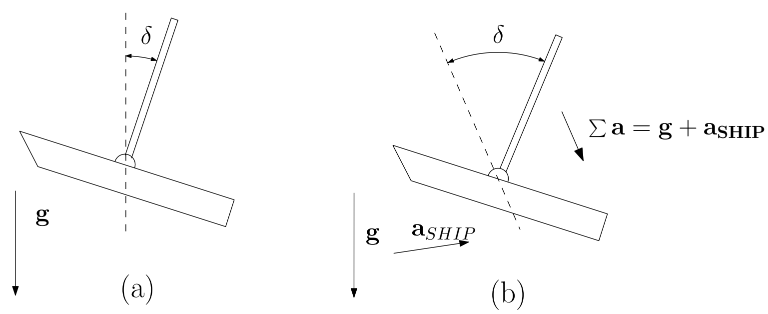

Figure 5.3: Acceleration due to: (a) gravity only and (b) gravity and ship motions.

While processing the motion capture data, it was observed that there were many cases where a vector from the subject's ankles to their CoM would align with the total acceleration vector, especially in the pitch direction. A sample of the pitch CoM angle compared to the pitch acceleration vector angle is shown in Figure 5.4. While this was not observed in the pitch direction in every case, and very rarely in the roll direction, as shown in another case in Figure 5.5, this apparent relationship provided a starting point for derivation of the control strategy.

The second source of human sensory information is the vestibular system, which provides two separate pieces of information: angular velocity of the head and the attitude

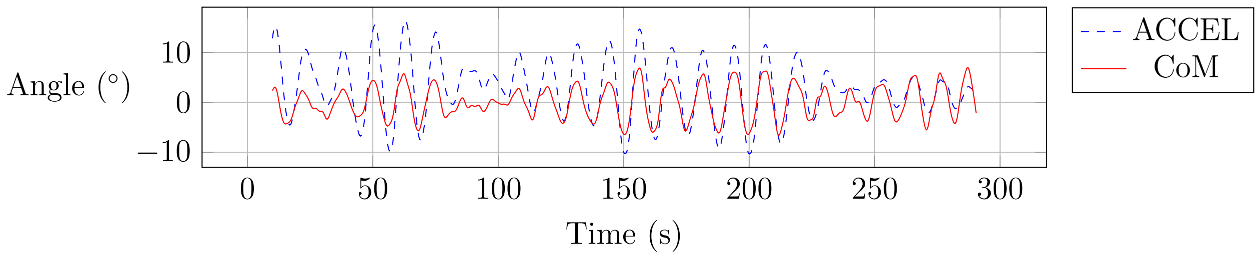

Figure 5.4: Sample case showing correlation between experimental CoM angle (CoM) and acceleration vector angle (ACCEL) for subject pitch angle.

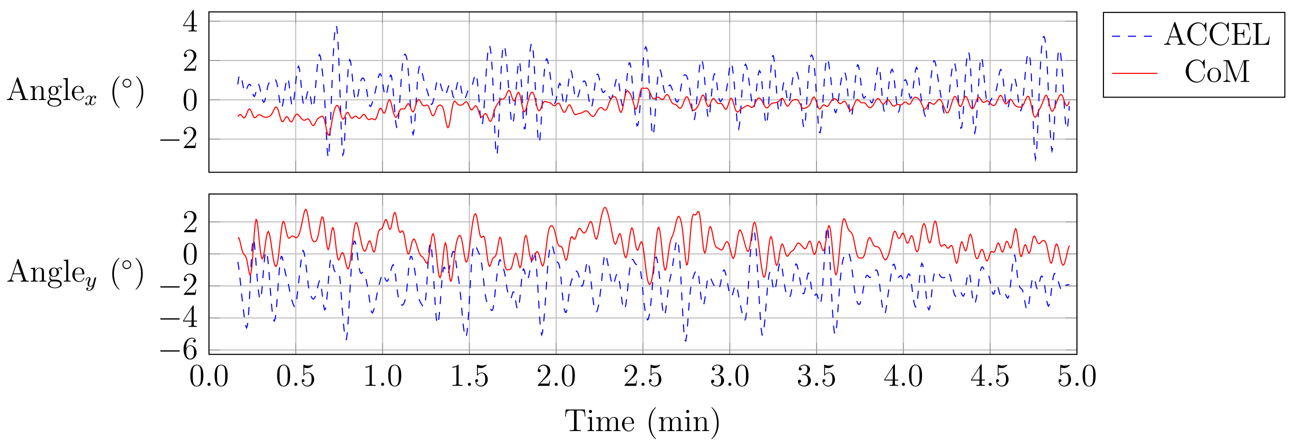

Figure 5.5: Comparison of motion capture CoM angle position vector (CoM) with translational acceleration vector (ACCEL) where correlation is limited.

of the head relative to the total gravity vector. The third source is vision, which provides information on head orientation with respect to the local environment. These two senses often work in conjunction as the vestibular senses are very responsive but prone to low-frequency noise, while the visual signals are very accurate but have much slower reaction time [60]. While it was not possible to use the sea trial data recordings of head kinematics as a basis for the controller, it is clear that they would provide information on body velocity and orientation with respect to the local ship frame.

A simple controller was devised based on the above premises. It consists of two basic objectives.

1. Minimize the angle between the body and the total acceleration vector.

2. Minimize the angular displacement between body segments.

A standard method for controlling a single-link inverted pendulum model in shipboard environments is to use full-state feedback control to maintain a vertical orientation with respect to inertial coordinates [9]. In such a case, it would be assumed that the magnitude of the restoring control moment would be directly proportional to the displacement of the centre of mass relative to the deck attachment point. While this is a logical expectation, it was found from the experimental data that the magnitude of the reaction moments did not consistently correlate to body displacements. It was found, however, that the moments correlated very well to the magnitude of the angles that the total acceleration vector made with respect to the ship. This makes sense from a sensory-control point of view. The experiments took place in an enclosed area within the ship such that participants did not have any indicators of the orientation of themselves with respect to the inertial coordinate system. In such a case, they were forced to do their best to (1) oppose the effects of the total acceleration, and (2) maintain upright stance within the ship frame in order to carry out their current tasks.

5.4.1 Acceleration Vector Angles

The IMU placed near the feet of the participants provided the total acceleration vector measured in the ship frame. In order to actuate an inverted pendulum to match the orientation of that vector, it is necessary to calculate the angle the vector makes with the vertical axis in the human-rotated frame. This can be done by calculating the projection of the vector onto three orthogonal axes as shown in Figure 5.6, where the axes can rotate with the human-rotated frame (Frame 2).

In Figure 5.6, the roll and pitch angles are measured with respect to the coordinate system of the IMU. In the model, these axes are replaced with human-fixed coordinate axes with the x axis ($\hat{\mathbf{u}}$) pointed to the person's front, the y axis ($\hat{\mathbf{v}}$) pointed to the person's

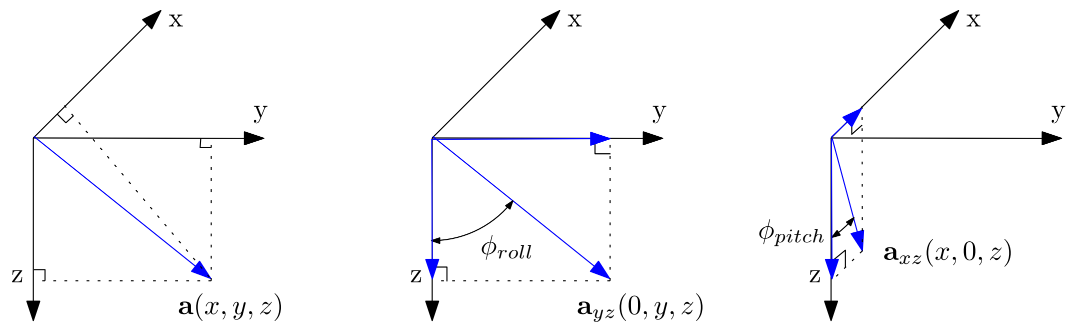

Figure 5.6: Absolute roll and pitch angles of the acceleration vector with respect to orthogonal coordinate axes.

left, and the z axis pointed up ($\hat{\mathbf{w}}$) in order for all angle measurements to be consistent and comparable. If $\hat{\mathbf{u}}$, $\hat{\mathbf{v}}$, and $\hat{\mathbf{w}}$ are unit vectors, then the absolute roll and pitch angles in the subject body frame can be calculated as:

$$\phi_{roll} = -\tan^{-1}\left(\frac{\mathbf{a}\cdot\hat{\mathbf{v}}}{\mathbf{a}\cdot\hat{\mathbf{w}}}\right) \tag{5.15}$$

$$\phi_{pitch} = \tan^{-1}\left(\frac{\mathbf{a}\cdot\hat{\mathbf{u}}}{\mathbf{a}\cdot\hat{\mathbf{w}}}\right) \tag{5.16}$$

5.4.2 Correlation of Moments with Accelerations

The torque outputs from the analysis in Chapter 3 and from the inverse dynamics calculations were compared to the angular motion of the CoM and acceleration angles. The correlations that showed the clearest trend suggested a linear relationship between the ground reaction torques from the experimental data and the acceleration angles calculated in the previous section. A graphed sample of this correlation is shown in Figure 5.7.

For each experimental trial, the slope of the line of best fit was calculated as well as Pearson's linear correlation coefficient. The coefficients were used as weights to average the slopes together to determine the average value for each subject. A computer algorithm was written which automatically calculated this average slope for all of the participants.

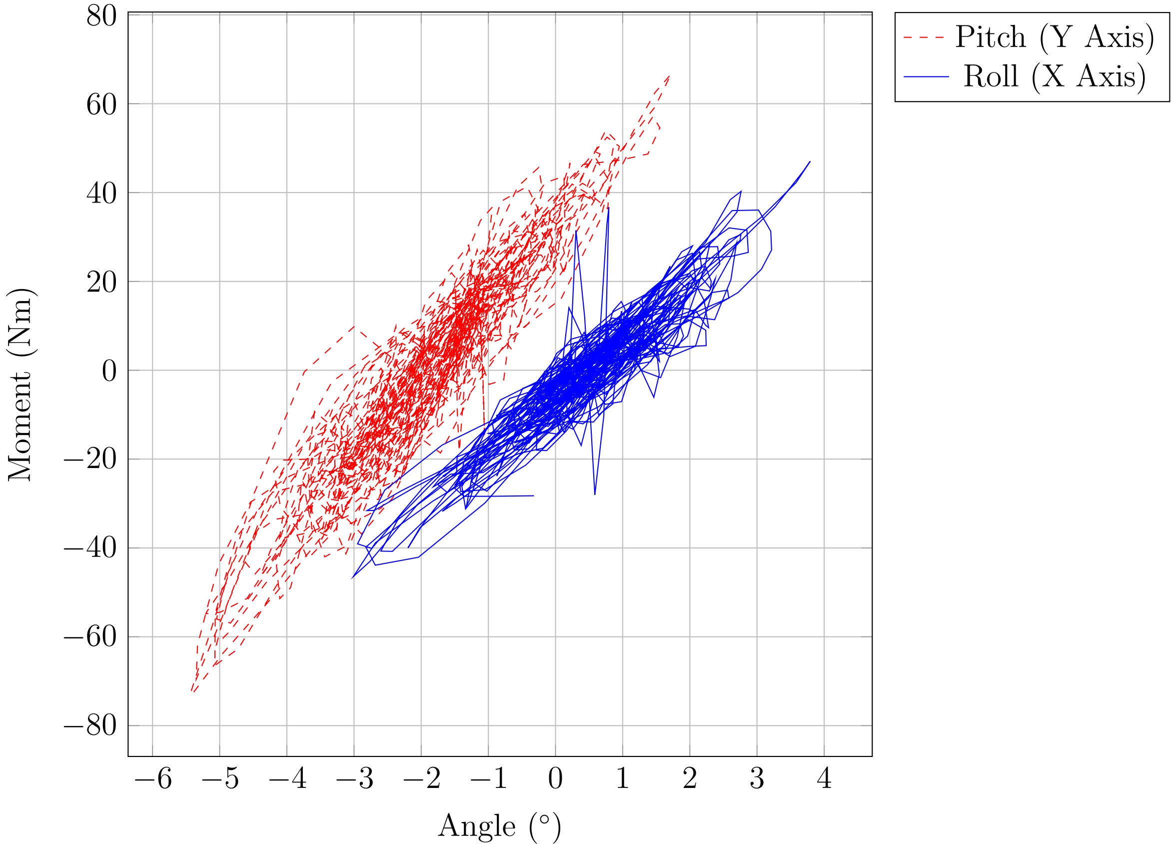

Figure 5.7: Near-linear relationship between acceleration angle and reaction moment.

A sample correlation calculation for one subject is shown in Table 5.3. Each slope measurement is multiplied by its correlation coefficient and divided by the sum of all of the correlation coefficients, in order to arrive at the weighted slope value. For example, in the top row of Table 5.3, $1042.33 \times 0.95 / 5.07 = 195.25$. All of the weighted slope values are then summed together to arrive at 952.76.

Table 5.3: Sample results for the calculation of the weighted average of the linear regression slope coefficients.

	Slope (Nm/rad)	Correlation	Weighted Slope (N·m/rad)
	1042.33	0.95	195.25
	898.20	0.94	167.16
	866.26	0.96	164.43
	1011.80	0.93	186.00
	1001.82	0.35	68.26
	928.92	0.94	171.66
Total		5.07	952.76

5.5 Controller Design

Next, a controller was designed which used the averaged linear regression coefficients calculated in the previous section as the basis for its feedback gains. The controller was designed with two objectives for how the system would be controlled.

1. The ankle joint would be controlled in order to follow the angles of the acceleration vector.

2. The knee, hip, and neck joints would be controlled to minimize their relative displacements.

While working toward a stable control system based on state feedback it was found that with just those two objectives, the inverted pendulum swayed much more than a person would, to the point where it even fell over in some cases. Therefore, additional control moment components were added to the knee, hip, and neck joints, based on the ankle moment that was previously calculated. The basis for adding these supplemental moment components was comprised of two parts.

1. Only generating moments at the knees, hips, and neck based on feedback errors did not provide a fast enough response to changing ship dynamics.

2. If a person were attempting to move their body to a specific orientation, it would most likely be a coordinated effort distributed among multiple joints.

In order to determine how this additional torque should be distributed among each of the links, the results of the inverse dynamics calculations were used. As shown in Figure 5.8, these results showed that there was a near-linear relationship between the control moments of different joints.

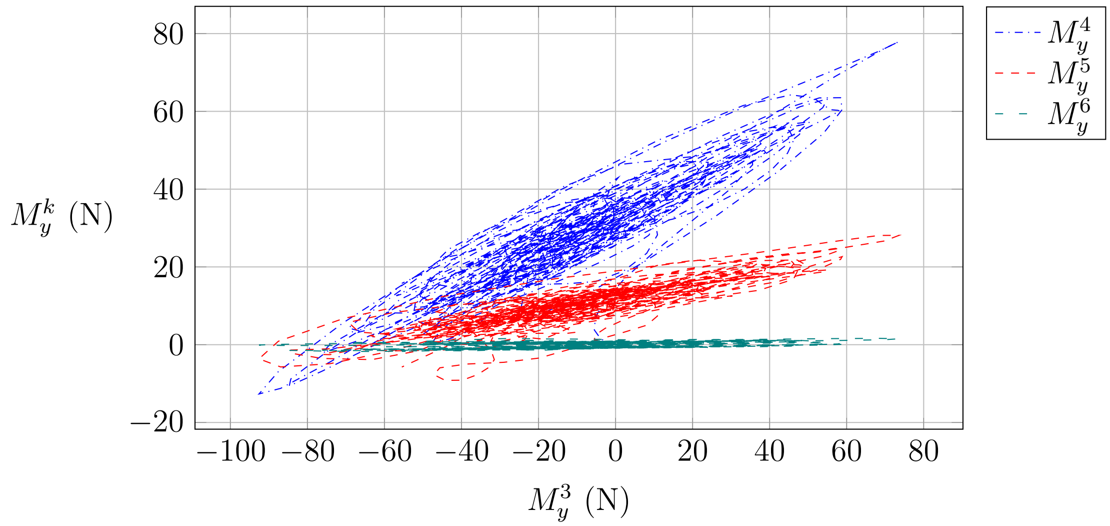

Figure 5.8: Knee, hip, and neck pitch moments as a function of ankle pitch moments from the inverse dynamics calculations.

On average, this analysis indicated that the knee joint torque was typically 30-50% of the ankle joint; the hip joint torque was typically 20–30%; and the neck joint torque was typically 1%. When these magnitudes were applied to the control system, however, it was found that they were typically not of large enough magnitude to produce a difference in the simulation results.

A second method which used the relative inertia values between the links resulted in a much better result. It was developed as follows. Referring to Figure 5.1 and neglecting the angular velocity terms, the angular equations of motion for the axis coming out of the page can be written in terms of the moments as:

$$\begin{aligned} m^1 - m^2 &= I^1\alpha^1 \\ m^2 - m^3 &= I^2\alpha^2 \\ m^3 - m^4 &= I^3\alpha^3 \\ m^4 &= I^4\alpha^4 \end{aligned} \tag{5.17}$$

For all of the inverted pendulum links to move as if they were a single link, the angular accelerations would have to be equal. Back-substitution of the moment terms and simplification of the resulting equations would then result in:

$$\begin{aligned} m^4 &= I^4\alpha \\ m^3 &= (I^3 + I^4)\alpha \\ m^2 &= (I^2 + I^3 + I^4)\alpha \\ m^1 &= (I^1 + I^2 + I^3 + I^4)\alpha \end{aligned} \tag{5.18}$$

Dividing each equation by the last one would then provide a relationship between moments m^2, m^3, m^4 and m^1:

$$m^2 = \frac{(I^2 + I^3 + I^4)}{(I^1 + I^2 + I^3 + I^4)} m^1 \tag{5.19}$$

$$m^3 = \frac{(I^3 + I^4)}{(I^1 + I^2 + I^3 + I^4)} m^1 \tag{5.20}$$

$$m^4 = \frac{(I^4)}{(I^1 + I^2 + I^3 + I^4)} m^1 \tag{5.21}$$

This method resulted in approximately 90% for the knee joint, 80% for the hip joint, and 4% for the head joint. This result greatly reduced the sway motions of the inverted pendulum, except it was found that the head joint tended to sway too much, and frequently caused the model to become unstable and fall over. Therefore, the value for the neck joint was raised to 10% in order to maintain stability based on observation of simulation results. These final results are defined as **h** in the control equations that are presented later in this section, where:

$$\mathbf{h} = [0 \;\; 0.88 \;\; 0.8 \;\; 0.1]^T \tag{5.22}$$

This resulted in a stable control system that consisted of two components.

1. A component focused on aligning the inverted pendulum's CoM with the acceleration vector by applying closed-loop control torques to the ankle joint and open-loop torques to the other joints.

2. A closed-loop component focused on minimizing the relative displacement and velocity between body segments.

At first the inverted pendulum consisted of twelve controllable degrees of freedom. It was determined that the yaw did not provide a meaningful contribution to the simulation so it was decided to constrain these degrees of freedom. Additionally, while tuning the control gains, it was not possible to obtain satisfactory control performance on both pitch and roll directions with a roll DOF at the knee joint. Therefore it was decided to constrain this DOF as well. It is believed that this is consistent with the objective to match the motion of a human since the lateral stability of an inverted pendulum does not accurately match the stability of a human with two legs. The single DOF remaining on the knee joint still provides the ability to have relative translational motion between the ankle and hips; thus the original objective of including a knee joint is maintained.

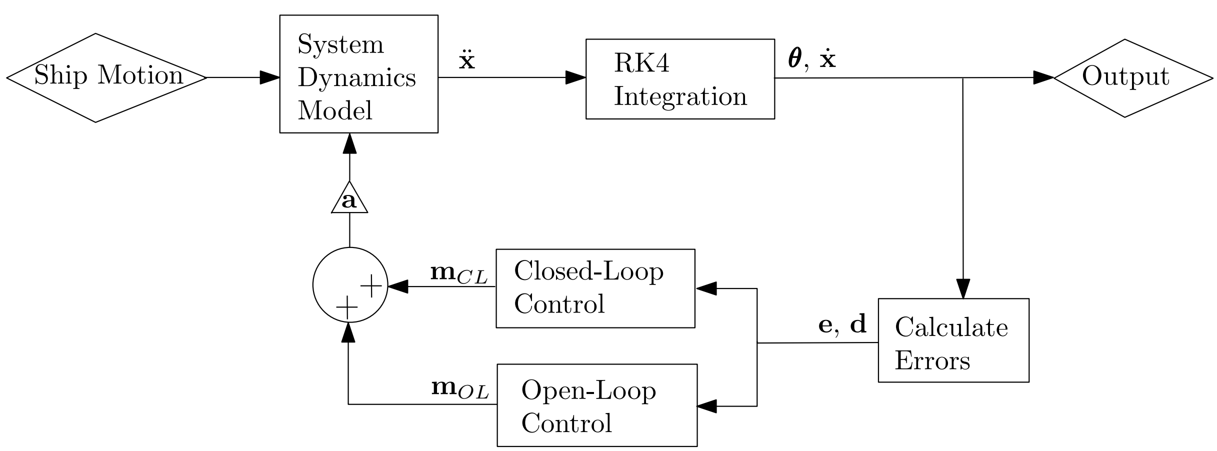

Figure 5.9: Diagram of the control loop used for the four-link inverted pendulum simulation.

Figure 5.9 shows the final overall control loop. The inputs to the error calculation algorithm are the Bryant angles and generalized coordinate derivatives, $\boldsymbol{\theta}$ and $\dot{\mathbf{x}}$ respectively. The outputs of these calculations include the proportional errors calculated as:

$$\mathbf{e} = \begin{bmatrix} -\tan^{-1}(\,{}^{2}r_2^m/\,{}^{2}r_3^m) \\ \tan^{-1}(\,{}^{2}r_1^m/\,{}^{2}r_3^m) \\ {}^{4}\theta_2^4 \\ {}^{5}\theta_1^5 \\ {}^{5}\theta_2^5 \\ {}^{6}\theta_1^6 \\ {}^{6}\theta_2^6 \end{bmatrix} \tag{5.23}$$

where the first two are the angles that the CoM makes with the ship frame and the other five are the state angles. The error rates are the absolute angular velocity of each link in the ship frame. Since coordinate transformations are required, it is simpler to calculate the values for all DOF as:

$$\mathbf{d}_{(12DOF)} = \begin{bmatrix} \dot{\mathbf{x}}^3\ \mathbf{R}^{32} \\ \dot{\mathbf{x}}^4\ \mathbf{R}^{42} + \dot{\mathbf{x}}^3\ \mathbf{R}^{32} \\ \dot{\mathbf{x}}^5\ \mathbf{R}^{52} + \dot{\mathbf{x}}^4\ \mathbf{R}^{42} + \dot{\mathbf{x}}^3\ \mathbf{R}^{32} \\ \dot{\mathbf{x}}^6\ \mathbf{R}^{62} + \dot{\mathbf{x}}^5\ \mathbf{R}^{52} + \dot{\mathbf{x}}^4\ \mathbf{R}^{42} + \dot{\mathbf{x}}^3\ \mathbf{R}^{32} \end{bmatrix} \tag{5.24}$$

which is then reduced to include just the DOF that are being controlled:

$$\mathbf{d}_{(7DOF)} = \begin{bmatrix} \mathbf{d}_{(12DOF)}(1) \\ \mathbf{d}_{(12DOF)}(2) \\ \mathbf{d}_{(12DOF)}(5) \\ \mathbf{d}_{(12DOF)}(7) \\ \mathbf{d}_{(12DOF)}(8) \\ \mathbf{d}_{(12DOF)}(10) \\ \mathbf{d}_{(12DOF)}(11) \end{bmatrix} \tag{5.25}$$

The open-loop controller provides control moments for bodies 4, 5, and 6 as a function of the errors for body 3:

$$\mathbf{m}_{OL} = - \begin{bmatrix} 0 \\ 0 \\ k_2 h_2 e_2 \\ k_1 h_3 e_1 \\ k_2 h_3 e_2 \\ k_1 h_4 e_1 \\ k_2 h_4 e_2 \end{bmatrix} \tag{5.26}$$

and the closed-loop control moments can be defined as:

$$\mathbf{m}_{CL} = -\begin{bmatrix} k_1 h_1 e_1 \\ k_2 h_1 e_2 \\ k_2 h_2 e_3 \\ k_1 h_3 e_4 \\ k_2 h_3 e_5 \\ k_1 h_4 e_6 \\ k_2 h_4 e_7 \end{bmatrix} - 0.15 \begin{bmatrix} k_1 h_1 d_1 \\ k_2 h_1 d_2 \\ k_2 h_2 d_3 \\ k_1 h_3 d_4 \\ k_2 h_3 d_5 \\ k_1 h_4 d_6 \\ k_2 h_4 d_7 \end{bmatrix} \tag{5.27}$$

where k_1 and k_2 are the subject-personalized roll and pitch control gains calculated in the previous section. The selection of error rate gains was based on published work on designing a control system for a two-dimensional three-link inverted pendulum model [61]. While in that case a scaling factor of 0.30 was used, it was found for this model that 0.15 was the largest value that could be used without compromising the stability of the controller.

The block labelled **a** in Figure 5.9 is an array of scaling coefficients for each of the control outputs that are used to tune the stability of the controller, since the relative magnitudes of the moments acting on each link can have a significant effect on the stability of the inverted pendulum model.

Note that $\mathbf{e}_1$ and $\mathbf{e}_2$ are only the CoM error and not the difference between those angles and the total acceleration vector. This difference was in fact the error used when the controller was first derived. Interestingly, it was found that the controller followed the acceleration angles more closely when their values were not included as part of the controller.

5.6 Results

The success of the control algorithm was evaluated using two metrics: how well the CoM angle of the inverted pendulum model matched the angles of the total acceleration vector and how well the reaction moment at the ankle matched between the model simulations, inverse dynamics calculations, and experimental results.

Figure 5.10 shows sample results comparing the first metric. The results are very close, with the results in the roll direction matching more closely, which was a common result for the 0° case.

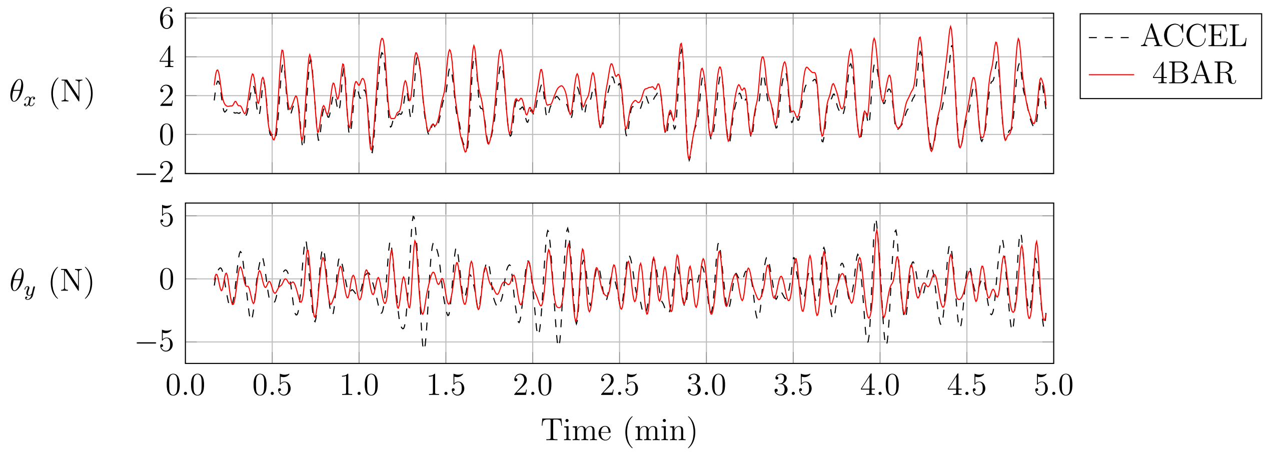

Figure 5.10: Comparison of experimental acceleration angles (ACCEL) and simulation CoM angles (4BAR) for a subject standing at 0°.

Figure 5.11 shows the results comparing the ground reaction moment between the simulation and experimental data. In this case, the roll moment is a better match than the pitch moment. In almost every case the magnitudes of the simulation results were greater than the experimental results. Figure 5.12 shows the results comparing the inverse dynamics moments to the simulation results. The inverse dynamics results were typically greater than the experimental results, but less than those from the simulation. The results from 49 trials that were analyzed are included in Appendix C.

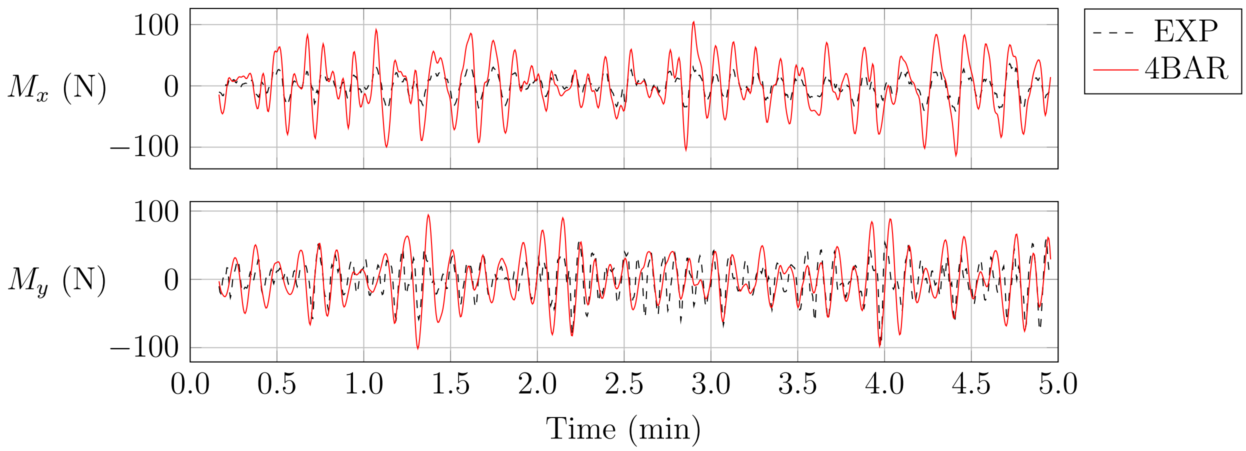

Figure 5.11: Comparison of human-ship moments between experimental data (EXP) and simulation data (4BAR) for subject standing at 0°.

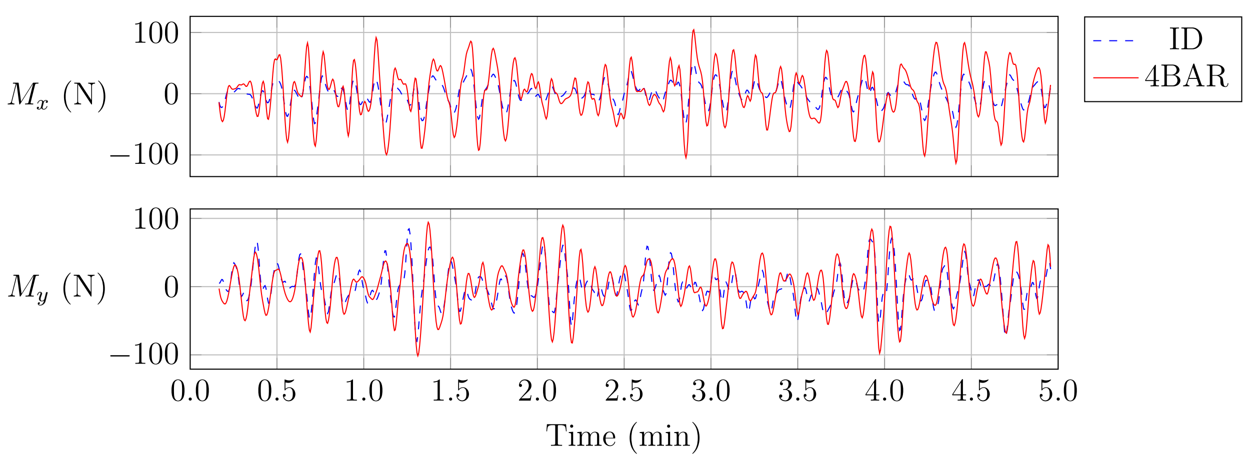

Figure 5.12: Comparison of human-ship moments between inverse dynamics results (ID) and simulation data (4BAR) for a subject standing at 0°.

5.7 Stability

Stability of the controller was analyzed by numerically linearizing the system at half-second intervals of each simulation and calculating the corresponding eigenvalues of the linearized system.

The goal of the linearization algorithm is to determine an equivalent linear system at specific operating points $(\mathbf{x_p}, \dot{\mathbf{x}}_\mathbf{p})$ of the simulation in the form of:

$$\mathbf{A}\ddot{\mathbf{x}} + \mathbf{C}\dot{\mathbf{x}} + \mathbf{K}\boldsymbol{\theta} = \boldsymbol{f}(\boldsymbol{\theta}, \dot{\mathbf{x}}) \tag{5.28}$$

where $\mathbf{A}$, $\mathbf{C}$, and $\mathbf{K}$ are not functions of the system's state as they are in the full model. The first step is to calculate $\mathbf{A}$ and $\boldsymbol{f}$ at the point of interest which can be done using Equation 4.40 and Equation 4.43 (restated here for convenience):

$$\mathbf{A}_p = \mathbf{A}(\mathbf{x_p}) = \sum^{k} \left[m^k \mathbf{V}_Q^k (\mathbf{V}_Q^k)^T + \mathbf{W}^k \mathbf{I}^{k0} (\mathbf{W}^k)^T \right] \tag{5.29}$$

$$\boldsymbol{f}_p = \boldsymbol{f}(\mathbf{x_p}, \dot{\mathbf{x}}_\mathbf{p}) = \sum^{k} \left[\mathbf{V}_Q^k m^k \mathbf{g} + \mathbf{W}^k (\mathbf{m}^k - \mathbf{m}^{k+1}) \right] \tag{5.30}$$

The next step is to determine $\mathbf{K}$, which is done by assuming that $\ddot{\mathbf{x}}$ and $\dot{\mathbf{x}}$ are zero at the current operating point. This would give:

$$\mathbf{K}\mathbf{x} = \boldsymbol{f} \tag{5.31}$$

Next, for each entry in $\mathbf{x}$, let $x_i' = x_i + \epsilon$, and substitute to obtain:

$$\mathbf{K}\ \mathbf{x}' = \boldsymbol{f}(\mathrm{x}', \dot{\mathbf{x}}_\mathbf{p}) = \boldsymbol{f}' \tag{5.32}$$

The i^{th} column in $\mathbf{K}$ can then be calculated as $(\boldsymbol{f}' - \boldsymbol{f}_{\boldsymbol{p}})/\epsilon$.

Table 5.4: Sample eigenvalues calculated over stable simulation.

Mean	RMS	Min		Max	
Re	Im	Re	Im	Re	Im
-264	0	-266	0	-257	0
-33.1	0	-48.8	0	-3.12	0
-48.7	0	-91.8	0	-46.7	0
-61.3	0	-91.8	0	-3.69	0
-86.4	0	-87.5	0	-6.79	0
-6.49	0	-6.79	0	-5.22	0
-35.7	0	-91.7	0	-3.65	0
-19.8	0	-47.4	0	-3.03	0
-4.06	-0.443	-6.05	-2.64	-1.11	2.66
-4.43	0.443	-6.05	-2.66	-1.11	2.64
-1.10	-2.78	-1.16	-3.02	-0.989	3.00
-1.18	2.79	-6.63	-2.91	-0.979	2.92
-1.26	-2.72	-6.63	-2.92	-1.11	2.92
-1.02	2.85	-1.05	-3.00	-0.979	3.02

The same process is used to estimate $\mathbf{C}$ from:

$$\mathbf{C}\ \dot{\mathbf{x}}' = \boldsymbol{f}(\mathbf{x_p}, \dot{\mathbf{x}}') = \boldsymbol{f}'' \tag{5.33}$$

The characteristic equation can then be obtained from:

$$\det\left(\begin{bmatrix} \mathbf{O}_{(7x7)} & \mathbf{I}_{(7x7)} \\ \mathbf{A}^{-1}\ \mathbf{K} & \mathbf{A}^{-1}\ \mathbf{C} \end{bmatrix} - \lambda \mathbf{I}_{(14\times 14)}\right) = 0 \tag{5.34}$$

Sample results for a 0° case are shown in Table 5.4. In the second column the imaginary parts are provided as a RMS value rather than a mean because they oscillate about zero. They have been multiplied by the sign of their mean values in order to indicate which ones are matching pairs. All of the real number parts of the eigenvalues are negative and therefore stable through the entire simulation.

In order to establish that the stability analysis was in fact valid, the results of a simulation performed with an unstable controller were analyzed. The results of the simulation are shown in Figure 5.13. In the figure it can be seen that shortly after 18 seconds have elapsed, the inverted pendulum loses its upright stance and begins to rotate. It can be seen in the second graph that one eigenvalue is consistently slightly positive (unstable) throughout the simulation, and that many of the others also exceed zero just before the inverted pendulum loses stability.

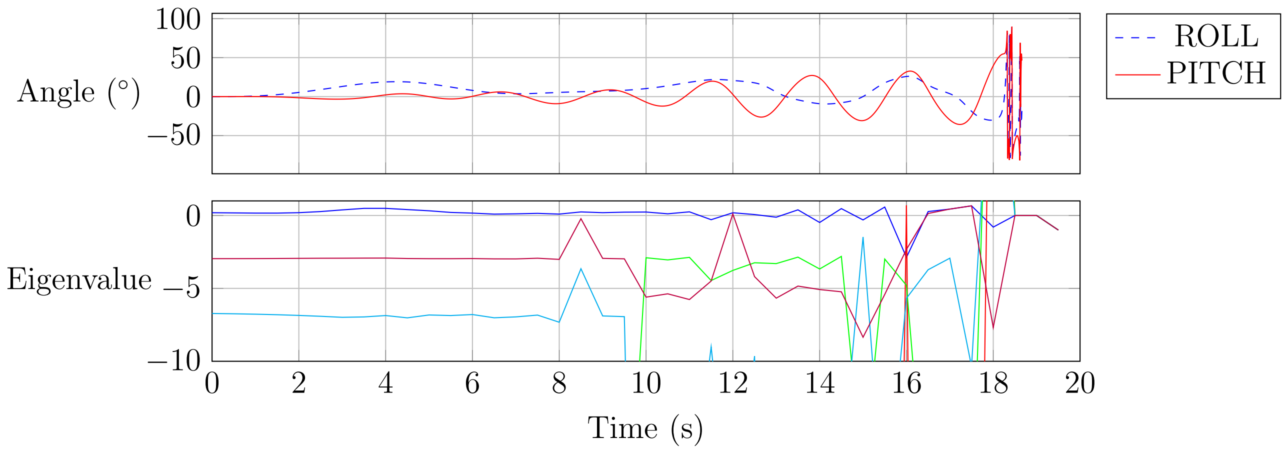

Figure 5.13: Sample simulation results with unstable controller. (Note that only eigenvalues contributing to the instability are shown.)

5.8 Overall Results

Model simulation, inverse dynamics, and experimental results were compiled for 49 test cases divided over the three standing orientations relative to the ship centreline. Data sets were compared by calculating the Pearson correlation coefficient between them. Figures 5.14 and 5.15 compare the ground reaction moments, first between the experimental and inverse dynamics, and second between the experimental and simulated results. Each figure shows the results for roll and pitch angles separately, those angles being measured with respect to the person's body frame. The data points have been spread about their X-axis values (direction) for visualization and interpretation purposes only. Figure 5.14 provides a measure of how well the full body kinematics can be reduced to a multi-link inverted pendulum's kinematics and still reflect the same required body control forces.

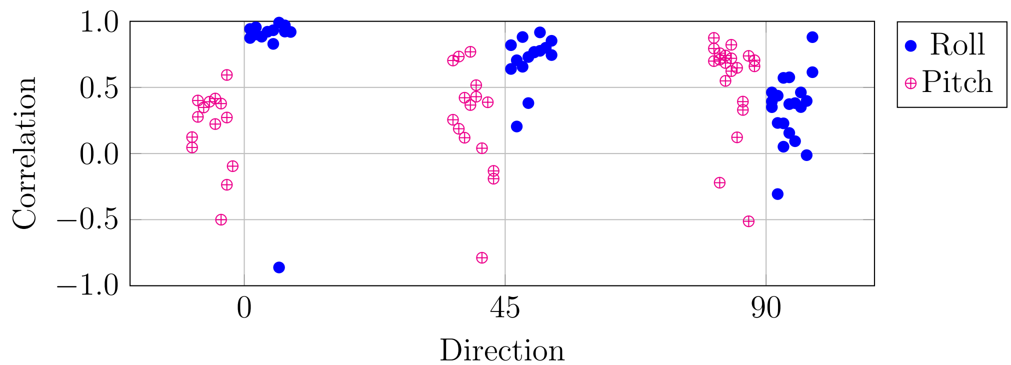

Figure 5.14: Correlations for comparing experimental moments to inverse dynamics moments.

Both figures show that there are cases when the data sets match very well and cases where they do not match very well. The general trend is that roll angle tends to match better with the subject standing at 0° and pitch angle tends to match better at 90°. The fact that many cases do not match at all is not unexpected since both cases are simplifications of the actual mechanics, and there is the possibility of error in the experimental results. The important aspect is that there are many cases where the results do correlate

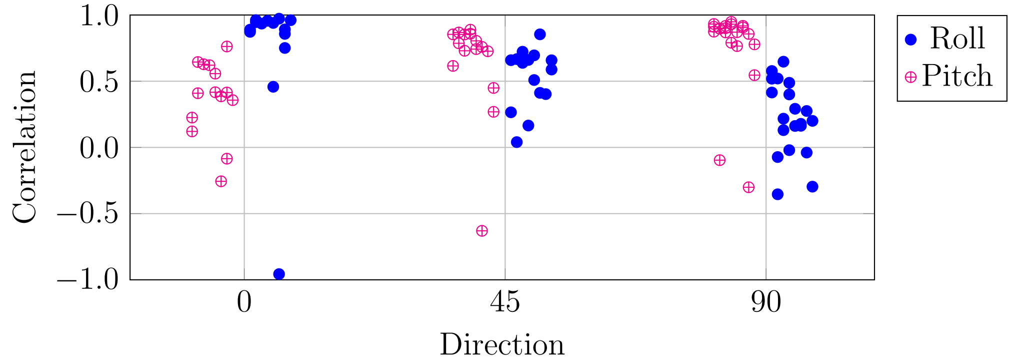

Figure 5.15: Correlations for comparing experimental moments to simulation moments.

very well.

The next two figures focus on the evaluation of the control algorithm. Figure 5.16 shows the correlation results between the simulation CoM angle and the experimental total acceleration angle. One of the goals of the controller was to match these two angles. Overall, the results were very good. The correlation results are over 0.5 for the majority of cases. The same general trend that was observed previously is also visible here–that the model tends to match best for roll at 0° and for pitch at 90°. Another observation is that overall pitch angle tended to match better than roll angle. This is not surprising as the geometrical simplification of the inverted pendulum model compared to a human is much greater in the roll direction. That said, the fact that roll angle actually matches very well at zero degrees is very interesting and will be further investigated in the next section.

Figure 5.17 evaluates how well the derived controller matches the 'ideal' controls calculated by the inverse dynamics model. In general, the results are very good with the majority of the correlations being 0.8 or greater. This is an important result, as there was no guarantee that the quasi-linear behaviour of the derived controller would be able to match the nonlinear behaviour of the inverse dynamics moments. The results for the other three joints are shown in Figure 5.18. The general result is that the higher up the inverted pendulum the joint is, the less well the results match.

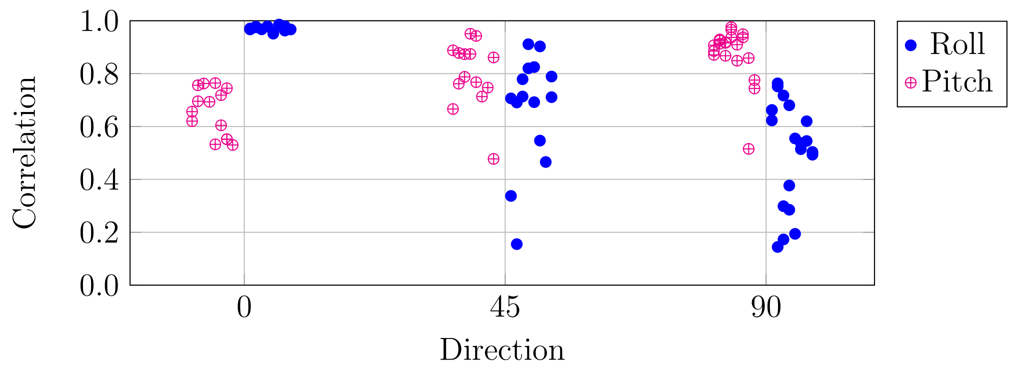

Figure 5.16: Correlations for comparing simulation CoM angles to acceleration angles.

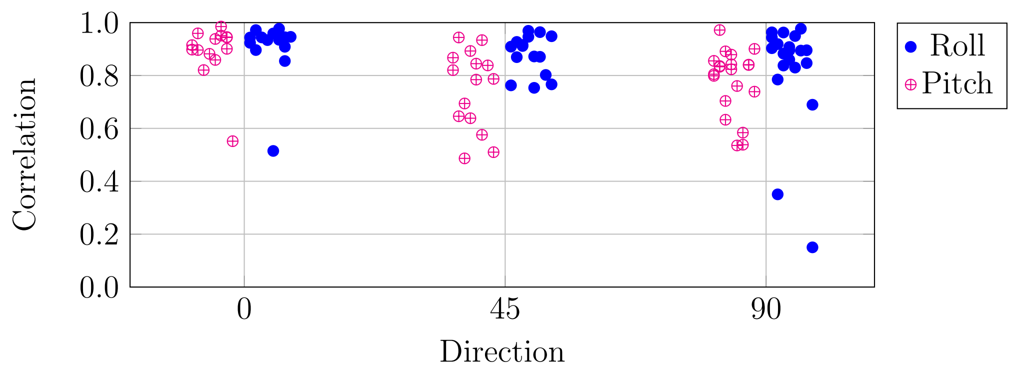

Figure 5.17: Correlations for comparing simulation moments to inverse kinematics of the ankle joint.

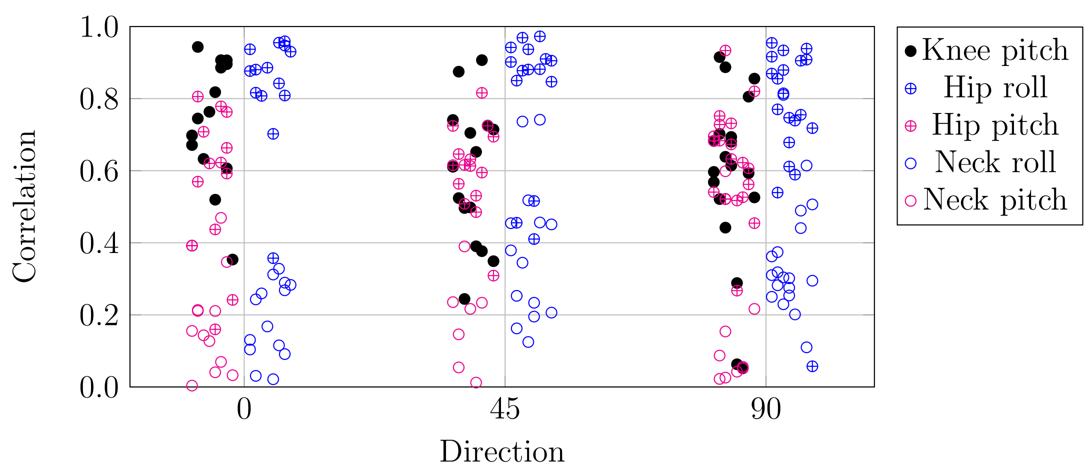

Figure 5.18: Correlations for comparing inverse dynamics moments of the ankle joint to all of the other joints.

Inspection of the simulation results shows an interesting trend: when the subject was oriented at 90°, the simulation CoM angle matched best with the pitch angle of the acceleration vector; but when the subject was rotated to 0°, the subject would best match with the roll angle of the acceleration vector. This indicated that the performance of the model, in comparing it to how well it tracked the acceleration vector, was not related to strictly pitch performance or roll performance. This was an interesting result because the model has different DOF in each direction since the knee is not permitted to roll. This result suggested that the performance of the model was based on the ship motions rather than the orientation of the subject. Metrics were derived to compare this result based on:

- ship angular motion;
- correlation of the acceleration vector with the simulation CoM; and
- subject angular motion.

The angular ship and subject motions were evaluated by calculating RMS absolute roll and pitch angles over each experimental trial, and then scaled by their ranges. The correlation results were the roll and pitch correlations shown in Figure 5.10. All three values were plotted with roll on the X axis and pitch on the Y axis, and the angular differences between them were compared. Sample results for three cases are shown in Figure 5.19, and the results for all of the cases are included in Appendix C.

In theory, if the performance of the model is a function of the magnitude of the ship motions, then the model performance correlations should match with the magnitudes of the ship motion. The third value was calculated to see if the experimental results showed the same general behaviour.

Over the results of 47 experimental trials the results did show the expected trend. Two outliers were removed because their results were an order of magnitude greater than all of the other results. The average angle difference between the ship angular motion and

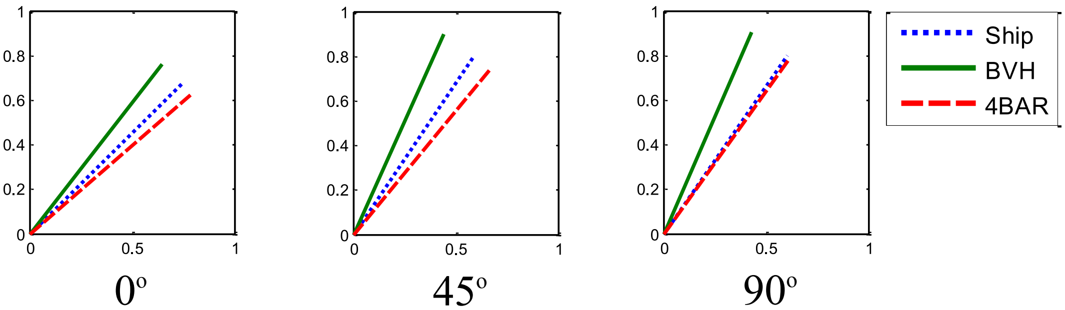

Figure 5.19: Graphs which compare simulation correlations with ship and subject angular motion magnitudes.

the simulation correlation was 8.85° with a standard deviation of 6.03°. Comparing the subject angular motion to the ship angular motion did not match quite as closely. In that case, the average difference was 10.65° with a standard deviation of 7.69°.

Chapter 6

Discussion and Conclusion

6.1 Overview

The objective of this thesis was to develop a postural stability model of a human standing at various orientations in a shipboard environment. The model was then to be tuned with experimental data gathered in a heavy-weather sea trial. This objective has been accomplished.

The postural stability model is a four-link inverted pendulum which allows for representative motion of ankles, knees, hips, and neck. The equations of motion were derived using a method that procedurally generates the equations based on the geometry of the system and the transformations between the coordinate systems of the individual links. The method also allows all of the mathematics to be written in two-dimensional array/matrix form. The model can be simulated under any six-degree-of-freedom ship motions and oriented at any angle with respect to the ship centreline. The model's equations were validated by comparing its simulation results with a variety of simpler published models that were simulated under identical conditions.

In order to design a control system for the model which would behave similarly to a person in actual sea environments, human postural stability experiments were carried out as a secondary experiment on board the Quest Q-348 heavy-weather sea trial. Over a period of eight days, thirteen participants took part in experiments where they were required to complete a cognitive task while standing at various angles with respect to the ship centreline. A variety of data acquisition technologies were used which included full-body motion capture, foot pressure measurements, and inertial motion measurements.

The experimental data was post-processed in a variety of ways to derive useful information from it. The final result was a detailed analysis of the motion of each subject's centre of mass and centre of force within their base of support. While few motion induced interruptions were observed during the sea trial, for those that were observed, various stability parameters were analyzed at the times of occurrences. Unfortunately, no clear trends were derived from the results.

From the experimental data of all of the participants, it was observed that in many cases the centre of mass position correlated with the direction of the total acceleration vector of the ship at the subject's location. Based on this, a controller was designed with gains that were derived from correlations made between the ship acceleration vector and the foot – ship reaction moments of each person. In order to maintain stability and also replicate coordinated muscle movement, both open-loop and closed-loop control strategies were employed.

When the controller was applied to the model, it was found that the interaction forces and moments between the ship and human subjects correlated well with both the experimental moments and the moments derived from an inverse dynamics analysis. Further, it was found that the non-symmetric model matched the experimental data most closely in the direction of largest ship angular motion, regardless of which direction the subject/model was facing.

6.2 Discussion

The results show that in shipboard environments humans do behave similarly to an inverted pendulum with linear feedback control as previous research has identified, but with caveats. One issue is that there were some cases where the model did not match the experimental data. A common observation in those cases, and to a lesser extent in the cases where the model did match the experimental data, is that the controller that was developed required much larger torques than what was measured. One source for this is that the central nervous system (CNS) likely coordinates moment outputs between joints in a more efficient manner than the derived controller, which is a common topic when employing human-like open-loop control mechanisms. The inverted pendulum model generated its largest moments at the ankle joint, whereas a human would be able to generate the greatest control moments at the hips due to muscle placement. Designing a controller that generates its largest moments at the hips is a nontrivial task due to the force balance on the lower limbs, which would require a more complex control method than simple linear feedback. It is likely that the range of motion of specific joints and muscles is also a factor. It is also likely that the CNS performs a fair amount of motion planning in advance of actual motions, coordinating individual muscles in specific patterns in order to generate larger overall movements. The harmonic nature of the ship environment could also be a factor. Due to the repetitive nature of the ship motion, it is likely that there is a fair amount of motion prediction, either passively or actively, occurring. For example, based on the rate of change of the motion of the ship, a prediction can be made on the amount of force that will be required to maintain stability when the ship eventually changes direction.

One of the original motivations of this research project was the investigation of motion-induced interruptions (MIIs) as well as motion-induced corrections (MICs). In theory MICs occur when a person adjusts their stance before it is absolutely necessary to, whereas MIIs occur when a person has no other choice but to take a step. These phenomena were not able to be studied in as much detail as was anticipated, due to several factors. One is that the ship motions were simply not significant enough to induce consistent MIIs, especially among the experienced sea-faring participants. Because of this, it was not possible to instruct participants to either step constantly or step when they felt they needed to, because they were simply not needing to step at all, especially at the 0° and 45° orientations. Additionally, the burden upon the subject was already significant with the continuous instrument calibration requirements, the upkeep of specific foot placements, the performance of the cognitive task, and maintaining balance in an unpredictable motion environment without a hand hold.

This brings up another interesting point on the measured control strategies. Due to the cognitive task the participants were required to perform, it is likely that the participants were not actively determining their responses to the ship motion. It is likely that most of their responses to the ship motion, aside from stepping events, were passively determined by the CNS, which is a standard procedure since people commonly stand, walk, run, and perform other motions without actively determining how their bodies will move from moment to moment.

The Quest sea trial was one of few human postural stability experiments which has been carried out on a ship in the ocean rather than on a motion platform in the laboratory. The advantages of having actual ship motion are that the possible range of translational motions are much greater on the ship and the subjects have time to become acclimated to the ship motions in advance of the individual trials which provided a more accurate representation of shipboard working conditions. The disadvantages include the lack of repeatability of the motions and the difficulty of calibrating a variety of sensors in a constantly-moving environment. The data acquisition technologies provided more detailed information than has ever before been recorded in a shipboard environment, especially with the full-body motion capture systems. While a significant portion of the data was used in the analysis presented in this thesis, many more years of useful experimental results may be extracted from the data. Additionally, as the cost of high-quality biometric sensors continues to decrease and the variety of available sensors increases, it is likely that future sea trial experiments could expand on these data acquisition techniques.

Concerning the control system development, while the derived system performs remarkably well and provides useful information when simulated, there is much additional complexity that could be added to the model. Some of the research project's original goals included incorporation of state estimation, time delays, and sensory input weighting as discussed in the first chapter. These control techniques that have been incorporated into 2D postural stability models, however, become markedly nontrivial when applied to spatial dynamics models with multiple degrees of freedom.

Most nonlinear control design strategies involve linearizing the system dynamics so that linear controller design strategies can be employed. The method used in Chapter 4 to derive the equations of motion was convenient for derivation and coding, as it did not require a final algebraic form of the equations to be produced prior to simulating them. This was beneficial since each term of the equations consisted of products of many trigonometric functions due to the many degrees of freedom. Unfortunately, without a final algebraic form, it was very difficult to linearize the equations algebraically. This limitation also impeded the application of state estimation theory to the controller design. During the development of the inverted pendulum model, it was expected that nonlinear control methods would be required to design a controller which behaved similarly to a human, which was reinforced when simple feedback control was not sufficient. It was fortuitous that including an open-loop component allowed the controller to attain its performance objectives without requiring a nonlinear component.

Experimental error has not been comprehensively addressed over the course of this project. There is no doubt that there are measurement errors associated with all of the experimental data that became magnified when data sources were combined and when noisy data were filtered. Of special note is the data from the insoles and from the Kinect motion capture. It is very likely that these data sources contributed a substantial amount of error to the base of support analysis in Chapter 3 since the insole data for the left foot was noticeably different from that of the load cell (a more accurate sensor) and it is known that the unprocessed Kinect sensor measurements have an uncertainty of 1-2 cm at the distance that they were used. It is possible that this error could have had an effect on the results at the end of Chapter 3 which attempted to identify markers indicating the onset of motion induced interruptions. That said, the motion capture centre of mass recordings do independently correlate with the measurements made of total acceleration by the IMU, and it is more likely that if the experimental error had had a significant effect on the results, it would have prevented them from showing the clear correlation that was observed.

The possibility of compounding of experimental errors is why the controlled model's performance is only evaluated in a general way rather than in specific situations. The derived controller does not indicate the onset of any of the motion induced interruptions so there is potential for improvement here – both in the recognition of experimental markers and on the identification of the exact causes of motion induced interruptions.

6.3 Conclusion

Despite the limitations and opportunities for future work discussed above, this project makes several significant contributions to shipboard postural stability research. These are summarized below.

A human postural stability model has been developed as a spatial four-link inverted pendulum with a control system that makes it behave similarly to an actual human when exposed to six-degree-of-freedom ship motion. This model is an improvement over existing actively-controlled shipboard postural stability models because of its spatial orientation and several degrees of freedom.

A common metric in the study of postural stability is to study the motion of the centre of mass within the base of support. This thesis has provided an advanced analysis of the behaviour of these metrics under the conditions of full six-DOF ship motion which has not been studied as comprehensively as lab motion experiments. While no clear conclusions were able to be made using this analysis in this thesis, the groundwork has been laid for future researchers to continue analysis of these data.

In addition to the data used in the centre of mass analysis, a significant amount of human biometric data has been gathered in a heavy weather sea trial through experiments that were designed and executed as a component of this research project. This was the first time that a full-body motion capture system had been employed in a shipboard environment in order to study the response of humans to ship motion. The sea trial data set also included foot pressure data from two sensors, head inertial data, and head vision data.

Control of a multi-link spatial inverted pendulum under six-DOF ship motion that also mimics the behaviour of a human is a nontrivial task which this thesis has successfully accomplished. It is shown that a control strategy that employs both closed-loop feedback components and open-loop motion planning components is required to maintain balance with a similar amount of centre of mass motion as that of a human. A novel approach that derives the control gains by correlating the experimental ship – human interface torques to the accelerations of the ship was implemented. This resulted in personalized control parameters for each subject which reflected the muscular torques their bodies were able to generate. The resulting controllers were shown to be stable and perform similarly for

49 experimental trials divided between 8 participants. Overall, the results then showed a clear trend between the accuracy of the controller and the direction of greatest ship angular motions, which was a remarkable accomplishment considering the complexity of human balance control. In its current state the model could be a used as a tool to predict how much space would be required on board a ship for a person to perform a simple record keeping task without coming into contact with the walls of the ship. This thesis has presented a clear advancement in the research area of human postural response in ocean environments while also laying the groundwork for continued research in this area.

References

[1] R. Graham, A.E. Baitis, and W.G. Meyers. On the development of seakeeping criteria. *Naval Engineers Journal*, 104:259–275, 1992.

[2] A.H. Wertheim. Working in a moving environment. *Ergonomics*, 41:1845–1858, 1998.

[3] A. Bagchee, A. Bhattacharya, P.A. Succop, and R. Emerich. Postural stability assessment during task performance. *Occupational Ergonomics*, 1(1):41–53, 1998.

[4] CBC News Laura Payton. Halifax, B.C. yards win shipbuilding work. http://www.cbc.ca/ news/ politics/ story/ 2011/10/19/ pol-shipbuilding-announcement.html, October 2011.

[5] R.G. Langlois and R.J. Anderson. Multibody dynamics of very flexible damped systems. *Multibody System Dynamics*, 3(2):109–136, May 1999.

[6] W. Schiehlen. Multibody system dynamics: roots and perspectives. *Multibody System Dynamics*, 1(2):149–188, 1997.

[7] A.W. Sovol, K.D. Bustamante Valles, S.A. Riedel, and G.F. Harris. Bi-planar postural stability model: Fitting model parameters to patient data automatically. In *32nd Annual International Conference of the IEEE IMBS*, 2010.

[8] J. Mckee. Simulating the effects of ship motion on postural stability using articulated dynamic models. Master's thesis, Carleton University, 2004.

[9] R. G. Langlois. Development of a spatial inverted pendulum shipboard postural stability model. In *International Conference on Human Performance at Sea*, Glasgow, Scotland, UK, June 2010.

[10] Xinjilefu, V. Hayward, and H. Michalska. Stabilization of the spatial double inverted pendulum using stochastic programming seen as a model of standing postural control. In *9th IEEE-RAS International Conference on Humanoid Robots*, 2009.

[11] C.W. Stockwell, S.H. Koozekanai, and K. Barin. A physical model of human postural dynamics. *Annals of the New York Academy of Sciences*, 374:722–730, 1981.

[12] H. C. Diener, J. Dichgans, W. Bruzek, and H. Selinka. Stabilization of human posture during induced oscillations of the body. *Experimental Brain Research*, 45:126–132, 1982.

[13] K. Barin. Evaluation of a generalized model of human postural dynamics and control in the sagittal plane. *Journal of Biological Cybernetics*, 61:37–50, 1989.

[14] A.D. Kuo and F.E. Zajac. Human standing posture: multijoint movement strategies based on biomechanical constraints. *Progress in Brain Research*, 97:349–358, 1993.

[15] J.E. Bos. Feasibility of motion induced interruption (MII) prediction. Technical Report TM-99-A017, TNO Human Factors Research Institute, 1999.

[16] B.E. Maki, W.E. McIlroy, and S.D. Perry. Influence of lateral destabilization on compensatory stepping responses. *Journal of Biomechanics*, 29(3):343–353, 1996.

[17] H. Hemami and B.T. Stokes. A qualitative discussion of mechanisms of feedback and feedforward in the control of locomotion. *IEEE Transactions on Biomedical Engineering*, BME-30:681–688, 1983.

[18] S. Corna, J. Tarantola, A. Nardone, A. Giordano, and M. Schieppati. Standing on a continuously moving platform: is body inertial counteracted or exploited? *Experimental Brain Research*, 124(3):331–341, 1999.

[19] J.L. Borah, L.R. Young, and R.E. Curry. Optimal estimator model for human spatial orientation. *Annals of the New York Academy of Sciences*, 545(1):51–73, 1988.

[20] A.D. Kuo. An optimal control model for analyzing human postural balance. *IEEE Transactions on Biomedical Engineering*, 42(1):87–101, January 1995.

[21] H. van der Kooij, R. Jacobs, B. Koopman, and H. Groontenboer. A multisensory integration model of human stance control. *Biological Cybernetics*, 80:299–308, 1998.

[22] H. van der Kooij, R. Jacobs, B. Kiipan, and F. van der Helm. An adaptive model of sensory integration in a dynamic environment applied to human stance control. In *American Control Conference*, pages 2297–2298, June 2001.

[23] J.E. Bos, W. Bles, R.J.A.W. Hosman, and E.L. Groen. The cause of spatial disorientation. Technical Report ADP013845, 2003.

[24] J.E. Bos and W. Bles. Theoretical considerations on canal – otolith interaction and an observer model. *Biological Cybernetics*, 2002.

[25] S. Chiou. Effects of environmental and task risk factors on workers' perceived sense of postural sway and instability. *Occupational Ergonomics*, 1:81–93, 1998.

[26] L.M. Nashner. *Sensory Feedback in Human Posture Control.* PhD thesis, Massachusetts Institute of Technology, 1970.

[27] D.A. Winter. Human balance and postural control during standing and walking. *Gait and Posture*, 3(4):193–214, 1995.

[28] P.J. Lee, E.L. Rogers, and K.P. Granata. Active trunk stiffness increases with co-contraction. *Journal of Electromyography and Kinesiology*, 16:51–57, 2006.

[29] F.B. Horak and L.M. Nashner. Central programming of postural movements: adaptation to altered support-surface configurations. *Journal of Neurophysiology*, 55:1369–1381, 1986.

[30] C. Tian and J. He. Simulation study of human posture control under external perturbation. In *IEEE Conference on Decision and Control*, San Diego, CA, USA, 1997.

[31] A. Roy and K. Iqbal. PID controller stabilization of a single-link biomechanical model with multiple delayed feedbacks. In *IEEE International Conference on Systems, Man and Cybernetics*, 2003.

[32] K.A. Tahboub. Biologically-inspired humanoid postural control. *Journal of Physiology - Paris*, 103:195–210, 2009.

[33] L.M. Nashner. Adaptation of human movement to altered environments. *Trends in Neurosciences*, 5:358–361, 1982.

[34] H. Hemami. The inverted pendulum and biped stability. *Mathematical Biosciences*, 34(2):95–110, 1977.

[35] H. Hemami and V.C. Jaswa. On a three-link model of the dynamics of standing up and sitting down. *IEEE Transactions on Systems, Man and Cybernetics*, SMC-8:120–135, 1978.

[36] Q. Wang and J. He. Control model of postural stability using LQR and fuzzy logic controller. In *Proceedings of The First Joint BMES/EMBS Conference Serving HUmanity, Advancing Technology*, 1999.

[37] Q. Wu. Lyapunov's stability control of constrained inverted pendulum. In *Proceedings of the American Control Conference*, 1999.

[38] P.D. Frazier and M.F. Chouikha. A novel control model for elucidating human postural balance. In *Proceedings of the 5th World Congress on Intelligent Control and Automation*, 2004.

[39] S. Virk and K.M. Valter McConville. Virtual reality applications in improving postural control and minimizing falls. In *Proceedings of the 28th IEEE EMBS Annual International Conference*, 2006.

[40] L.M. Nasher. Organization and programming of motor activity during posture control. *Reflex Control of Posture and Movement, Progress in Brain Research*, 1979.

[41] K. Sarioz and E. Narli. Effect of criteria on seakeeping performance assessment. *Ocean Engineering*, 32:1161–1173, 2005.

[42] P. Crossland, M.J. Evans, D. Grist, M. Lowten, H. Jones, and R.S. Bridger. Motion induced interruptions aboard ship: Model development and application to ship design. *Occupational Ergonomics*, 7:183–199, 2007.

[43] A.E. Baitis, T.R. Applebee, and T.M. McNamara. Human factors considerations applied to operations of the FFG-8 and lamps MK III. *Naval Engineers Journal*, 97(4):191–199, 1984.

[44] R.G. Langlois, S.N. Mackinnon, and C.A. Duncan. Modelling sea trial motion induced interruption data using an inverted pendulum articulated postural stability model. *International Journal of Maritime Engineering*, 151, 2009.

[45] J.L. Colwell, N. Allen, J. Bos, and et al. Human performance trial QUEST Q-303. In *International Martime Conference*, 2008.

[46] C.A. Duncan, S.N. MacKinnon, and W.J. Albert. Changes in thoracolumbar kinematics and centre of pressure when performing stationary tasks in moving environments. *International Journal of Industrial Ergonomics*, July 2010.

[47] A. Hunter, N. Bourgeois, and R. Langlois. The impact of motion induced interruptions on cognitive performance. In *6th International Conference on Applied Human Factors and Ergonomics*, 2014.

[48] N.R. Bourgeois, R.G. Langlois, and A. Hunter. Quest Q-348 sea trial: Human postural stability studies. In *International Conference of Control, Dynamic Systems, and Robotics*, Ottawa, Canada, 2014.

[49] E. M. Lewandowski. *The Dynamics of Marine Craft: Maneuvering and Seakeeping*. World Scientific Publishing Co. Pte. Ltd., 2004.

[50] Y-C. Pai and J. Patton. Center of mass velocity-position predictions for balance control. *Journal of Biomechanics*, 1997.

[51] D.A. Winter. *Biomechanics and Motor Control of Human Movement, 4th Edition*. John Wiley and Sons Inc., Hoboken, New Jersey, 2009.

[52] J. H. Mathews and K. K. Fink. *Numerical Methods Using MATLAB, 4th Edition*. Prentice-Hall Inc., 2004.

[53] P.E. Nikravesh. *Computer-aided analysis of mechanical systems*. Prentice Hall, 1988.

[54] J. Martin. Postural stability of humans. Master's thesis, Carleton University, 2010.

[55] F.M.L. Amirouche. *Fundamentals of Multibody Dynamics*. Birkhauser Boston, 2006.

[56] N. Bourgeois and R. Langlois. Derivation and validation of a spatial multi-link human postural stability model. In *CCToMM Symposium on Mechanisms, Machines, and Mechatronics*, 2015.

[57] R.L. Huston. *Multibody Dynamics*. Butterworth-Heinemann, 1990.

[58] H.E. Morris and R.G. Langlois. Generic stance geometry model for determining postural stability motion induced interruption onsets. In *International Conference of Control, Dynamic Systems, and Robotics*, Ottawa, Canada, 2014.

[59] R.G. Langlois and R.J. Anderson. A tutorial presentation of alternative solutions to the flexible beam on rigid cart problem. In *Transactions of the Canadian Society for Mechanical Engineering*, volume 29, pages 357–373, 2005.

[60] Roger Carpenter and Benjamin Reddi. *NeurophyEdition: A Conceptual Approach*. Hodder Arnold, 2012.

[61] H. Hemami, L. Humphrey, K. Barin, and A. Krishnamurthy. Simulated responses to support surface disturbances in humanoid biped model with a vestibular-like apparatus. *IEEE Transactions on Systems, Man and Cybernetics*, 40(1):109–119, 2010.

Appendix A

Ethics Clearance

In advance of the sea trial experiments it was necessary to acquire peer-reviewed ethical clearance of the intended experiments since they involved human participants. Included in this appendix are the ethics approval documents from the Carleton University Research Ethics Board (13-0632) and the DRDC Human Research Ethics Committee (2012-045).

Appendix B

Simulation Code

This appendix contains the function written in MATLAB that calculates $\ddot{\mathbf{x}}$ for the four-link inverted pendulum model. This function is presented here because it allows one to see how the multibody dynamics method presented in this thesis allows the dynamics code to be written in terms of the geometrical properties of the model and the transformation matrices between frames, which allows for a simple debugging process when troubleshooting the simulation. Some of the variable names have been changed from the original code to more accurately reflect the variable naming conventions used in this thesis.

```
function [ x_dotdot ] = computeAccel(obj,x,x_dot,xx,xx_dot,xx_dotdot,Minp,Finp,dir)
% Outputs: x_dotdot - 27x1 divided into:
%                     12x1 Bryant rates
%                      3x1 Reaction forces
%                     12x1 Generalized coordinate 2nd derivatives
% Inputs: obj         - four-bar linkage class object
%           x         - 12x1 inverted pendulum Bryant angles
%           x_dot     - 12x1 inverted pendulum generalized coordinate
%                       derivatives
%           xx        - 3x1 ship Bryant angles
%           xx_dot    - 6x1 ship velocities
%           xx_dotdot - 6x1 ship accelerations
%           Minp      - 12x1 control moments
%           Finp      - 12x1 external forces (aside from gravity) if
```

```
%                            present
%           dir       - direction of subject wrt ship centreline



I = obj.I; % 3x3 identity matrix
O = obj.O; % 3x3 zero matrix

% transformation from angular velocities to Bryant rates
BB = [ RotMatVelocityToBryantRates(x(1:3)) zeros(3)  zeros(3) zeros(3);
    zeros(3) RotMatVelocityToBryantRates(x(4:6)) zeros(3) zeros(3);
    zeros(3) zeros(3) RotMatVelocityToBryantRates(x(7:9)) zeros(3);
    zeros(3) zeros(3) zeros(3) RotMatVelocityToBryantRates(x(10:12))];



% Transformation matrices
% Transforms from first index to second index
% So R10 is from 1 to 0
R10 = RMat(xx(1:3));
R21 = [ cosd(dir) -sind(dir) 0 ; sind(dir) cosd(dir) 0 ; 0 0 1]';
R32 = RMat(x(1:3));
R43 = RMat(x(4:6));
R54 = RMat(x(7:9));
R65 = RMat(x(10:12));

R30 = R32 * R21 * R10;
R40 = R43 * R30;
R50 = R54 * R40;
R60 = R65 * R50;

R31 = R32*R21;
R42 = R43*R32;
R41 = R42*R21;
R53 = R54*R43;
R52 = R53*R32;
R51 = R52*R21;
R64 = R65*R54;
R63 = R64*R43;
R62 = R63*R32;
R61 = R62*R21;
```

```
% Wk transforms generalized coordinate derivatives to absolute
% angular velocities in each local frame
Q  = [ I   O     R31' R41' R51' R61' ;
       O   R10   O    O    O    O    ;
       O   O     I    R43' R52' R63' ;
       O   O     O    I    R53' R64' ;
       O   O     O    O    I    R65' ;
       O   O     O    O    O    I    ];

ang_vel = ([xx_dot' x_dot'] * Q)';

% Derivatives of transformation matrices
R10_dot = SkewMat(ang_vel(1:3))'*R10;
R30_dot = SkewMat(ang_vel(7:9))'*R30;
R40_dot = SkewMat(ang_vel(10:12))'*R40;
R50_dot = SkewMat(ang_vel(13:15))'*R50;
R60_dot = SkewMat(ang_vel(16:18))'*R60;

% Partial angular velocities
W1  = [ R10 ; O ; O   ; O   ; O   ; O   ];
W1s = [ O   ; O ; O   ; O   ; O   ; O   ];
W3  = [ R10 ; O ; R30 ; O   ; O   ; O   ];
W4  = [ R10 ; O ; R30 ; R40 ; O   ; O   ];
W5  = [ R10 ; O ; R30 ; R40 ; R50 ; O   ];
W6  = [ R10 ; O ; R30 ; R40 ; R50 ; R60 ];

% partial angular velocities substituted for constrained joints
W3I = [ O   ; O ; R30 ; O   ; O   ; O   ];
W4I = [ O   ; O ; O   ; R40 ; O   ; O   ];
W5I = [ O   ; O ; O   ; O   ; R50 ; O   ];
W6I = [ O   ; O ; O   ; O   ; O   ; R60 ];


% Derivatives of partial angular velocities
W1_dot  = [ R10_dot ; O ; O       ; O       ; O       ; O      ];
W1s_dot = [ O       ; O ; O       ; O       ; O       ; O      ];
W3_dot  = [ R10_dot ; O ; R30_dot ; O       ; O       ; O      ];
W4_dot  = [ R10_dot ; O ; R30_dot ; R40_dot ; O       ; O      ];
```

```
W5_dot  = [ R10_dot ; O ; R30_dot ; R40_dot ; R50_dot ; O      ];
W6_dot  = [ R10_dot ; O ; R30_dot ; R40_dot ; R50_dot ; R60_dot];

% Partial velocities
V1  = [ obj.S_r1 * R10 ; O ; O ; O ; O ; O ];
V1s = [ O ; R10 ; O ; O ; O ; O ];
V3  = [ obj.S_q1 * R10 ; R10 ; obj.S_r3 * R30 ; O ; O ; O ];
V4  = [ obj.S_q1 * R10 ; R10 ; obj.S_q3 * R30 ; obj.S_r4 * R40 ; O ; O ];
V5  = [ obj.S_q1 * R10 ; R10 ; obj.S_q3 * R30 ; obj.S_q4 * R40 ; obj.S_r5 * R50 ; O ];
V6  = [ obj.S_q1 * R10 ; R10 ; obj.S_q3 * R30 ; obj.S_q4 * R40 ; obj.S_q5 * R50 ; ...
        R60' * obj.S_r6 * R60 ];

% Derivates of partial velocity matrices
V1_dot  = [ obj.S_q1 * R10_dot ; O ; O ; O ; O ; O ];
V1s_dot = [ obj.S_q1 * R10_dot ; R10_dot ; O ; O ; O ; O ];
V3_dot  = [ obj.S_q1 * R10_dot ; R10_dot ; obj.S_r3 * R30_dot ; O ; O ; O ];
V4_dot  = [ obj.S_q1 * R10_dot ; R10_dot ; obj.S_q3 * R30_dot ; obj.S_r4 * R40_dot ; O ; O ];
V5_dot  = [ obj.S_q1 * R10_dot ; R10_dot ; obj.S_q3 * R30_dot ; obj.S_q4 * R40_dot ;  ...
        obj.S_r5 * R50_dot ; O ];
V6_dot  = [ obj.S_q1 * R10_dot ; R10_dot ; obj.S_q3 * R30_dot ; obj.S_q4 * R40_dot ;  ...
        obj.S_q5 * R50_dot ; obj.S_r6 * R60_dot ];

% Qk transforms generalized coordinate derivatives to absolute
% angular velocities in inertial frame
Qk = [ R10 O   R10 R10 R10 R10 ;
       O   R10 O   O   O   O ;
       O   O   R30 R30 R30 R30 ;
       O   O   O   R40 R40 R40 ;
       O   O   O   O   R50 R50 ;
       O   O   O   O   O   R60 ];

ang_vel = ([xx_dot' x_dot'] * Qk)';

% Transform inertia to inertial frame
I_10 = (R10' * obj.I_1 * R10)';
I_30 = (R30' * obj.I_3 * R30)';
I_40 = (R40' * obj.I_4 * R40)';
I_50 = (R50' * obj.I_5 * R50)';
I_60 = (R60' * obj.I_6 * R60)';
```

```
% Skew matrices of angular velocities
Z1 = SkewMat(ang_vel(1:3)'*I_10')';
Z3 = SkewMat(ang_vel(7:9)'*I_30')';
Z4 = SkewMat(ang_vel(10:12)'*I_40')';
Z5 = SkewMat(ang_vel(13:15)'*I_50')';
Z6 = SkewMat(ang_vel(16:18)'*I_60')';

% Transform V^k to V^k_Q
V1_Q  = Q * V1;
V1s_Q = Q * V1s;
V3_Q  = Q * V3;
V4_Q  = Q * V4;
V5_Q  = Q * V5;
V6_Q  = Q * V6;
V1_Q_dot  = Q * V1_dot;
V3_Q_dot  = Q * V3_dot;
V4_Q_dot  = Q * V4_dot;
V5_Q_dot  = Q * V5_dot;
V6_Q_dot  = Q * V6_dot;

% Generalized mass matrix
A1 = obj.m(1) * (V1_Q * V1_Q') + ...
     obj.m(3) * (V3_Q * V3_Q') + ...
     obj.m(4) * (V4_Q * V4_Q') + ...
     obj.m(5) * (V5_Q * V5_Q') + ...
     obj.m(6) * (V6_Q * V6_Q');

A2 = W1 * I_10 * W1' + ...
     W3 * I_30 * W3' + ...
     W4 * I_40 * W4' + ...
     W5 * I_50 * W5' + ...
     W6 * I_60 * W6';

A = A1 + A2;


% Constrained DOF
A(:,9)  = -W3I(:,3);
```

```
A(:,10) = -W4I(:,1);
A(:,12) = -W4I(:,3);
A(:,15) = -W5I(:,3);
A(:,18) = -W6I(:,3);

A_RHS(1:18,1:6) = A(1:18,1:6);
A(4:18,4:6) = -V1s_Q(4:18,1:3);

% Linear and nonlinear damping matrices
B1 = obj.m(1) * (V1_Q * V1_Q_dot') + ...
     obj.m(3) * (V3_Q * V3_Q_dot') + ...
     obj.m(4) * (V4_Q * V4_Q_dot') + ...
     obj.m(5) * (V5_Q * V5_Q_dot') + ...
     obj.m(6) * (V6_Q * V6_Q_dot');

B2 = W1 * I_10 * W1_dot' + ...
     W3 * I_30 * W3_dot' + ...
     W4 * I_40 * W4_dot' + ...
     W5 * I_50 * W5_dot' + ...
     W6 * I_60 * W6_dot';

B = B1 + B2;

C = W1 * Z1 * W1' + ...
    W3 * Z3 * W3' + ...
    W4 * Z4 * W4' + ...
    W5 * Z5 * W5' + ...
    W6 * Z6 * W6';

% Gravity forces
% Finp is normally zeros
f3 = [0 0 -obj.m(3)*obj.g] + Finp(1:3)';
f4 = [0 0 -obj.m(4)*obj.g] + Finp(4:6)';
f5 = [0 0 -obj.m(5)*obj.g] + Finp(7:9)';
f6 = [0 0 -obj.m(6)*obj.g] + Finp(10:12)';
F = V3_Q*f3' + V4_Q*f4' + V5_Q*f5' + V6_Q*f6';

% Control moments
M3 = Minp(1:3);
```

```
M4 = Minp(4:6);
M5 = Minp(7:9);
M6 = Minp(10:12);
M =  W3*M3 + W4*M5 + W5*M5 + W6*M6;

f = F + M;

RHS = f(4:18) ...
    - B(4:18,1:18) * [xx_dot ; x_dot ] ...
    - C(4:18,1:18) * [xx_dot ; x_dot ] ...
    - A_RHS(4:18,1:6)*xx_dotdot;

% only solve equations for DOF we are interested in
RHS = [RHS(4:5,1) ; RHS(8,1) ; RHS(10:11,1) ; RHS(13:14,1) ];
A = [A(:,1:8) A(:,11) A(:,13:14) A(:,16:17) ];
A = [A(1:8,:) ; A(11,:) ; A(13:14,:) ; A(16:17,:) ];

% global variables used to store values for stability analysis
global Aglobal;
global Fglobal;
global Wglobal;

Aglobal = A(7:13,7:13);
Fglobal = RHS;
Wglobal = W;

x_dotdot = zeros(27,1);
x_dotdot(1:12,1) = BB * x_dot;

temp = A(7:13,7:13) \ RHS ;
x_dotdot(16:17) = temp(1:2);
x_dotdot(20) = temp(3);
x_dotdot(22:23) = temp(4:5);
x_dotdot(25:26) = temp(6:7);

end
```

Appendix C

Simulation Results

This section contains experimental and simulation sea trial results from 49 separate trials divided between 8 experiment participants. Each page of data corresponds to one 6-minute trial. The contents of each page are described below.

The number at the top of the page indicates which participant the data corresponds to and the starting date and time of the experimental trial.

The graph in the top left corner of the page shows a time-lapse of the motion of the person's left and right feet, centre of mass, and centre of force. Only the average value of their base of support online is displayed in order to reduce clutter. For all graphs, the front (bow) of the ship is on the right. The graphs are divided between the person standing at 0°, 45°, and 90° with respect to ship centreline, in which the person would be facing to the right, to the top right, and toward the top of the page, respectively.

The four graphs that span the width of the page compare results from the four-link inverted pendulum model (4BAR) to the experimental results (EXP), and to the inverse dynamics results (ID). The top two graphs compare the reaction moments at the ship. For the 4BAR and ID results, this is the reaction moment between the inverted pendulum model and the ship. For the experimental results, this is the reaction force from the insoles multiplied by the distance between the centre of force and centre of mass. The bottom two graphs compare the results of the motions. For the 4BAR model results, this is the angle between the inertial vertical and a line from the ankle joint to the model's centre of mass. For the 'accel' results, this is the angle between the inertial vertical and the total acceleration vector. For the BVH results, this is the angle between the inertial vertical and a line from a point between the person's ankles to their centre of mass, as determined from the motion capture data. The numbers in the tables next to each of these graphs are the Pearson correlation coefficient values between the indicated data sets.

The graph in the top right compares the ship direction of best simulation – experimental results with the direction of greatest ship motion and direction of greatest centre of mass sway of the participant. The 4BAR line corresponds to how well the simulation centre of mass motion results correlate to the direction of total acceleration. Roll motion is represented on the x axis and pitch motion on the y axis. The angle of this line indicates the direction in the ship frame in which the results match most closely. The 'Ship' line indicates the direction of maximum ship angular motion using RMS roll and pitch angles. The BVH line indicates the direction of maximum subject sway. The table on the right side of the graph displays the angle in degrees between the indicated lines.